Measurements of directed, elliptic, and triangular flow of charged hadrons from Cu+Au collisions at $\sqrt{s_{NN}} = 200$ GeV with PHENIX at RHIC

By

Brennan C. Schaefer

Dissertation

Submitted to the Faculty of the

Graduate School of Vanderbilt University

in partial fulfillment of the requirements

for the degree of

DOCTOR OF PHILOSOPHY

in

Physics

August, 2016

Nashville, Tennessee

Approved:

Julia A. Velkovska, Ph.D.

Charles F. Maguire, Ph.D.

Andreas A. Berlind, Ph.D.

Sait A. Umar, Ph.D.

ACKNOWLEDGMENTS

I have looked to my advisor for many things. From specific analysis techniques up to the bigger picture of providing direction for my physics pursuit, I have come to rely on her with a sense of assuredness. Having worked in the large PHENIX Collaboration for the duration of my term, I've also been very fortunate to have such a strong personal advocate. Julia, I want you to know I am very thankful for all you have done, and for your patience throughout.

I wish to thank the Ph.D. committee members for overseeing my progress. There have also been a number of scientists in PHENIX who have helped in this work, they include: Hiroshi Nakagomi, Shin-Ichi Esumi, Javier Orjuela Koop, Martin Purschke, Chris Pinkenburg, Mickey Chiu, John Haggerty, Paul Stankus, Takao Sakaguchi, Jeffery Mitchell, Gabor David, and Victor Riabov.

TABLE OF CONTENTS

LIST OF TABLES

LIST OF FIGURES

$\bar{p}$	anti-proton
χ	chi, used in data quality tests
Δt	time difference
ε	energy density in a thermodynamic system
η/s	shear viscosity over entropy density
γ	Lorentz factor
Λ	lambda baryon
μ	baryon chemical potential
ϕ	azimuthal angle
π^0	neutral pion
$\pi^{\pm}$	charged pion
Ψ_n^A	n^{th} order event plane measured in A detector
p_T	transverse momentum
σ	standard deviation
$\sqrt{s_{NN}}$	center-of-mass energy per nucleon pair
ε_n	n^{th} order eccentricity of nuclear overlap region based on positions of interacting nucleons
$\vec{b}$	collision impact vector
Ξ	xi, or cascade baryon
$A+A$	nuclear collision species
A_m, B_m	generic Fourier coefficients
dS	change in entropy in a thermodynamic system
E	energy in a thermodynamic system
$g^{\mu\nu}$	metric tensor
$h^{\pm}$	positive and negative hadrons
$K^{\pm}$	charged kaon
KE_T	transverse kinetic energy, $m_T - m$
L	path length
m	mass
m_T	transverse mass
N	number of identical particles in a thermodynamic system
n	number of baryons in a thermodynamic system
N_{part}	number of participants
n_q	number of quarks scaling parameter
P	pressure in a thermodynamic system
p	momentum
p	proton
$Res(\Psi_n^A)$	resolution of n^{th} order event plane measured with detector A
s	entropy per baryon in a thermodynamic system
T	temperature in a thermodynamic system
$T^{\mu\nu}$	energy-momentum tensor
u^{μ}, u^{ν}	velocity 4-vectors components
V	volume in a thermodynamic system

v	velocity
v_n	n^{th} order Fourier coefficient characterizing flow
z	cylindrical height coordinate, distance from collision vertex
3D+1	hydrodynamical model with 3 spatial and 1 time dimensions
Q-vector	weighted flow vector
ADC	analog to digital converter
AMPT	A Multi-Phase Transport Model simulation of heavy ion collisions
AMU	analog memory unit
ART	A Relativistic Transport model used in simulation
ATP	assembly trigger processor
Au	gold
BBC	Beam-Beam Counter detector
BD	black disk - in the context of the Glauber model, nucleons are considered to be solid spheres
BNL	Brookhaven National Laboratory
CERN	Conseil Européen pour la Recherche Nucléaire
CNT	central arm
Cu	copper
DAQ	data acquisition
DC	Drift Chamber
DCM	data collection module
DST	data summary tape file format
EMCal	ElectroMagnetic Calorimeter detector
EP	event plane
FEE	front end electronics
FEM	front end module
GD	grey disk - in the context of the Glauber model, nucleons are considered to have Gaussian density distribution
GEANT	GEometry ANd Tracking simulation
GeV	billion electron volts
HIJING	Heavy Ion Jet INteraction Generator
HPSS	High Performance Storage System
IRC	internal review committee
LHC	Large Hadron Collider
LVM	light vector mesons
mb	millibarn unit, 10^{-27} cm^2
MeV	million electron volts
MRPC	Multigap Resistive Plate Chamber
MWPC	Multi-Wire Proportional Chamber detector
PB	petabyte
Pb	lead
PbGl	Lead Glass detector
PbSc	Lead Scintillator detector
PC	Pad Chamber (PC1, PC2, PC3 layers) detector
PHENIX	Pioneering High Energy Nuclear Interaction eXperiment detector at RHIC

PID	particle identification
PLHF	photons LVM hadrons and flow working group
PMT	photo multiplier tube
PPG	paper preparation group
pQCD	perturbative quantum chromodynamics
PRDF	PHENIX raw data format
ps	picoseconds
QA	quality assurance
QCD	quantum chromodynamics
QGP	quark gluon plasma
RHIC	Relativistic Heavy Ion Collider
RP	reaction plane
SEB	sub-event buffer
SMD	Shower Maximum Detector detector
STAR	Solenoid Tracker at RHIC detector experiment
TB	terabyte
TeV	trillion electron volts
TOF	Time of Flight (TOFE, TOFW) East and West detectors
w.r.t.	with respect to
WA98	West Area 98 experiment at CERN
ZDC	Zero Degree Calorimeter detector

Chapter 1

Introduction

In 1975 Collins and Perry deduced that because the QCD coupling constant decrease with decreasing distance scales, a dense and hot state of matter could exist consisting of deconfined quarks and gluons [1]. Qualitative examination of this proposed state led Shuryak in 1980 to coin the name *quark gluon plasma* (QGP) [2] because this system would have free color charges, in analogy to the electromagnetic plasma. The Relativistic Heavy Ion Collider (RHIC) at Brookhaven National Laboratory was built with the purpose of creating a state of matter with the extreme temperature and energy density under which this phase of matter would exist, and further to allow the study of the phase transition from QGP into discrete hadrons [3].

RHIC collides ions such as gold and copper at center-of-mass energies up to 200 GeV per nucleon-nucleon pair. This allows the fundamental interactions of QCD to be examined in the context of bulk matter phenomena. In this regime the collective properties of strongly coupled matter can be studied using the tools of statistical mechanics and thermal physics.

An immediate question that comes to mind upon first learning that heavy ion collisions allow bulk properties of matter to be studied is, how could the minutest interval (~2 x 10^{-23} sec) afford any type of cumulative effects. A toy answer is that strong interactions tend to be quick ones, and further that everyday macroscopic chemical explosions are similarly studied using thermodynamics.

One of the primary observations confirming the existence of the quark gluon plasma at RHIC has come from measurements of anisotropic flow of produced particles. In particular, strong elliptic flow (indicated by an excess of particle emission in the plane containing the impact parameter vector and the beam axis) reaching the upper hydrodynamical limit sug-

gests that a near-perfect fluid is formed [4]. In the general case of ions colliding with partial overlap, the intersecting region has a lenticular shape with varying pressure gradients along the short and long axes. In order to propagate this gradient from the initial geometry into the observed azimuthal distribution of produced particles, hydrodynamic model calculations show the requirement of thermalization early on in the collision [4]. Independent evidence confirming thermalization comes from final-state abundances of hadrons, which are well described by thermal models that assume a system with a common baryon chemical potential and common temperature at chemical freeze-out. Evidence that thermalized partonic degrees of freedom are involved in building up the collective flow is seen in measurements of anisotropic flow of identified hadrons, including those featured in this work.

Anisotropic flow measurements together with theoretical modeling have made great strides in describing the QGP. The azimuthal distribution of produced particles is characterized using Fourier analysis with coefficients conventionally denoted by v_n. The strength of the second order harmonic (v_2) indicating elliptic flow has been further used to show the QGP has the properties of a nearly perfect fluid [3, 5, 6, 7]. The shear viscosity over entropy density (η/s) of this fluid is a tunable parameter in hydrodynamic calculations and it is found that the data favor values that are near the extreme lower bound for any fluid in nature [8, 9].

Experimental results from the LHC and RHIC have found non-zero values for v_1, v_3, and v_5 [10, 11, 12, 13, 14, 15], which are understood to be the product of fluctuations in the initial energy density distribution that varies on an event-by-event basis [16]. While v_2 is the strongest signal of anisotropic flow and has unlocked surprising discoveries on the properties of the QGP , measurements of the odd flow harmonics provide tighter bounds for theoretical modeling. The influence of the fluctuating initial geometry on each order of flow can be investigated empirically using different scaling parameters that describe the shape of the initial interaction region. Two such parameters are the eccentricity (ε_n) derived on an event-by-event basis from the positions of the nucleons that participate in inelastic

collisions, and the number of participants (N_{part}) which is related to the system size.

In 2012 RHIC collided Cu+Au at $\sqrt{s_{NN}} = 200$ GeV, the first system of its kind at high energy. This has afforded a unique opportunity to study the influence of geometry on particle production and collective expansion dynamics. Copper has approximately 1/3 the mass of gold yielding overlap regions that are asymmetric, except in the extreme central case. Measurements of v_1, v_2, and v_3 from this system are presented in this work for particles produced at midrapidity, including unidentified charged hadrons as well as identified $\pi^{\pm}$, $K^{\pm}$, p, and $\bar{p}$. Comparisons are made to measurements performed in the Cu+Cu and Au+Au systems. Various scaling parameters are used to investigate the sources within initial conditions that lead to final-state anisotropy. Comparisons to two theoretical calculations are also featured including 3D+1 viscous hydrodynamics and A-Multiphase-Transport Model (AMPT).

Chapter 2

The PHENIX Detector

The PHENIX detector is really many small detectors assembled together to provide a picture of high energy nuclear collisions. Individual detectors are commonly referred to as *subsystems* and studies of different phenomena in collisions of protons and nuclei use information from different subsystems. A brief description of each of the subsystems used in this work is provided below. PHENIX subsystems can be loosely categorized by their location. Forward detectors are close to the beam pipe (*z-axis*) and central arm detectors surround the interaction region centered on the *x-y* plane. The PHENIX experiment uses a right-handed coordinate system, with the z-axis pointing North along the beam direction, the x-axis pointing West, and the y-axis vertically up. Figure 2.1 illustrates the central arms (left) and forward (right) detectors within the greater PHENIX detector.

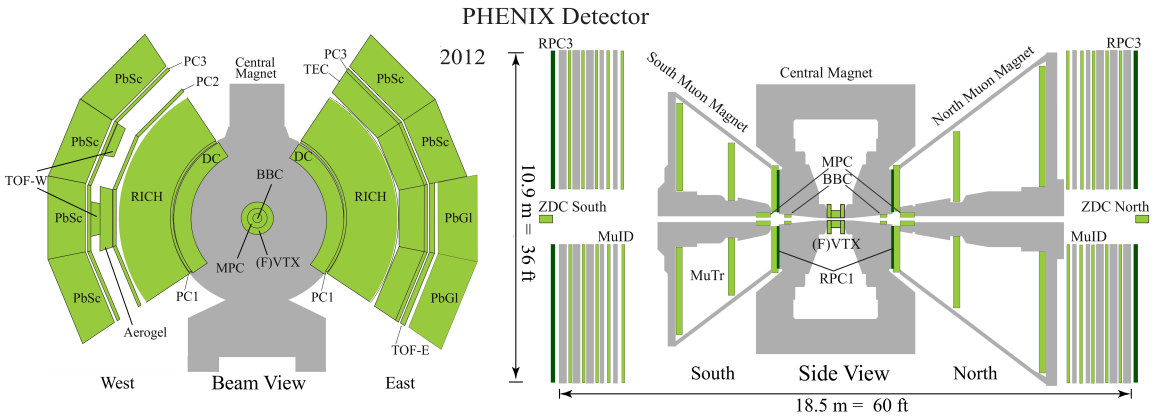

Figure 2.1: The PHENIX central arm (left) and forward (right) detector subsystems are shown in the configuration used in 2012 when Cu+Au data was taken.

2.1 Forward Detectors

2.1.1 Beam-Beam Counter

The Beam Beam Counter is a two part detector that surrounds the beam pipe at locations ±144 cm from the center (z = 0). Each side has 64 photo multiplier tubes (PMTs) arranged radially around the beam pipe that detect incident charged particles. The BBC readouts are used for several purposes. To signal whether a heavy ion bunch crossing has produced a collision that will be stored, a minimum of two PMTs on each side must fire. For proton+proton collisions the requirement is one PMT firing on each side. This event selection requirement is called the *minimum-bias trigger*. Using timing information from both sides, the collision position along the z-axis can be calculated along with the collision start time. Figure 2.2 shows the collision locations as measured by the BBC for the dataset used in this analysis. The width of the peak reflects how tightly ions are packed together in the bunches that travel in the beam pipe. The timing resolution of the BBC is estimated to be 40 ps, or 1.2 cm of path length for a particle moving with the speed of light [17].

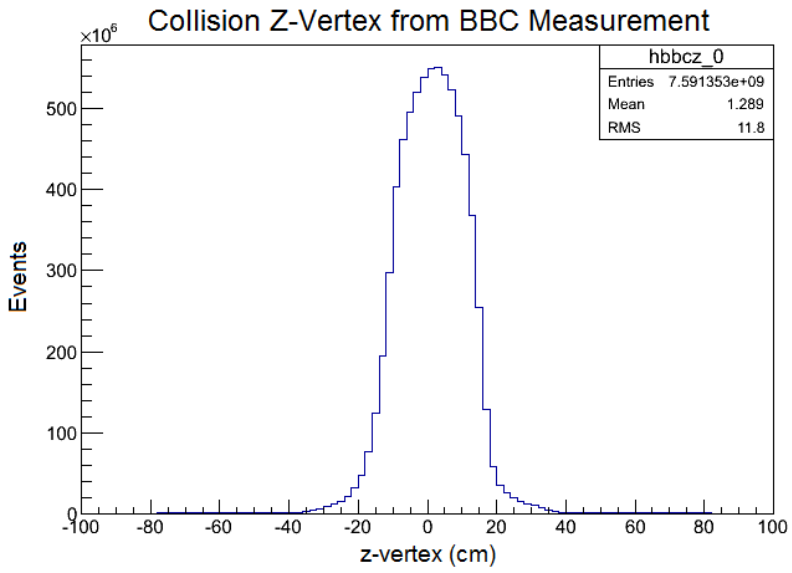

Figure 2.2: The Beam Beam Counter subsystem is used to find the collision location along the z-axis. The timing difference between incident charges and the distance between them is used to calculate the position and start time of collisions. The above distribution shows the z position of minimum bias collisions in Run 12 Cu+Au at $\sqrt{s_{NN}} = 200$ GeV in PHENIX.

The BBC can be used to measure the event plane angle of the collision. A more detailed explanation of this use is discussed in Section 4.1.1.

2.1.2 Zero Degree Calorimeter

Seventeen meters along the beam pipe in both directions from the vertex are the sites of the Zero Degree Calorimeters. They sit between the *pants* where the beam pipe splits in two directions for the incoming and outgoing beams. At ±17m they are well outside of the PHENIX experimental hall and located in the beam tunnel. The name *zero degree* derives from the fact that the beam axis passes directly through the detectors; diagrams can be found in Reference [18]. At these locations the magnets that bend the beams (called DX magnets) into their respective pipes effectively sweep away charged particles that would otherwise be incident on the ZDCs. Neutrons from collision spectators are incident on the ZDC and produce charged secondary particles from hadronic interactions in 24 tungsten plates, each 5.0 mm thick and 100 mm wide, and 187 mm tall. In between the plates are layers of fiber optic tubes in single file rows. Fibers are bundled together into one PMT, and the resulting signal is a measurement of incident energy deposited by neutrons. There are three ZDC assemblies in both forward and backward sites separated by layers of tungsten. ZDCs are used by the accelerator department to tune the beams and consequently identical sets exist at all four RHIC detector experiments [19, 20]. In the context of this work ZDCs are not used in making the final measurement values; however they were used extensively to study noise in the measurements of event plane angles and also feature timing signals that were used to study systematic uncertainties.

2.1.3 Shower Maximum Detector

Sandwiched between the first and second ZDCs (Sec. 2.1.2) on each side of the interaction region are the Shower Maximum Detectors (SMD-South). Each SMD is made of 7 vertically oriented and 8 horizontally oriented plastic scintillators (all 15 being illustrated

in Fig. 2.3). Each scintillator is comprised of three or four strips with triangular cross-sections (not pictured; described in detail in Ref. [20]) that each have a wavelength shifting fiber running axially though lengthwise. The fibers from each scintillator are attached to 15 channels of a 16 channel PMT [20]. Showers from neutrons incident on the ZDC tungsten plates are used in the SMD to locate the mass-centroid position. Figure 2.3 illustrates the method used to calculate the centroid which is taken to reflect the collision event plane.

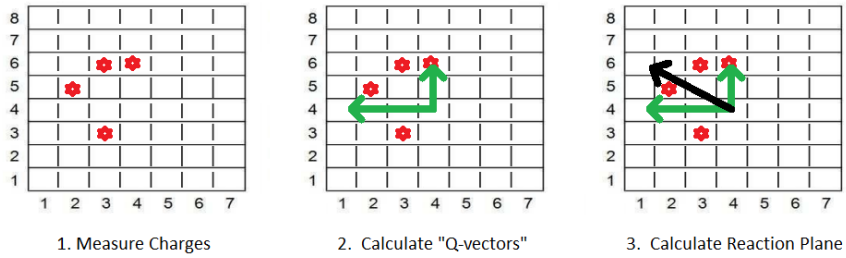

Figure 2.3: In each Shower Maximum Detector (SMD) 8 horizontal (7 vertical) scintillation units measure the vertical (horizontal) position of incident charges. The x and y *Q-vectors* corresponding to the location of each scintillator hit with respect to an average over many events (*centering*, Sec. 4.5.1) are weighted according to the amount of charge measured and added together. With additional *flattening* (Sec. 4.5.2) procedure an angle representative of the event plane is calculated.

2.2 Central Arm Detectors

2.2.1 Drift Chamber

The PHENIX Drift Chamber (DC) is used to measure the momentum of charged particles at mid rapidity. A drift chamber is a descendent of the *multi-wire proportional chamber* (MWPC) developed by Georges Charpak in 1968 [21, 22]. The main detecting elements in both DC and MWPC are wires. In the vicinity of a line charge, the electric field is proportional to the inverse of the radial distance. When particles traverse a wire chamber, they leave trails of ions and electrons that will in turn drift toward sensing wires due to an applied electric field. In the strong electric field near a wire, avalanches of ~10^6 additional charges occur, yielding detection efficiencies close to 100%. In particular, anode wires are used between cathode wires to separate out electrons as the preferred faster drifting charge

signal. The PHENIX drift chamber [23] measures the electrons' arrival time to the sense wire, which is then converted to a distance measurement using the electron drift velocity in the working gas of the drift chamber.

The PHENIX Drift Chamber consists of two mirror image arches (called East and West) each with 90° coverage in ϕ and ±0.35 in pseudorapidity ($\eta = -ln(tan(\theta/2))$, where θ is the polar angle). The central collision region has a magnetic field of approximately 980 mT that is parallel to the beam axis. The field is produced by two sets of concentric solenoids approximately 1.5 m in length and 1.25 m (3.75 m) in diameter for the inner (outer) coils. The DC arches are located at the outer edge of the central magnetic region so that charged particle tracks traverse through at their maximum bending angle. Track momentum is found indirectly using measurements of track ϕ position at 2.02 and 2.46 meters from the beam line. The angle of deflection is reconstructed assuming the track originated at the collision vertex and is inversely proportional to the particle's momentum. Both sides of the DC together use 12800 readout wires. Along with anode and cathode wires, the DC uses additional gate wires to shape the electric field in the region of the sensing wires and further to ensure isochron drift of the electrons through the electric field for best timing, and hence - position resolution. To eliminate left-right ambiguity, back wires are used to collect the charge from one side of the field cage before it reaches the sense wire. The geometry and drift paths are illustrated in Fig. 2.4 in blue for the charges being detected on the sense wires, and in yellow - for the ones that are collected at the back wires before reaching the sense wire. With the principal detecting medium being a 50-50% mixture of argon and ethane, the DC is highly efficient while minimally altering particle energy and trajectory [24].

2.2.2 Pad Chamber

Charged particle tracking systems in the central arm of the PHENIX detector provide 3D coordinates at multiple distances from the interaction point. One such tracking system

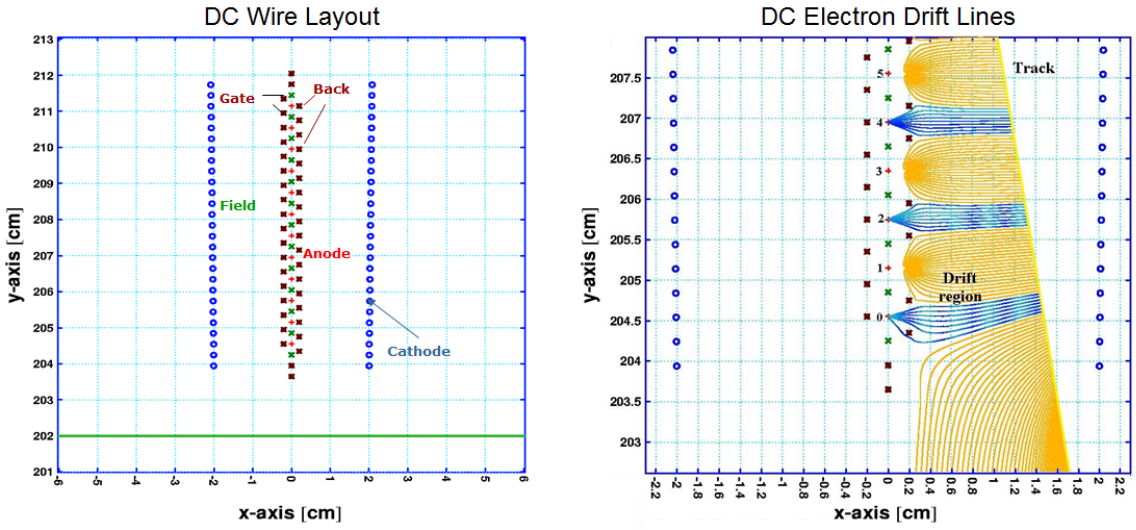

Figure 2.4: (Used with permission) Both left and right illustrations are made using the GARFIELD wire chamber simulation software. The left shows the various types of wires used, including *Cathode* wires used to create a uniform electric field together with the sensing *Anode* wires, *Back* wires for removing left-right ambiguity, *Gate* wires for shaping the electric field and providing uniform approach to the sensing wires, and *Field* wires for separating sensing wire regions. The illustration on the right shows drift lines of electrons from the track that are either sensed (blue) or repelled (yellow) [25].

is made up of Pad Chambers (PCs). The West arm has three PC layers at 2.5 (known as PC1), 4.2 (PC2), and 4.9 (PC3) meters from the beam line, each being comprised of rectangular sections that combine to form cylindrically positioned arches, and each having similar acceptance as the DC (Sec. 2.2.1). All layers of PCs are effectively outside the magnetic field region, so that particle trajectories are approximately straight. Using multiple position points enables reliable track reconstruction. The East arm has PC1 and PC3 layers, which mirror those in the West arm. The combined geometry of all layers in both arms has nearly 100 m^2 area [26].

Pad chambers, like drift chambers are an extension of multi-wire proportional chambers. Readouts are on small cathode plates or *pads* instead of the anode wires. Charges from cascades on the anode wires induce image charges on copper pads [27]. PHENIX PCs have 172,800 readout channels. This number would otherwise be three times as many except that multi-pixel geometry with multi-signal requirement allow for a reduction to a

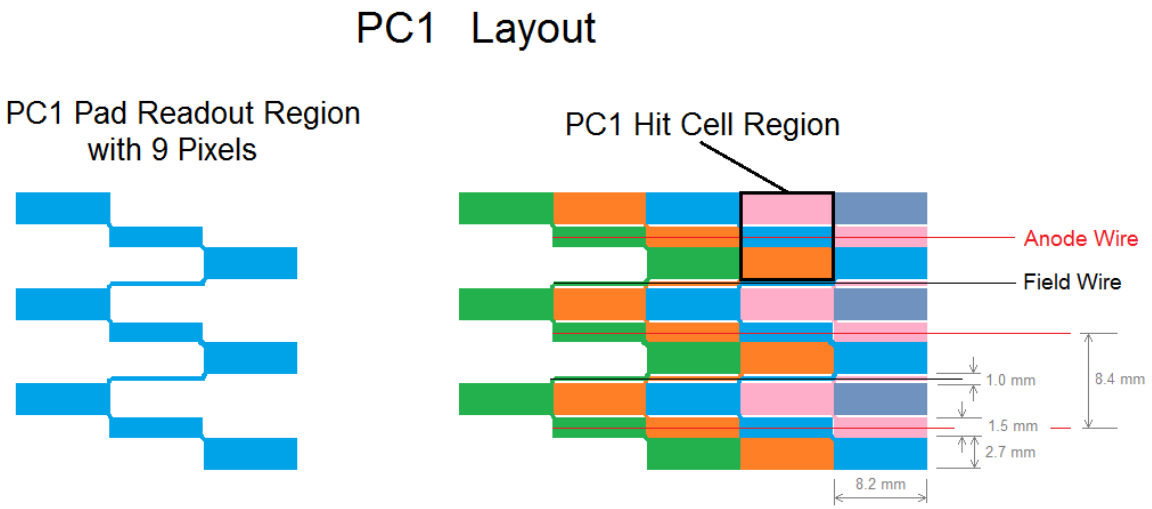

Figure 2.5: (Illustration is adapted from one found in [26]) Each pad readout (left) is shared by 9 cells and each cell (right) has 3 readouts, allowing for a reduction of readout channels by a factor of 3. A valid hit requires three readouts to fire, greatly reducing the influence of noise. The pixel width along the anode wire is smaller than that above and below in order to have similar amounts of charge induced in all three.

third of the readout channels without sacrificing single-track position resolution, and incurring an acceptable loss in double incidence resolution. Figure 2.5 illustrates the readout pad geometry and unit cell requirements. The three-fold signal needed for a track to be counted diminishes efficiency very little given the near 100% rate in each pixel. The approximately square cells vary in size between PC1, PC2, and PC3 according to the designed resolution requirements. PC1 uses 8.45 mm cells, PC2 14.2 mm, and PC3 16.7 mm [26].

2.2.3 Electromagnetic Calorimeter

At the outer edge of the central arms is the Electromagnetic Calorimeter (EMCal). As the name suggests, it measures energy and also position of incident particles. The EMCal has similar acceptance to the DC and is divided into two distinct detector types. The Lead Scintillator (PbSc) covers 135° and the Lead Glass (PbGl) covers the remaining 45°. Both PbSc and PbGl achieve the same purpose; however their designs are significantly different. The PbSc uses plates of lead 0.15 cm thick for hadronic interactions, behind which are 0.4

cm thick polystyrene scintillators. Three layers of lead and scintillators are followed by an outer PMT layer with fiber optics attached that traverses all three. The detecting principal is the same as that for the ZDC (Sec. 2.1.2) and their position as the back wall of the central arms allows fewer radiation lengths between detector layers. The approximate 5 meter distance to the beam line also provides a longer baseline for the EMCal's additional time of flight capability.

The PbGl detector uses PMTs like the PbSc. In this case the scintillator and lead are combined as *lead glass* rectangular bars 38 cm long. It detects Cherenkov radiation from particles moving faster than the speed of light in the material [28]. In PHENIX the EMCal on the West arm is entirely PbSc and the East arm is half PbSc and half PbGl. Components of this detector were previously used successfully for photon and π^0 measurements in the WA98 experiment at CERN.

2.2.4 Time of Flight

Time of Flight detectors (TOF) are used for particle identification. PHENIX has two varieties of TOF using different technologies. Both are in front of PC3 (Sec. 2.2.2), allowing the maximum distance to the interaction region (~4.9m). The East arm has a 22.5° ϕ acceptance segment with the full pseudorapidity width of the DC (Sec. 2.2.1) and an additional segment of the same ϕ acceptance and 0.175 pseudorapidity width, centered at midrapidity. TOF-East (TOFE) is a scintillator based detector using PMTs [29].

TOF-West (TOFW) has two 11.25° in ϕ sectors separated by a gap of approximately 14°, both having the full DC pseudorapidity range. 128 Multigap Resistive Plate Chambers (MRPCs) [30] each 12.7 cm by 53.3 cm and each having four lengthwise sensing strips and seven plates of glass separated by 230 micron gaps (shown in Fig.2.6). Fishing line is used to evenly separate the plates. The chambers housing the strips are located in an aluminum gas box with a mixture of 95% freon and 5% isobutane. The outer plates of the MRPCs are held at +/- 7 kV potential provided by two C.A.E.N. model SY127 power

supplies. Charged particles traversing the detector cause cascades of ionization of the gas in the gaps between the plates to be imaged onto readout strips [31]. Details of TOFE and TOFW usage for particle identification are explained in Section 4.4.

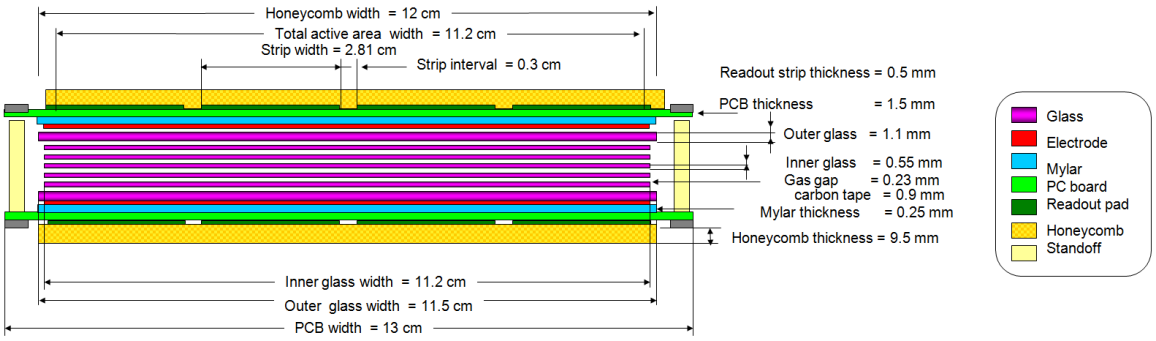

Figure 2.6: (From Ref. [32]) Time of Flight West uses 128 Multigap Resistive Plate Chambers each having four detecting strips. Chambers measure 12.7 by 53.3 cm. The view shown above is the short end of a chamber. Readouts are used on each end of each detecting strip.

Chapter 3

From Collisions to Publications

There is a significant progression of steps between heavy ion collisions in the PHENIX detector and the publication of a paper. With adequate prioritization of personnel and computing, the time between the actual collisions and papers/conferences can be about one year. On the other end it is not uncommon for further analysis to be done even up to 10 years after data is collected when new directions are sought.

Throughout the whole process at each step there are collaboration members inclined to help and who are actively working to improve data collection and processing in PHENIX at RHIC. Many of the most significant improvements in the PHENIX central arm spectrometers came about before I first worked at the detector in 2011. After this point additional detector upgrades have been installed in the forward pseudorapidity region. Improvements in operational efficiency and beam luminosity have continued their climb up until the present.

During RHICs annual running period which is generally around 22 weeks per year, PHENIX is manned by five shifters each with a unique role. There is a shift leader, a data acquisition (DAQ) operator, a data monitor, a voltage controller, and a shift assistant. The machine runs around the clock and three shift teams work eight hour periods dubbed Day, Evening, and Owl. Most shifters encounter problems and need to solve them or get assistance. In tracking down the source of a problem it is greatly beneficial to know the steps of data moving from detector to disk. To everyone else much of these details are meaningless and best skipped over.

The following description derives from 5 years of first-hand experience taking shifts at the PHENIX detector.

3.1 Within the first second of a collision

When RHIC is set up to collide heavy ions at 200 GeV, bunches of ions pass each other at the PHENIX vertex at a rate of 9.43 MHz. This forms the basic clock upon which most processes are timed. One of the beams is called Blue and the other Yellow, allegedly having been named by someone from Sweden. To be more precise, the clock most commonly used is associated with the Blue beam.

Out of 120 possible buckets or regions along the approximately circular beams, 109-111 buckets are filled with bunches of ions. Each bunch typically has about 10^9 ions. Most of the remaining empty buckets constitute the abort gap which is an area in the beam vacant of ions to allow enough time for magnets to be turned off and the beams to be dumped. Not every crossing produces a collision, and not every collision is desirable to record. PHENIX has an advanced trigger system for selecting which events to record. Its use in the context of this work is explained in Sec. 2.1. About one in a thousand crossings will produce an event that is stored in PHENIX, yielding a DAQ rate of about 10 kHz.

Events in PHENIX generally produce multiple tracks that are picked up by detectors using many different technologies, for instance Multigap Resistive Plate Chambers (MRPCs) and Photo Multiplier Tubes (PMTs). Initial signals are first conditioned in Front End Electronics (FEEs) which are typically mounted right onto the detecting hardware. The FEEs pass on the signal to the next stage of electronics called Front End Modules (FEMS) which are also inside the PHENIX detector hall. The FEMs have Analog Memory Unit (AMUs) which store charges corresponding to timing, energy, etc., and can buffer charges from multiple events. It can take many clock cycles before the trigger system communicates with the FEMs to either reset the AMU or digitize the stored signal. With the positive trigger signal the FEMs use an ADC (typically 12-bit) to measure the charge which also requires several clock cycles (it is therefore already impossible for two subsequent bunch crossings to produce collisions that end up being stored). The trigger system will alternatively send out a negative signal so that FEMs reset.

FEMs pass their signal along fiber optic lines that pass out of the experimental hall and into the rack room. In the rack room the fiber lines are attached to Data Collection Modules (DCMs). At this point the DAQ system in PHENIX is describable as being comprised of many separate smaller DAQ systems.

DCMs pass their data onto Sub-Event Buffers (SEBs) which are the first regular computers in the line-up. SEBs receive data from specialized interfaces and pass it along on gigabit ethernet. SEBs function as a buffer and send out data in response to requests further up stream. They are still dealing only with data from individual sub-systems.

Data from all of the subsystems gets merged into a single event at the next step in the chain. There are 64 Assembly Trigger Processor (ATP) computers each working to collect and assemble all of the information that characterizes an event in PHENIX. These computers were originally intended to be part of a higher level trigger system (this feature hasn't been used in recent years). Events vary in size significantly and can similarly vary in the time it takes to assemble them. As all 64 machines are individually assembling different events, when they pass their data further up the stream the events are generally not in the same order that the collisions occurred in.

The ATPs produce event data formatted in PHENIX Raw Data Format (PRDFs) files and transfers them to computers called buffer boxes. The buffer boxes are fast and reliable disk arrays that store terabytes of data for typically around 24 hours at a time.

3.2 Within 24 hours of a collision

The buffer boxes each have three partitions dubbed a, b, and c and the shift crew will alternate which partitions are being written to. Data is usually taken in hour-long segments called runs and the collider is filled with ions for collisions typically for 8-hour long fills. The term *run* is highly overloaded in PHENIX. A run can refer to the entire use of RHIC for one year (i.e. Run-12), it can refer to a sub-year period in which a particular species is collided (Cu+Au was collided for a 5 weeks run within Run-12) or again, the data taking

period of one hour.

After a minute or two of a run (an hour long *run*) some of the data in the buffer boxes is duplicated to a server used by the shift crew operating the detector. This feature is called *online monitoring* and is among the primary means for detecting problems together with the data acquisition control. With about a minute of delay between collisions and online monitoring data being seen by the shift crew, the operation of all subsystems can be inspected to assure a basic level functionality in near real-time.

Occasionally data from the buffer boxes is used for a *fast-production* that may allow access to a fraction of the whole dataset for quick analysis. This feature allows indepth analysis of data potentially within weeks of data collection and results made with fast production have on many occasions been shown at many conferences. In the case of the Cu+Au data collected in 2012, 20% was produced in fast production. Analysis works based on fast production are given *preliminary* approval, which allows use for conferences and prevents use in PHENIX publications.

In between fills the shift crew may switch the buffer box being written to. Immediately after the buffer box is switched, they will also begin a transfer of the data on the previously used buffer box to BNL's High Performance Storage System (HPSS). HPSS is in a different building within BNL about 2.5 km from PHENIX. At the time of this writing the data is transferred to HPSS over two aggregated 10-Gbit fiber links. An average of about 15 TB of data are sent to HPSS per day.

3.3 After 24 hours

When RHIC is running heavy ions, HPSS accumulates petabyte sized data sets each year. HPSS stores PRDF files on magnetic tapes in a large robotic carousel. As this data is essentially the digitized signal output of subsystem detectors, it is not immediately usable to most physicists doing analysis work. There is a lengthy and CPU intensive reconstruction process that takes signal input from the many subsystems and turns the data into more

accessible information characterizing each event and each detected particle. For instance signals from the Drift Chamber and first Pad Chamber are used to distinguish individual tracks and calculate their corresponding momentum. This process can be described as being a work of pattern recognition and is significantly CPU intensive. For heavy ion runs, such as Au+Au at 200 GeV, data taken over the course of a week will later require about a week of processing time.

Presently PHENIX has upwards of 15000 computers to use for reconstructing and analyzing data. The hard drives of these machines form a common distributed file system called dCache (presently 7 PB) which is augmented by the system of tape drives. A priority scheme based on how recently a segment of data has been used as well as how frequently it has been used allows a speedier access by balancing the faster disks with the slower tapes. So that CPUs are used efficiently and not waiting on read accesses, data is pinned to disks for the duration of the reconstruction time.

The reconstruction process reads PRDF files and makes Data Summary Tape files (DSTs, the name is 25+ years old) which are compressed ROOT files. DST files are about 30% the size of PRDFs, and after production they are stored once again on tapes.

When a physicist wishes to do analysis work on PHENIX data, they first write a specialized script called a taxi to retrieve it from the tapes. Most likely they will only need a small fraction of all of the parameters stored in the DST files. For example, a track's momentum may be desired and the hit position within a specific subsystem may be unneeded. The PHENIX Collaboration has a designated taxi driver / train conductor to whom taxi requests are submitted. The taxi driver pins the relevant DST files to dCache and runs the requester's taxi code. The data retrieved from the requester's code is written to their personal disk space, generally located on a different partition within the same disk array.

3.4 Data Analysis

Data retrieved from the taxi process can be encapsulated into histograms and therefore requires very little disk space and minimal processor power for analysis. As was the case with this analysis, the taxi data totaled about 1 TB. Many passes parsing through the data is done quickly with the Condor batch processing system. Cu+Au in PHENIX Run-12 for example was taken in about 400 runs, which makes for an obvious delineation of data for batch jobs.

Analysis work typically constitutes months and even years and is distinct to the type of physics sought, the data set analyzed, and varying parts of the detector used. Typically a researcher at a university will first share results in their local group where cross checks, vetting, and refinement takes places. From here the next step is typically to present in a local working group, which is a basic part of the collaboration structure. In the context of this work the local working group is Photons, LVM, Hadrons, and Flow (PLHF) and meetings are held weekly. About five presenters on average from different institutions will give 15-30 minute presentations in each working group meeting.

Once an analysis effort is able to demonstrate physics findings worthy of publication, a request is made at the group meeting to form a Paper Preparation Group (PPG). PPGs are typically 4-8 physicists and one or two chairs or co-chairs.

After a paper is drafted, it is sent out to the entire collaboration for an initial two week review period. During this time anyone can formally comment on the paper. Comments vary from minor syntax and semantics suggestions to large structural changes, and even challenges to physical assertions. The commenting process and submission of the paper to the collaboration are both done by collaboration wide email. An Internal Review Committee (IRC) of three independent PHENIX members is created to oversee the comment process and ensure that all comments are addressed. The PPG will compile the comments and write responses to each with an explanation of if/how the suggested change in the paper was implemented.

After the first review period is over and the existing comments are addressed the PPG together with the IRC's oversight will send out a second draft of the paper. A second comment period of one week ensues. After comments from the second review are addressed and the spokesperson has reviewed the draft and signs off before the paper is submitted to the arXive and journal. All *members in good standing* who have contributed substantially to the data used in the paper, either from taking shifts at the detector, having made calibrations, simulations, etc. in the data process are included in the list of authors.

Chapter 4

Analysis Procedure

4.1 Run Selection

Between May 15 and June 25 of 2012 (41 days total, 38 for physics) PHENIX collected 430 runs of data, at approximately an hour a piece. They are designated with run numbers from 372403 - 377310 (most of the numbers in the range do not constitute physics runs). Run data is stored in 8360 total files. There are tests done to assure the quality of the run data used (QA tests) which are explained in the subsequent sections. Of the 430 total runs collected, 401 pass the tests and are used in the analysis.

4.1.1 Reaction Plane - Quality Assurance

The *reaction plane angle* is the azimuthal angle of the impact parameter vector perpendicular to the beam axis. The reaction plane angle (illustrated below in Fig. 4.1) is approximately known due to measurements with forward detectors (Sec. 2.1) and is subsequently used with central arm track angles (Sec. 4.5) to measure anisotropic flow.

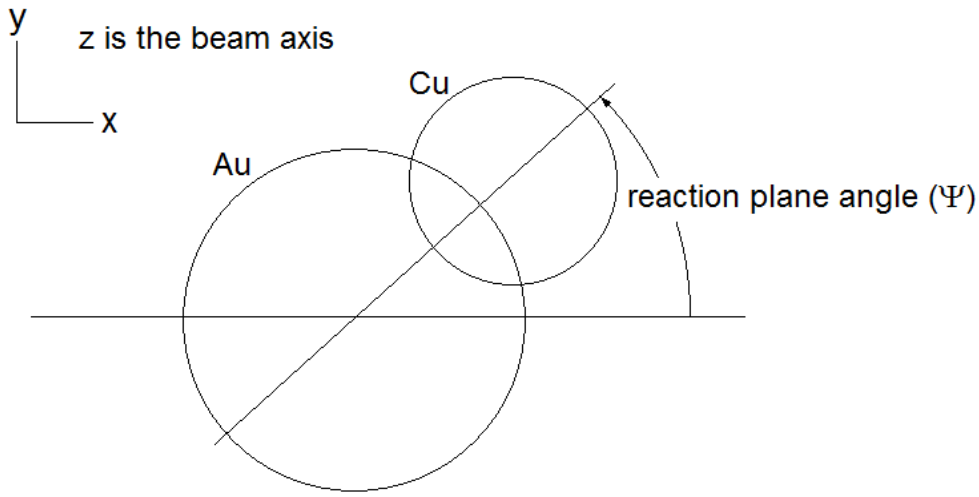

Figure 4.1: The reaction plane angle is the orientation of the collision with respect to the lab frame.

Because all angular orientations are equally probable, the distribution of the reaction plane angles as measured is ideally flat from $-\pi$ to π. A flattening procedure (Sec. 4.5.2) is used to mathematically correct for detector imperfections that yield a non-uniform distribution. After the flattening procedure the distribution is compared to a constant and a $0.2 < \chi^2 < 3.0$ cut is made eliminating an additional 9 data runs.

4.1.2 Subsystem - Quality Assurance

While taking data in PHENIX, certain detector subsystems may occasionally experience high voltage trips. It is further possible for there to be a small time interval between the trip and the stopping of data acquisition. For this reason offline quality assurance is needed. A simple indicator to aid in removing runs on account of equipment failure is to look at the average number of tracks per event in each run. Fig. 4.2 illustrates the type of threshold cut used.

4.2 Event Selection - Minimum Bias

Only events with collisions direct enough to have inelastic collisions are of interest in the context of this analysis. For this reason an event selection is used that requires a minimum threshold of charge to be measured in the BBC (Sec. 2.1.1).

Additionally a requirement is made that collisions are used only when their vertex position is ±30 cm from the center of the detector, or z=0 point. Collisions outside of this range are less suited for study because associated track reconstruction efficiency diminishes given the set of subsystems used in this analysis. Both the minimum BBC charge and z-vertex limits make up the *minimum-bias* event cut. The Cu+Au run in 2012 collected 7.6 billion minimum bias events.

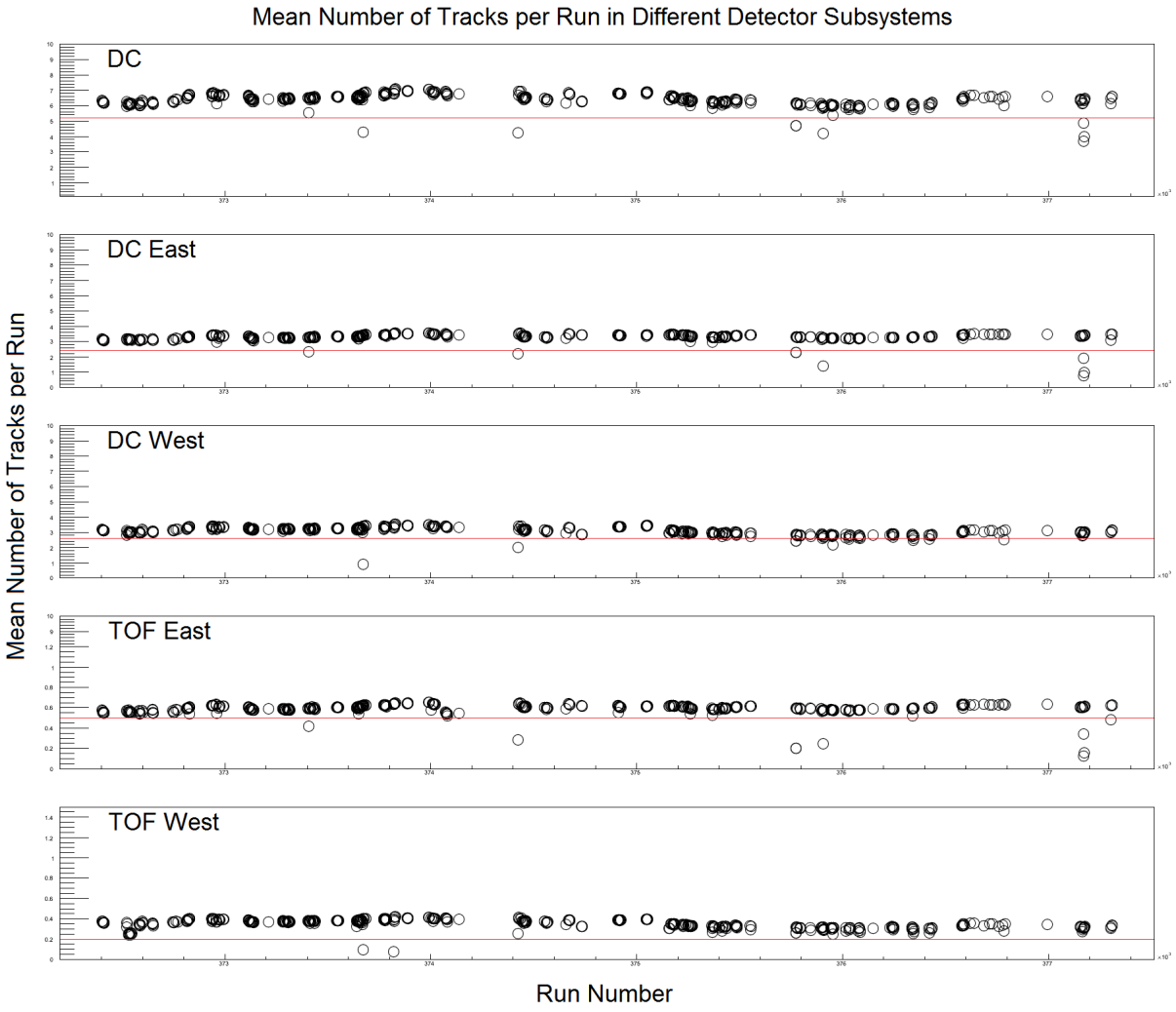

Figure 4.2: The above quality assurance plots show actual numbers of tracks per event in each run. The threshold lines (red) are only representative, whereas the actual lines used in this analysis are a little higher in each case. A total of 20 runs were marked *bad* and excluded from this test.

4.3 Track Selection

4.3.1 TOF Track Matching Quality Cut

Tracking of charged particles in the PHENIX central arms is performed using the DC and PC1. The tracking algorithm is based on a combinatorial Hough transform and is highly efficient for particles with $p_t > 200$ MeV/c [33]. The algorithm uses information about the z coordinate of the vertex location based on the BBC measurement and assumes that all particles that are detected in the drift chamber originate from this vertex. There-

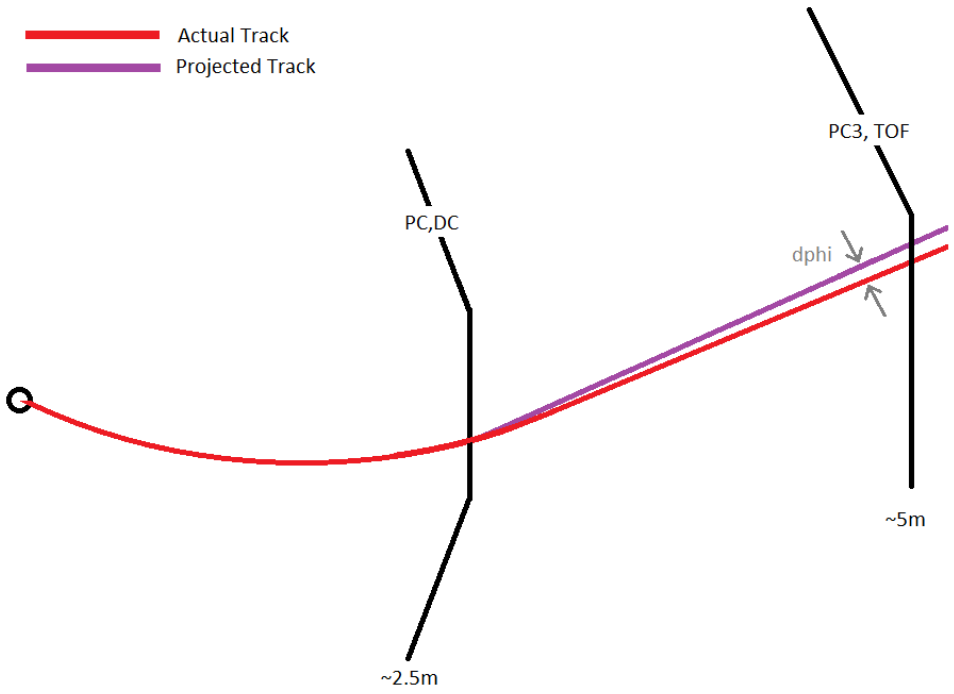

Figure 4.3: Illustration of matching technique that compares real hits in inner and outer detector layers with the mathematical projections from inner track hits. The comparison is used in a cut for the purpose of eliminating background tracks.

fore, of produced particles coming from the vertex, secondary particles from decays of produced particles, particle interactions with detector medium, tracks from cosmic rays and environmental radiation, may also be reconstructed, albeit with incorrect momentum. For the purposes of this analysis work, signal tracks are approximately those coming from the primary vertex and background tracks are everything else. One method for separating the signal from the background tracks is called *track matching*. As illustrated in Fig. 4.3 tracks are first assumed to come from the primary vertex. Their signal is detected in an inner layer of detectors, DC and PC1. A mathematical projection is then computed as to where the track will hit an outer layer of detectors at approximately twice the radius, such as PC3 and TOF. In order to associate or *match* hits in the inner layer of detectors with hits in the outer layer, the difference is taken between the outer layer hit position and the track projection. This difference, or *residual*, is found in both the ϕ (Fig. 4.4) and z directions and is generally expected to be greater for background tracks. A cut of two standard de-

viations (2-σ) width on the distribution is used for track purity (Sec. 4.3.2). Before this cut is made, quality checks of individual strips of TOFW (and slats of TOFE) are made by looking at residuals in each. For this initial quality assurance cut, only tracks between 1.0 and 1.5 GeV/c are used. Tracks are separated into positive and negative bins and $d\phi$ and dz residuals are plotted for each of the 512 TOFW strips (and 960 TOFE slats). Figure 4.4 shows graphs of residuals of positive and negative tracks from a strips that passes the quality assurance, and from a strip that does not.

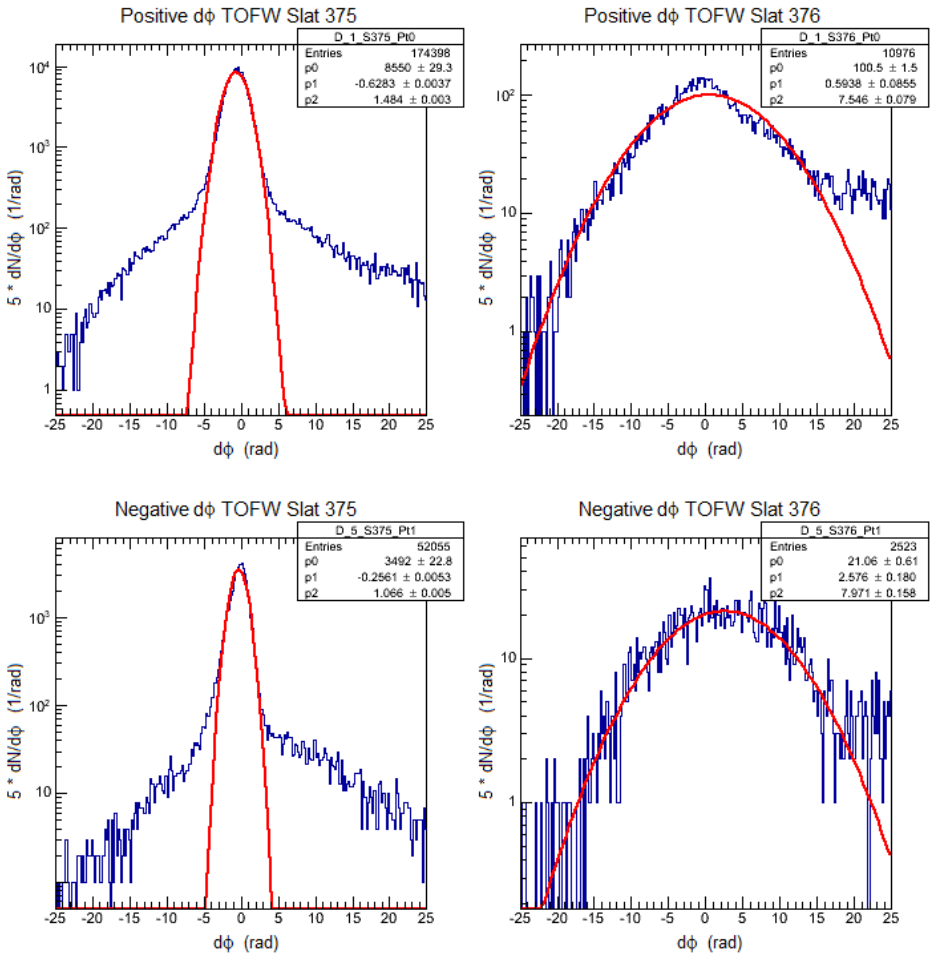

Figure 4.4: The top left and bottom left are $d\phi$ residuals for positive and negative tracks respectively in TOFW strip number 375. The corresponding plots for TOFW strip 376 are plotted on the right. Strip 376 is eliminated using this cut.

4.3.2 TOF and PC3 Track Matching Cut

A 2-σ width matching requirement is made for tracks in TOF, PC3, and EMCal detectors. Each histograms is fit with a double Gaussian functions and must be individually inspected. Tracks are separated into 10 zed bins (DC, PC1), 6 centrality bins, and 17 p_T bins between 0.4 and 5.0 GeV/c having variable bin width ranging from 100 to 500 MeV/c, with the smaller bins used at low p_T. In each of the individual 1020 bins, $d\phi$ and dz are fit separately, also for positive and negative tracks, for PC3 and TOF separately, and lastly East and West separately, giving 8160 fitting histograms. The full fitting process is then repeated to insure the correctness of the procedure and gauge the fitting accuracy. A sample $d\phi$ residual histogram is shown in Fig. 4.5 for negative tracks detected in PC3 East, DC/PC1 zed between -70 and -57 cm, and p_T between 0.4 and 0.5 MeV/c.

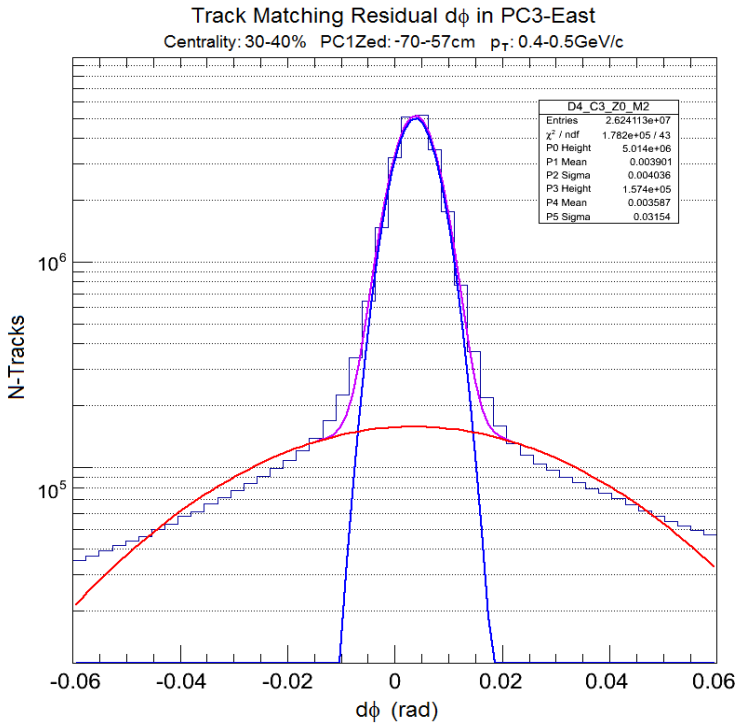

Figure 4.5: Histogram of $d\phi$ residual. Violet shows the 2-Gaussian fitting function, red shows the extracted background, and blue the extracted signal.

An added level of complexity and refinement to the matching scheme described above is the fitting of mean and standard deviation as functions of p_T. This allows functions to

be used for the matching cuts instead of discrete values in each p_T range and further for extrapolation to regions of weaker statistics. Depending on the uniformity of the $d\phi$ and dz track matching data, the process of normalization and fitting can be done iteratively. A single pass is used in this analysis.

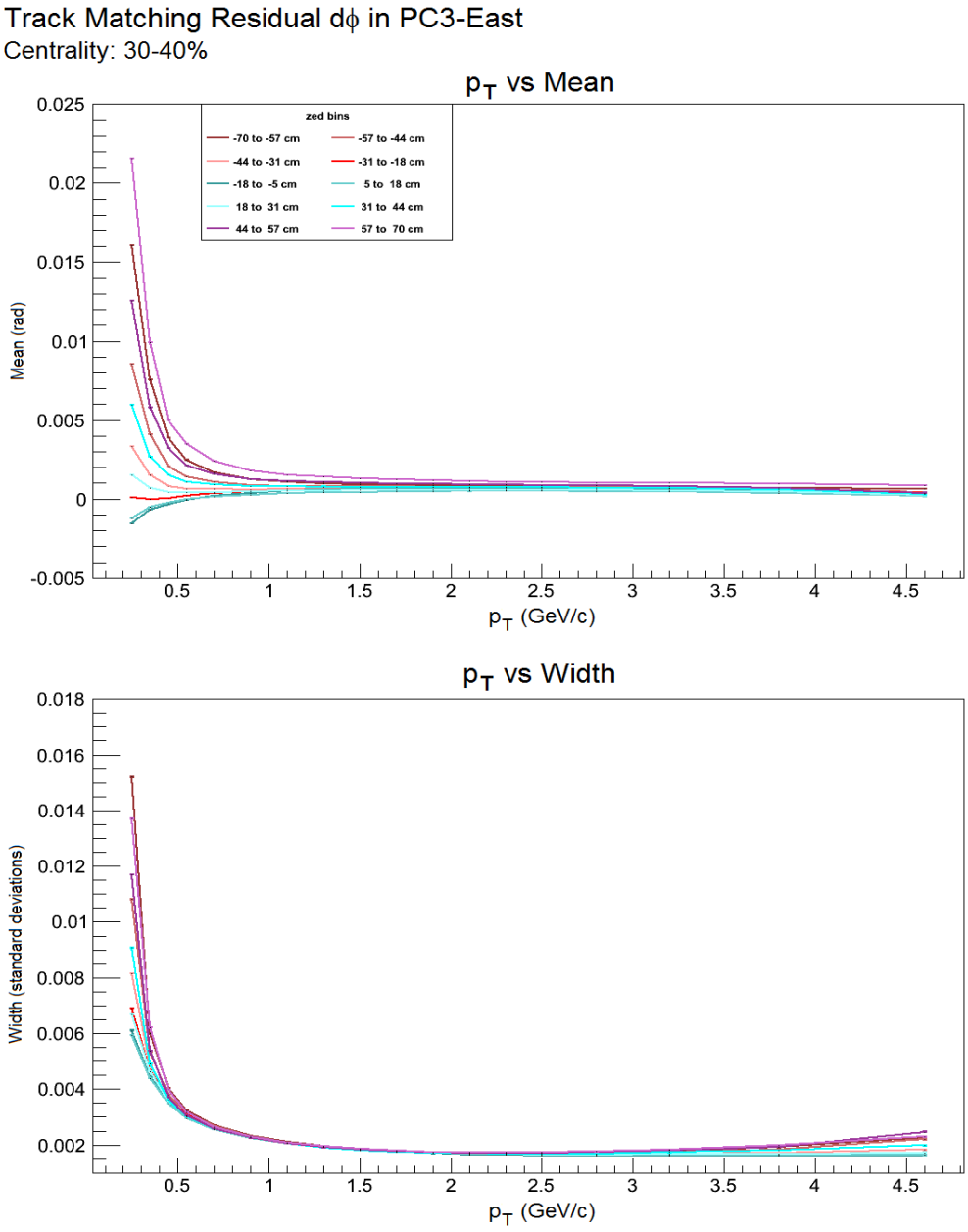

Figure 4.6: The top plot is the *mean vs* p_T plot and the bottom plot is *width vs* p_T. In each, the different colors represent different DC/PC1 zed bins. The mean and width of the blue curve plotted in Fig. 4.5 contributes one data point on each of these graphs.

Instead of using a fitting function here (a polynomial for example) a 16 segment piecewise linear function in p_T is used for finding both mean and (width) values. There are 960 of these functions used arising from finding either mean or width, from 10 zed bins, 6 centrality bins, positive and negative tracks separately, TOF and PC3 separately, and East and West separately. Using the mean and width values from these functions the residuals of each track are normalized to have a mean of 0 and width of 1 using Eq. 4.1. Lastly a 2-σ (2 standard deviations) width cut is applied to limit the influence of the background. The resulting enhancement of identified particle peaks from PC3 and TOF matching is seen in Figure 4.7. EMCal matching (Sec. 5.2) is introduced to gauge the systematic uncertainty associated with PC3 and TOF matching and makes only nominal difference in track number.

$$sd\phi = \frac{d\phi - mean}{width} \tag{4.1}$$

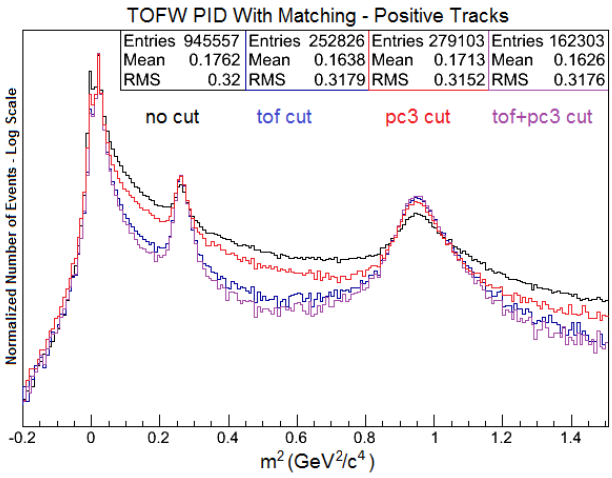

Figure 4.7: Track matching reduces background contamination in species peaks. The black curve is without matching, red is with PC3 matching, blue with TOF matching, and violet with PC3 and TOF matching cuts combined. Each is normalized to have the same area.

4.4 Timing Calibrations and Cuts

4.4.1 Strip Timing Quality Assurance

Along with an initial TOF based quality cut that looks at the average number of TOF tracks per event in each run (Sec. 4.1.2), an additional quality assurance test is done on each strip (slat) of TOFW (TOFE). Runs at the beginning, middle, and end of the run are sampled and tracks are selected with a narrow p_T range between 1.0 and 1.1 GeV/c. From here the track time of flight (the timing difference between the collision time as measured by the BBC and the particle's incidence in the TOF detector) can be used to see pion, kaon, and proton peaks. The expected time for pions is subtracted to determine if there are additional timing offsets between the BBC, which provide the start time for the time-of-flight measurement, and the TOF detectors. If the timing is correctly calibrated, the pion peak is centered at 0. (Eq 4.2). The results for each TOFW strip are inspected visually to verify the expected profile is seen and also to eliminate malfunctioning strips. As seen in Figure 4.8 the minimal statistics seen in malfunctioning strips would otherwise influence the final result very little. This test is nevertheless necessary for basic verification of strip performance.

$$\Delta t = t_{TOF\ incidence} - t_{collision} - t_{pion\ expected} \tag{4.2}$$

$$t_{pion\ expected} = \sqrt{\frac{m_\pi^2}{p^2} + \frac{1}{c^2}} \tag{4.3}$$

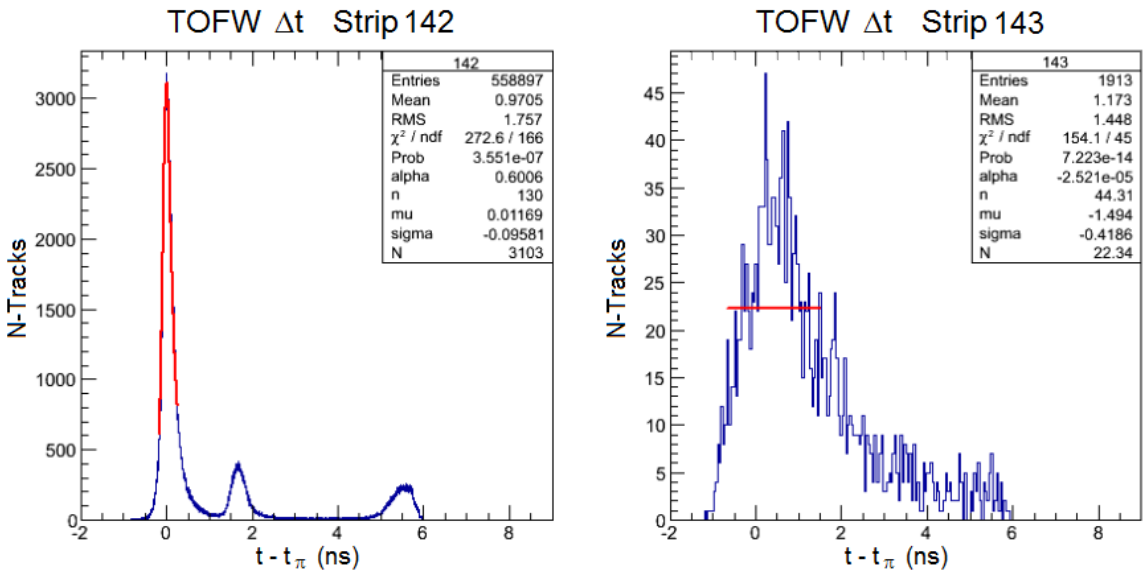

Figure 4.8: On the left is an example of a TOFW strip with timing characteristics that pass the quality assurance test, and conversely the right fails. The plots are made by limiting tracks to a narrow transverse momentum range of 1.0 to 1.1 GeV/c as measured with the DC. In the left panel the tallest peak is from pions and subsequent peaks to the right are kaon, then proton (qualified later in this work).

4.4.2 Strip by Strip and Run by Run Timing Calibrations

Once the track selection cuts are made there are a number of calibrations necessary before particles can be separated according to their species. The majority of hadrons in heavy ion collisions at RHIC are pions, making their great abundance relative to kaons and protons an easily identifiable signature of their arrival time.

Calibration of TOFW timing for the Cu+Au dataset was done for use in this work. The corresponding calibration of the TOFE dataset was done earlier and in support of any future analysis that would potentially make use of TOFE. The procedures used by the TOFE and TOFW team are qualitatively the same. With TOFW however, the first timing calibration is a generic one that can be used on any central arm datasets. It compensates for the known differences in distances to the 512 individual strips that comprise TOFW. The implementation is trivial, timing offsets are read in from a look-up table common to all datasets and track timing information is adjusted according to the strip the track is incident

upon.

After the initial generic timing calibration, a run-by-run timing calibration is done that corrects for changes during the data taking. Such changes could include a clock change, BBC calibration, or moving a central arm carriage. For this second calibration, a track cut is again put in place to only admit tracks with p_T between 1.0-1.1 GeV/c. For each run the timing adjustment is found by fitting the pion peak and shifting the timing so that the pions arrive at the time expected, given their path length traversed and velocity calculated from the DC momentum.

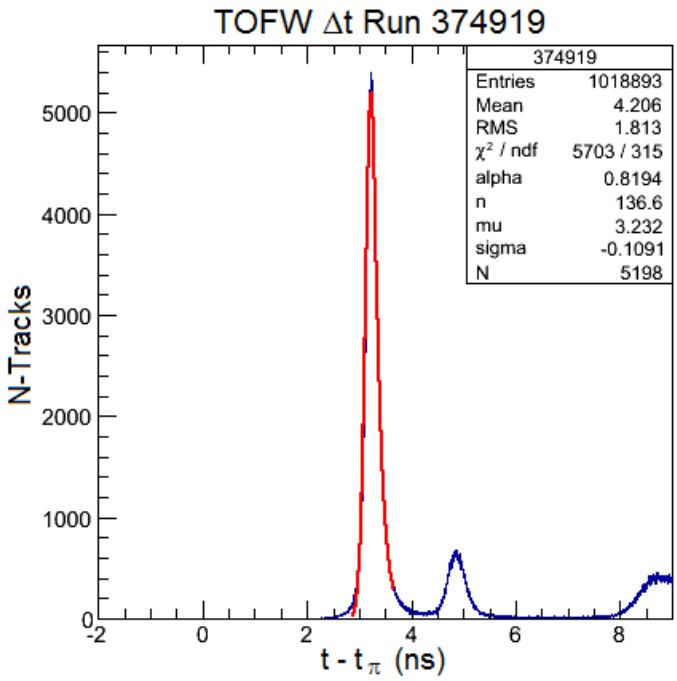

Figure 4.9: An example plot of a run-timing calibration in which a timing offset of ~2.9 ns is found corresponding to the pion peak. The Kaon peak is around 5 ns, and the proton peak is around 9 ns.

Each successive correction in the iterative slat-by-slat, then run-by-run, slat-by-slat, run-by-run process yields smaller and smaller corrections. The first generic strip-by-strip correction has global timing offsets common to all slats typically between 1-10 nanoseconds due to the dependency of the BBC timing, and further strip-by-strip variation of less than half a nanosecond. The first run-by-run calibration has offsets of the order of nanoseconds however variance between runs is approximately 500 picoseconds (ps) and results

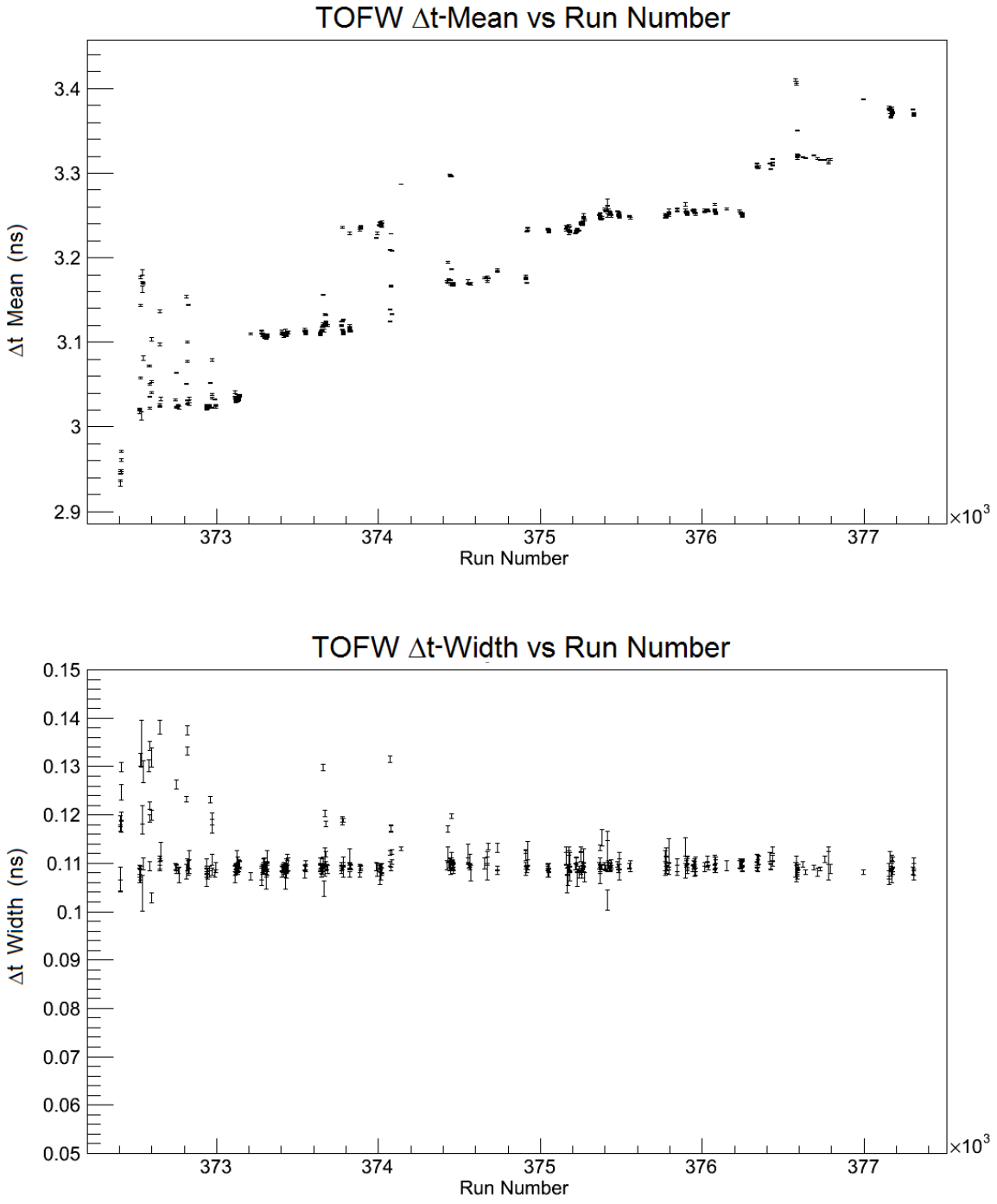

Figure 4.10: Run by run calibration timing offsets for TOFW (top) and the widths of pion peaks (bottom).

in timing resolution around 110 ps (Fig. 4.10). The second strip-by-strip calibration has offsets generally between ±50 ps. Strip resolution varies significantly between 70 and 150 ps (Fig. 4.11). The second run-by-run calibration finds timing offsets between ±10 ps and resolution for most runs between 86 and 94 ps (Fig. 4.12).

An additional third strip-by-strip and run-by-run iteration gives corrections of similar magnitude to the second iteration which indicates the variance is due to statics and fitting. Further, by the second run-by-run calibration the timing corrections are an order of magnitude smaller than the widths of the pion peaks. The process is therefore limited to two iterations.

4.4.3 Particle Identification - Mass Squared Fitting

In the timing plots shown in Figure 4.9, the profile of species is already seen in their time-of-flight to the outer West wall. The tracks featured in these plots are limited to 1.0-1.1 GeV/c and are timing measurements without a definitive link made to their particle species. To this end the timing information is mated to the tracks momentum and path length to find the *mass-squared* term using Equations 4.4, and 4.5.

$$p = mv\gamma \tag{4.4}$$

$$m^2 = \frac{p^2}{c^2}\left(\frac{t^2c^2}{L^2} - 1\right) \tag{4.5}$$

Gamma (γ) is the Lorentz factor, v is the velocity, L is the path length traversed, and c is the speed of light.

Figure 4.13 shows particle species are readily identifiable according to their mass-squared. Particle identification cuts are done separately for positive and negative tracks,

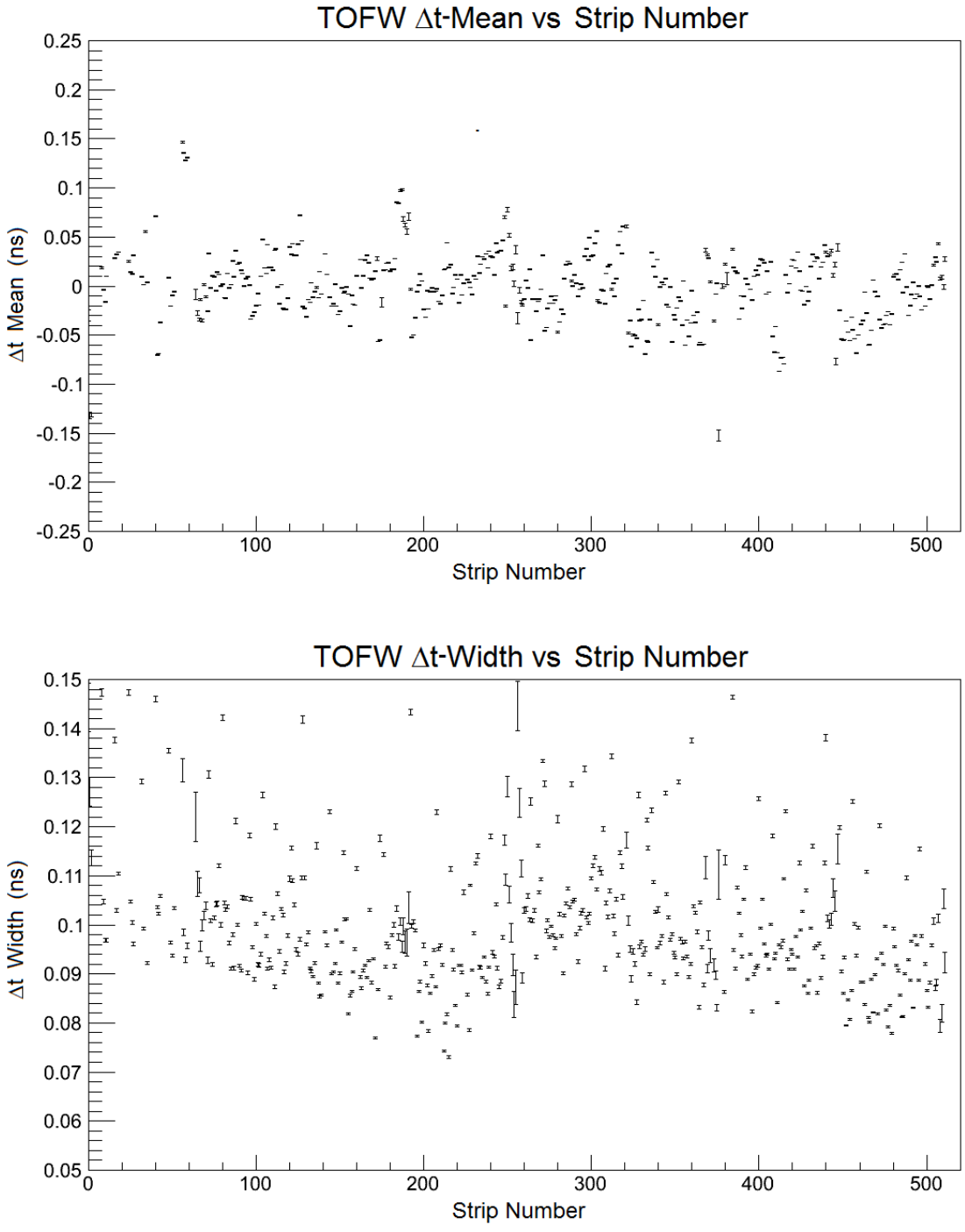

Figure 4.11: Slat by slat calibration timing offsets for TOFW (top) and the widths of pion peaks (bottom).

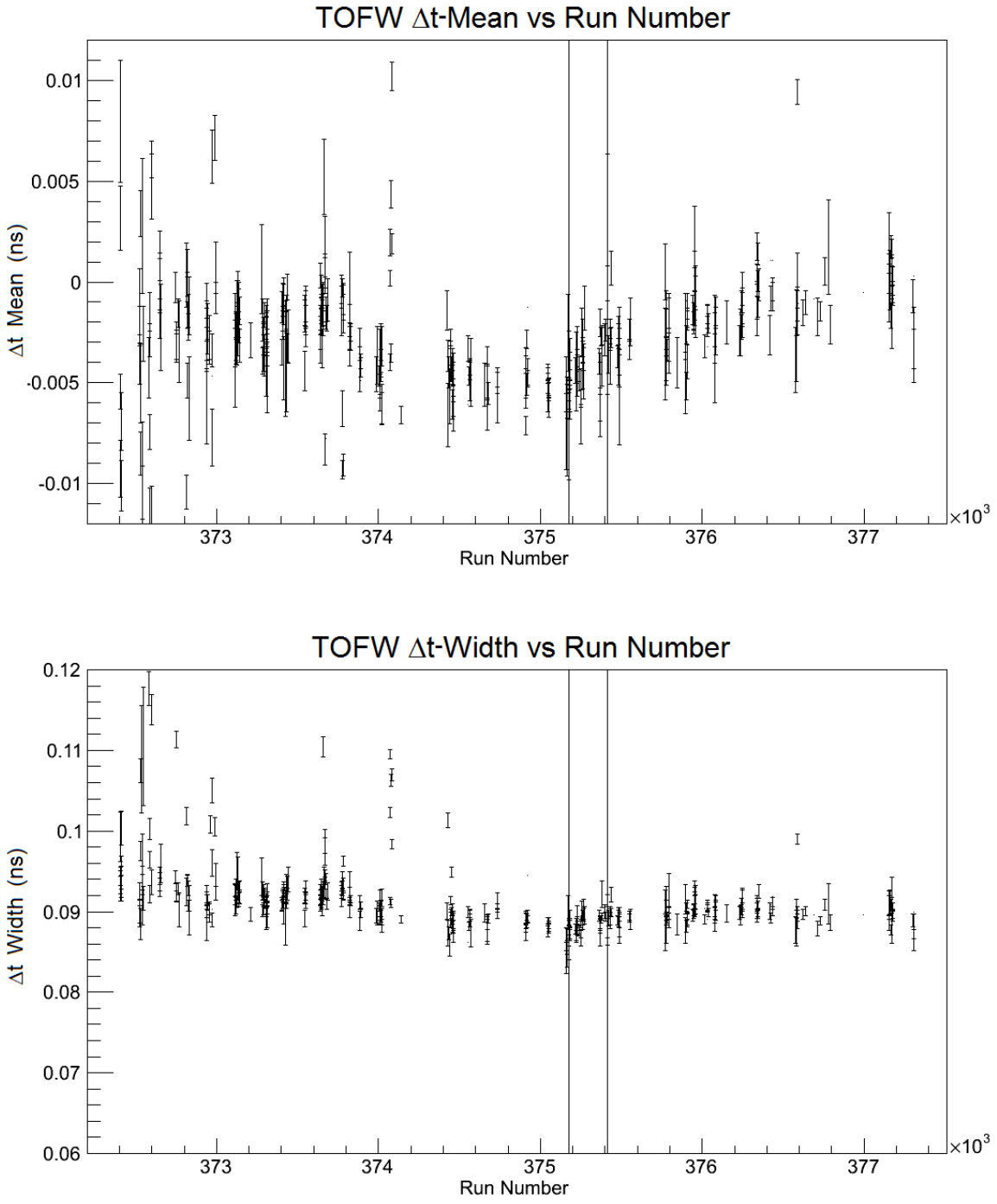

Figure 4.12: The second iteration of run-by-run calibration timing offsets for TOFW (top) and the widths of pion peaks (bottom).

as well as separately using TOFE and TOFW. The upper left panel is m^2 of positive tracks detected in TOFE on the vertical axis vs p_T from the DC on the horizontal axis. The upper right panel is the same measurement using TOFW, and the bottom panels show the corresponding measurements for negative particles. In each panel the sharp red streak in the lower left corner are the pions, immediately above is a kaon band in yellow, and then just beneath 1 GeV/c are the protons. Lastly, a wide band in mass-squared corresponding to deuterons or anti-deuterons is seen between 3 and 4 GeV/c.

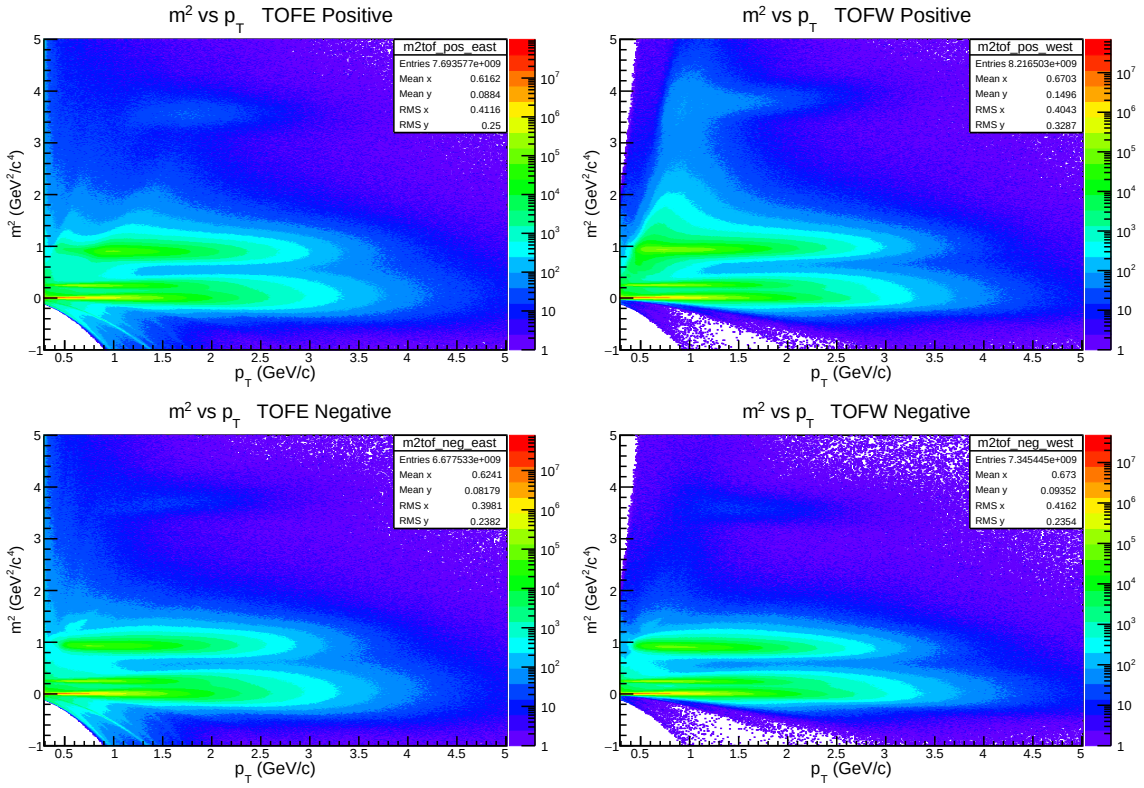

Figure 4.13: The mass-squared vs p_T plots of positive (upper) and negative (lower), East (left) and West (right) tracks. in mass-squared, corresponding to pions, kaons, (anti)protons, and (anti) deuterons can be identified. Bands in mass-squared, corresponding to pions, kaons, (anti)protons, and (anti) deuterons can be identified.

In order to separate the species, a cut is implemented at two standard deviations around the mean value of each species peak. Mass-squared data are first divided up into 100 MeV/c p_T bins. Due to the asymmetric shape of the species peaks a *Crystal Ball* function (Ref. [34]) is used for each, that consists of a piece-wise Gaussian curve on one side of the peak

and an exponential tail on the other. The pion and kaon peaks are fit together with a double Crystal Ball function so that at high p_T their mutual influence can be better accounted for when overlap is substantial. Proton peaks are minimally influenced by pollution from other species within the range of transverse momentum sought in this work. Therefore, a single Crystal Ball function is used to fit the proton peak. Example fittings at low, medium, and high p_T are shown in Figures 4.14, 4.15, and 4.16. In each case the Crystal Ball fitting function results are drawn in red and the extracted Gaussian (where visible) is drawn in blue to a width of 2-σ. Additionally, deuteron peaks are fit with a Gaussian distribution plus an exponential for the background (Fig. 4.17). Although deuteron fittings are not used for measurements in the context of this work, their fittings affirm that pollution of protons by deuterons is negligible.

The means and widths of pions, kaons, protons (anti-protons) peaks are fit as a function of p_T using Equations 4.6 and 4.7, examples of which can be seen in Figures 4.18 and 4.19.

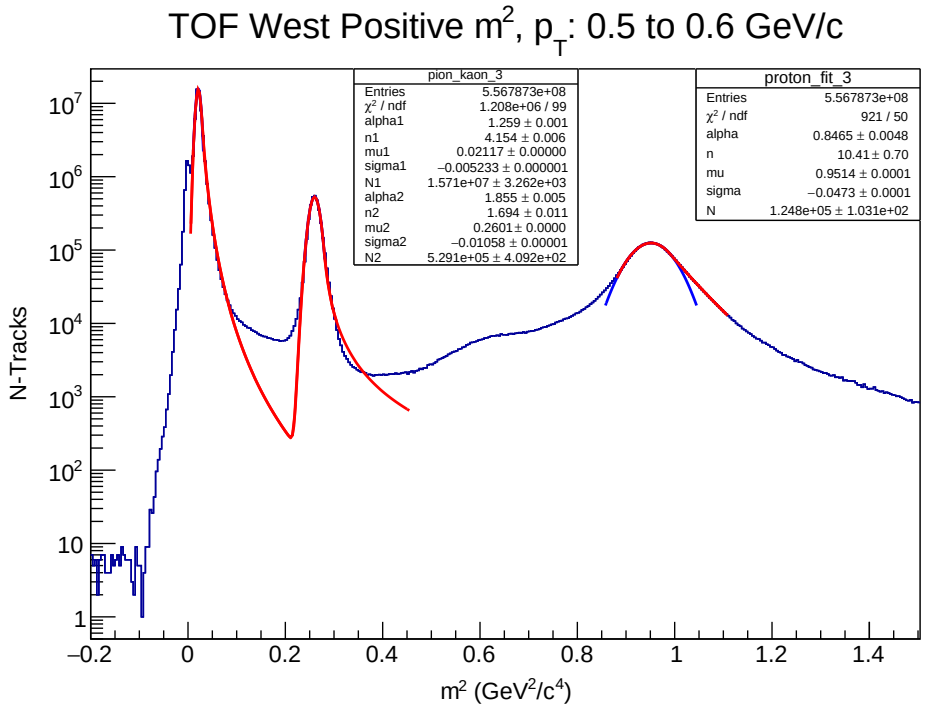

Figure 4.14: An example low p_T mass-squared fitting plot for positive tracks in TOFW.

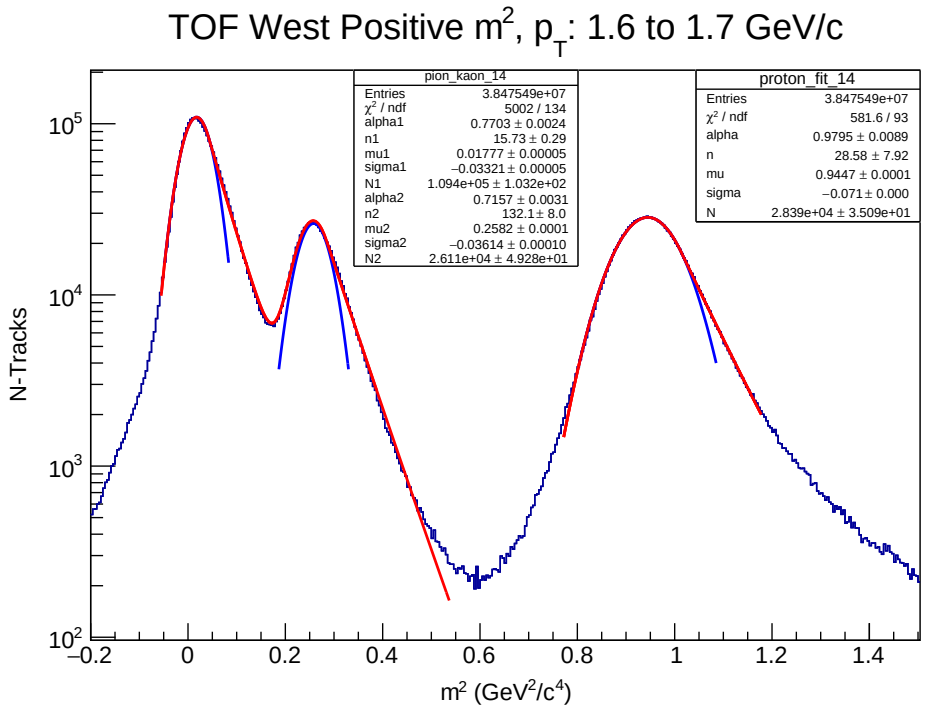

Figure 4.15: An example mass-squared fitting plot at medium p_T for positive pion, kaon, and protons in TOFW.

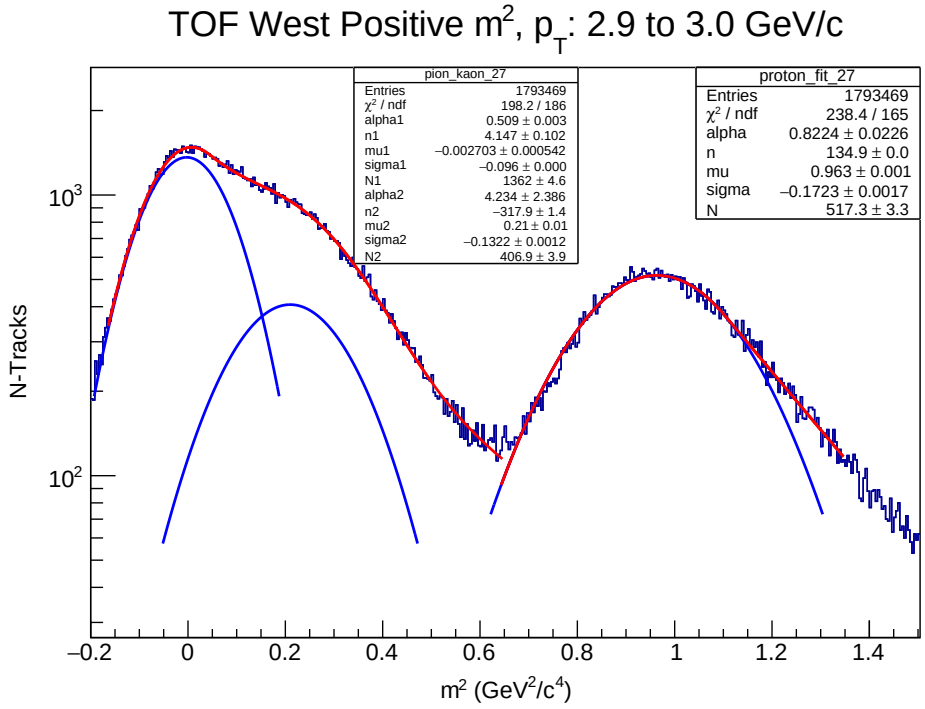

Figure 4.16: An example mass-squared fitting plot at high p_T for positive pion, kaon, and protons in TOFW.

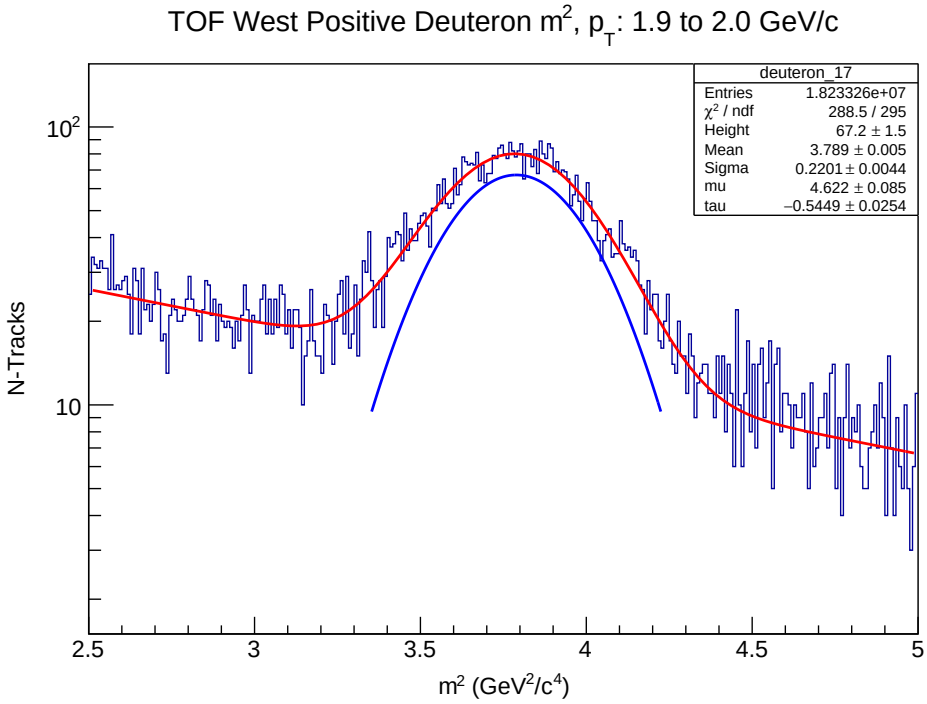

Figure 4.17: An example mass-squared fitting plot at medium p_T for positive deuterons in TOFW.

$$mean(x) = m_0 + m_1 x + m_2 x^2 + m_3 x^3 + \frac{m_4}{\sqrt{x}} + \frac{m_5}{x} \tag{4.6}$$

$$width(x) = w_0 + w_1 x + \frac{w_2}{x} + w_3 x^2 + w_4 x^3 + \frac{w_5}{\sqrt{x}} \tag{4.7}$$

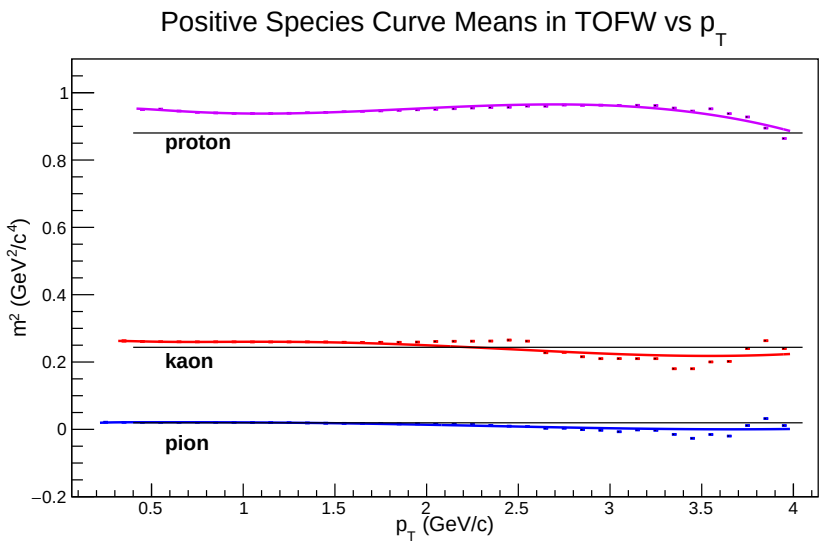

Figure 4.18: The mean values of each peak are fit as a function of p_T using Eq. 4.6. The accepted mass-squared values are also drawn for reference.

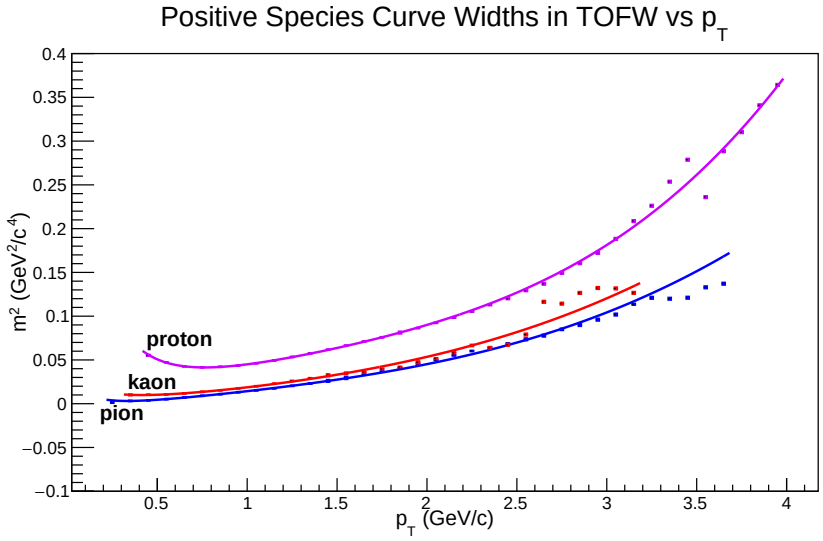

Figure 4.19: The width values of each peak are fit as a function of p_T using Eq. 4.7.

Using the mean and width fitting functions (Eq. 4.6,4.7), a two-standard-deviation cut is used for acceptance of each species and additionally a two-standard-deviation veto is used to insure species purity. For example, a pion that passes the PID cut will be within two standard deviations of the mean of the pion mass-squared distribution and further than two standard deviations from the mean of the kaon distribution. The resulting bands of tracks that remain following the two cuts are seen in Figure 4.20.

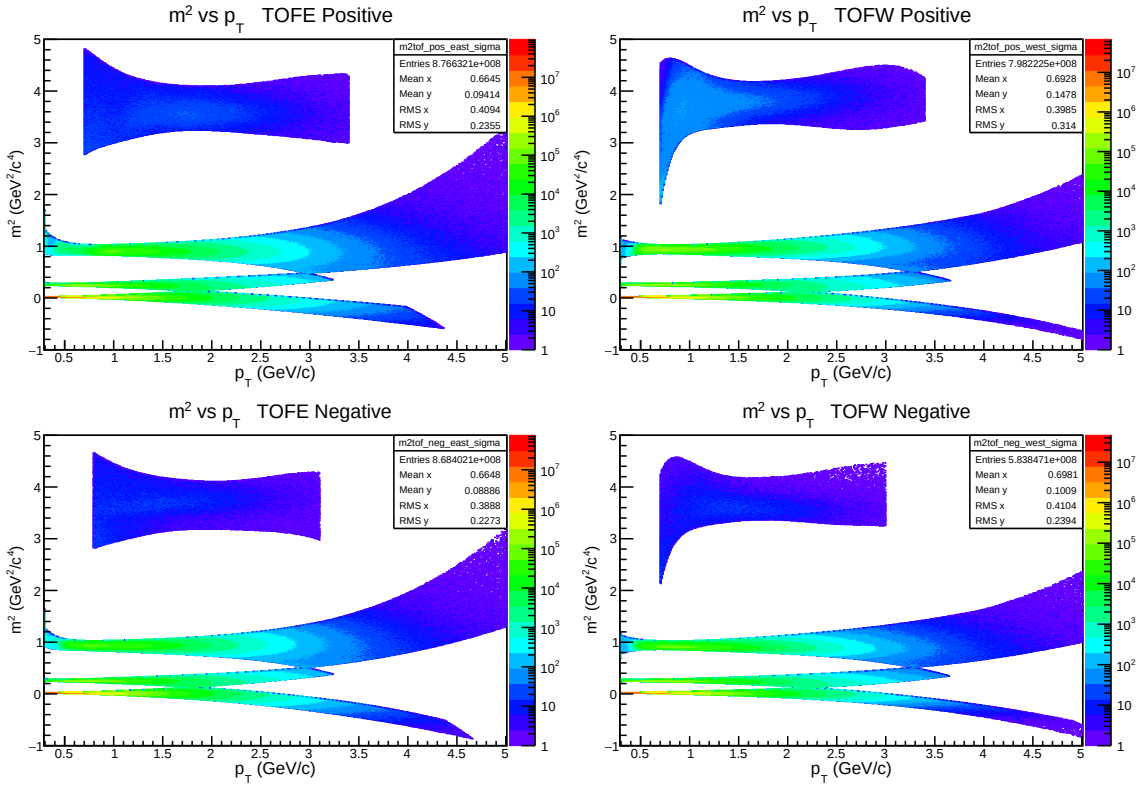

Figure 4.20: The mass-squared vs p_T plots of positive (above) and negative (below), East (left) and West (right) tracks, similar to Fig. 4.13 with cuts included. Species are cut at two standard deviations from their mean and also with a 2-sigma veto from their adjacent species peaks.

4.5 The Event Plane Method

The flow of produced particles from heavy ion collisions in the azimuthal plane is characterized with respect to the physical orientation of the collision. There are different descriptions of the collision orientation commonly used. The *reaction plane* is the plane made by the line between the center of each nucleus together with the beam axis. Due to fluctuations in the initial conditions, the distribution of participating nucleons has an orientation that may be different from the reaction plane and may be reflected differently in the measured distribution of produced particles. The nucleons participating in the collision can therefore be described as having their own *participant plane* seen in the primed coordinates of Figure 4.21. While both the reaction plane and the participant plane refer to concrete physical pictures, they are both somewhat idealized in that neither is directly

attainable through observables. Instead the *event plane* is reconstructed from either spectators detected at forward rapidity or from produced particles [35]. Event plane measurements using spectator neutrons are expected to better approximate the reaction plane, and conversely - produced particles more closely related to the participant plane [36].

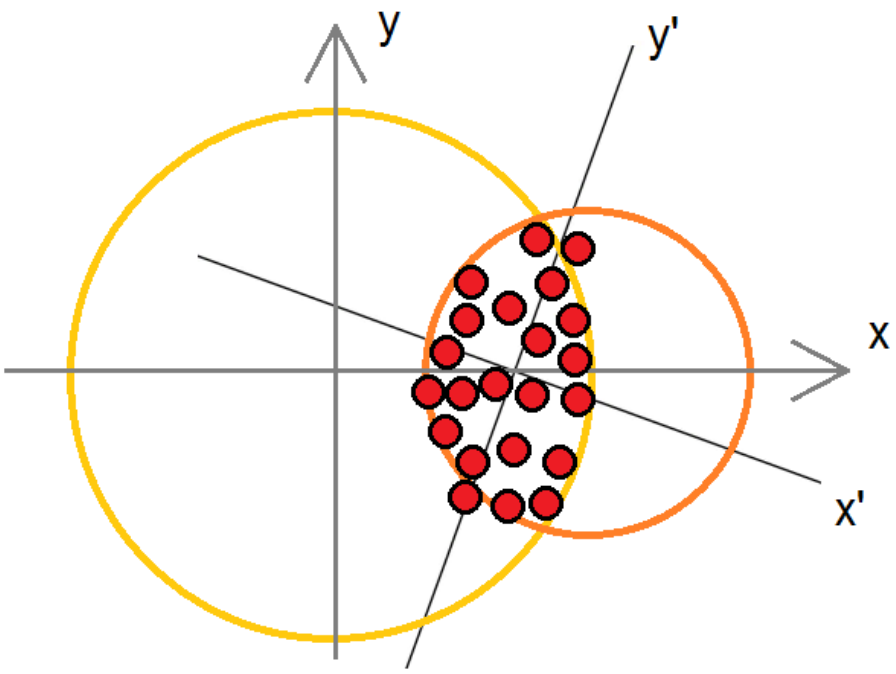

Figure 4.21: The reaction plane from a collision of two like nuclei is illustrated here and represented by the x and y axes. The red marks represent participating nucleons and the corresponding participant plane is that of x' and y' axes. The event plane in the context of this work, is the taken from measurements using either spectator neutrons or produced charged particles.

4.5.1 Q-Vector Recentering

The event plane vectors as measured by BBC and SMD detectors (Sec. 2.1) are calculated according to the weighted detector responses in the x and y axis directions called Q-*vectors*. This Q-vector has to undergo further calibrations to account for detector, or beam-condition effects. For example, the beam may not be aligned with the z-axis of the experiment, and therefore the exact middle of the SMD scintillator planes. The scintillators may yield light of varying relative intensity, which could bias the measured spectator

distribution. Additionally, a bias may arise in the BBC event plane measurement because it is used as a trigger for event selection (Sec. 2.1). A calibration used initially to correct for these imbalances involves recentering of the Q-vectors so that $<Q_x>$ and $<Q_y>$ are zero. The Q-vector recentering is done individually within each PHENIX run data to more closely account for changes in the detector during the period of operation.

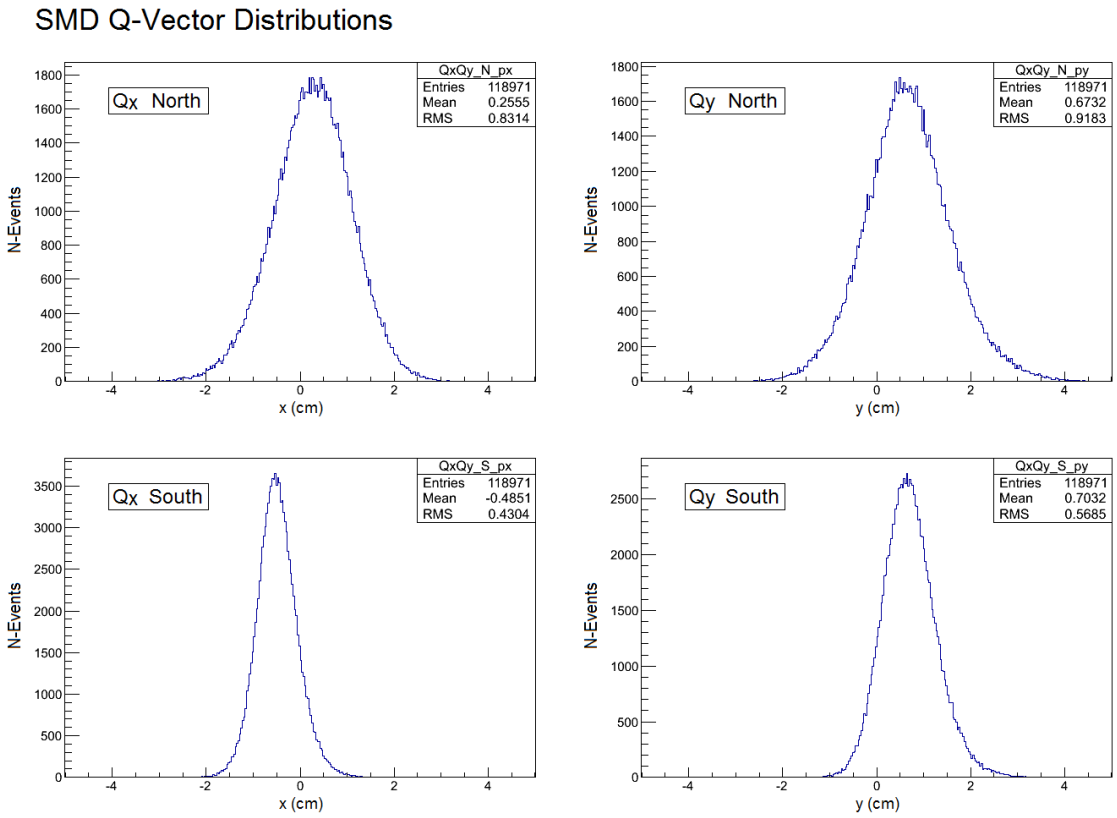

Figure 4.22: Raw Q-vectors for North and South Shower Maximum Detectors (top and bottom panels) and x and y planes (left and right panels).

The distribution of both Q_x and Q_y vectors in the North SMD are broader than those in South (Fig. 4.22). The North side is where copper spectator neutrons are incident and impact with less overall mass on average than the neutrons in the gold-going direction on the South side. The resulting PMT signals in the North are predictably weaker than the corresponding PMTs in the South (Fig. 4.23).

Although the method used in this work for recentering is the standard one [37, 38, 39, 40, 41, 42, 43], a possible refinement was discovered after submission for publication that

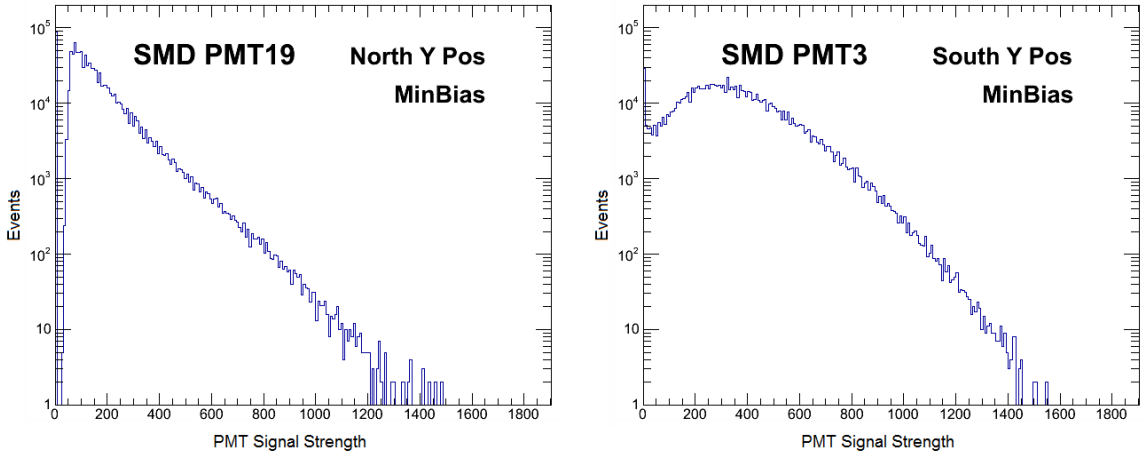

Figure 4.23: Distributions of the charge measured in single events PMTs in the North (left) and South (right). Each SMD has 15 scintillators, and the two examples above are from corresponding horizontal scintillators in the North and South. On average, the South PMTs measure more charge due to the greater incident mass of spectator neutrons from the gold nuclei compared to the South going copper neutrons.

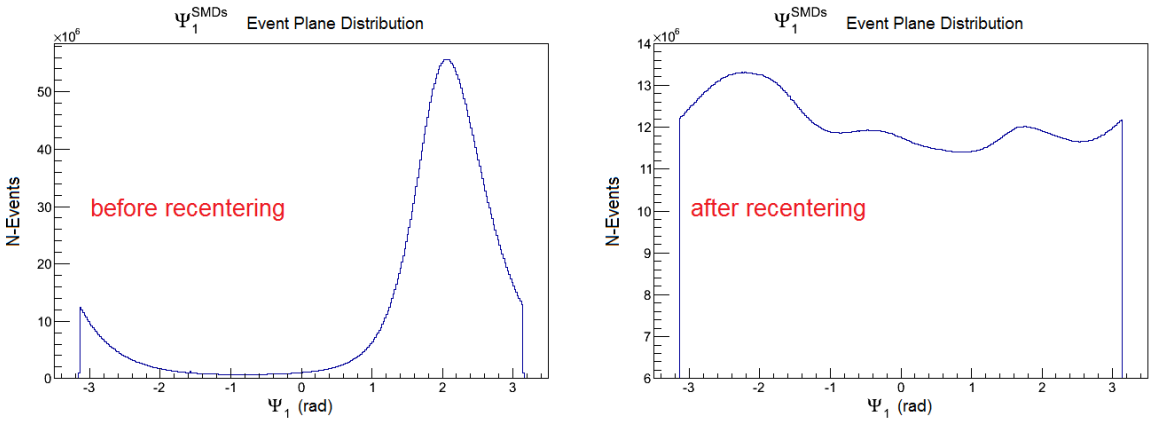

Figure 4.24: The Q-vectors are combined to form an event plane angle ($\Psi = arctan(\frac{y}{x})$) before (left) and after recentering (right). The example above is from SMD-South and the subscript "1" refers to its use in measuring the coefficient of directed flow v_1.

is proposed for the first time here. Instead of shifting Q-vectors such that the mean is zero, an alternative is to shift to the *median* or middle value. Because in principal all reaction plane angles are equally probably, an idealized detector will for instance measure equal numbers of Q-vectors with positive x values as negative. If the distributions of Q-vectors were symmetric, the mean and middle values would be the same, however from visual inspection (Fig. 4.22) all of the distributions are skewed.

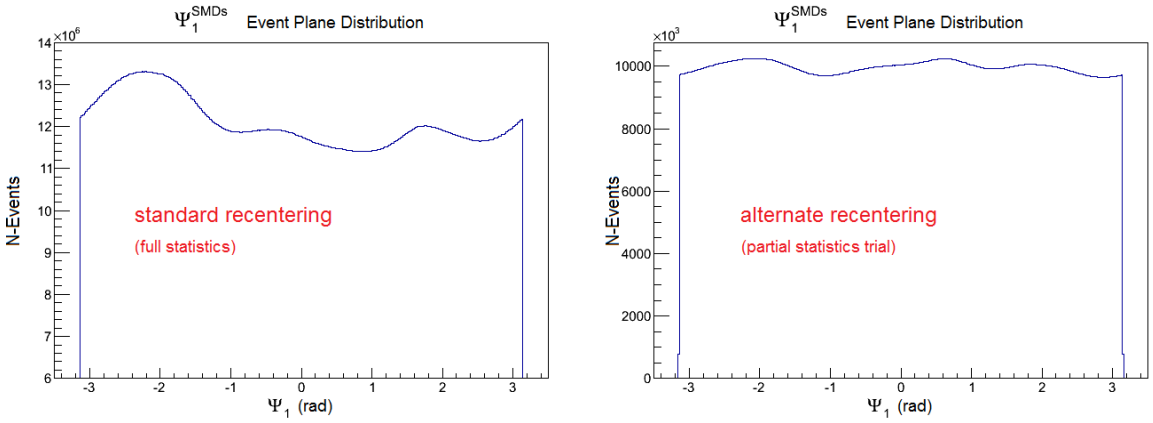

Figure 4.25: A recentering based on using *mean* (left) vs *median* (right), the latter provides a more uniform distribution of event planes. The former is the standard method and is used in this analysis.

4.5.2 Fourier Series Flattening

A second procedure to correct for forward event plane detector imperfections is flattening with a Fourier series [44]. The distribution is approximated by a Fourier series expansion, in this case - one with twenty terms. Subsequently each event-plane angle is shifted using the series expansion according to Eq. 4.10. Similarly to the recentering procedure (Sec. 4.5.1), flattening is done individually within each PHENIX run.

$$A_m = \int_{-\pi}^{\pi} cos(m\Psi)\, d\Psi \;\; = \;\; -\frac{2}{m} < sin(m\Psi) > \tag{4.8}$$

$$B_m = \int_{-\pi}^{\pi} sin(m\Psi)\, d\Psi \;\; = \;\; \frac{2}{m} < cos(m\Psi) > \tag{4.9}$$

$$\Psi' = \Psi + \sum_m (A_m \cos m\Psi + B_m \sin m\Psi) \tag{4.10}$$

In Equation 4.10, Ψ is the event plane angle after recentering (Sec. 4.5.1), Ψ' is the event plane angle shifted in such a way that the accumulated distribution will be flat, m is the Fourier term order (from 1 to 20 in this work), and A_m and B_m are Fourier coefficients found with Equations 4.8, and 4.9. Recentering and flattening is done separately for 6 different z-vertex position intervals due to varying angles of spectator neutrons (produced charged particles) incident in the SMD-South (BBC-South) measuring the event plane. Similarly, different collision centrality intervals also produce varying intensities of forward particles. Recentering and flattening are likewise done separately for 10 centrality intervals.

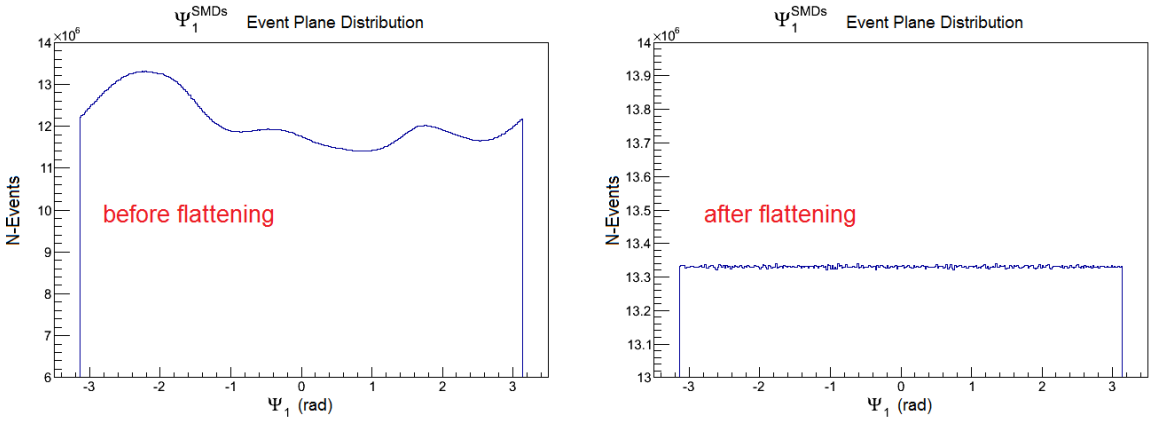

Figure 4.26: A flattening procedure is used to correct for the irregularities in event plane angle measurements.

4.5.3 Event Plane Resolution

Event plane measurements using either spectator neutrons or produced charged particles are both limited in resolution due to the finite multiplicity of incident particles. If detector imperfections and nuclear fluctuations are neglected, the SMD-North detector is ideally expected to measure an event plane angle 180° from that of SMD-South. This is because on average, the spectator neutrons of the copper and gold have oppositely oriented

centroids. Their correlation is seen in Figure 4.27 with the SMD-North rotated 180°. Better resolution in each detector would yield a tighter band on the diagonal.

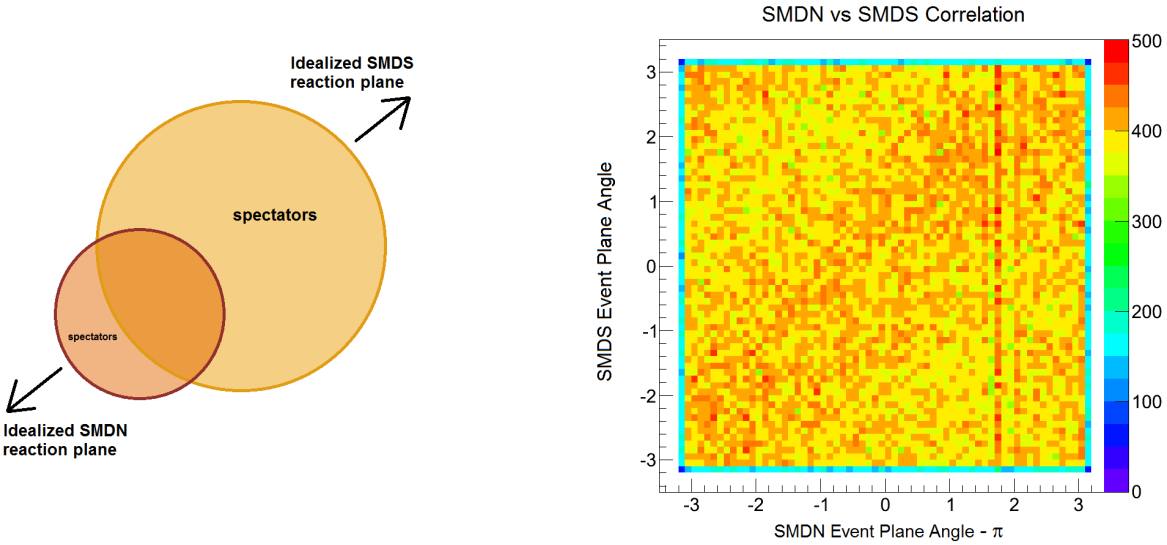

Figure 4.27: The illustration (left) shows the opposite angles of event plane measured by spectator neutrons moving in opposite directions along the z-axis of the beamline. The 3-D histogram (right) shows the correlation of North and South measurements with the SMD-North event plane angle rotated 180° to approximately align with the SMD-South event plane. Weak correlation is seen between event plane angles measured by SMD-South and SMD-North due in large part to the low resolution in each. Fluctuations in both nuclei also enlarges the difference between North and South measurements. The vertical band around 1.75 rad on the x-axis reveals an irregularity in SMD-North.

As uncertainty in the event plane measurement increases, the magnitude of anisotropic flow measured will necessarily decrease. A technique exists for compensating for this effect that involves comparing the event planes measured by multiple independent detectors. The resolution of the detector used to measure the event plane is then used to correct the measurement of anisotropic flow using Eq. 4.11.

$$v_n = \frac{v_{n\ measured}}{Res(\Psi_n^A))} \tag{4.11}$$

The resolution of the event plane measurement is found with Eq. 4.12 in which Ψ_n^A is the event plane measured with detector A and Ψ_n^{RP} is the hypothetical reaction plane found with infinite granularity of measurement and an infinite number of detected particles.

$$Res(\Psi_n^A) = < cos(\Psi_n^A - \Psi_n^{RP}) > \tag{4.12}$$

$$Res(\Psi_n^A) = < cos(\Psi_n^A - \Psi_n^B) > \qquad two\ subevent\ method \tag{4.13}$$

$$Res(\Psi_n^A) = \sqrt{\frac{< cos(\Psi_n^A - \Psi_n^B) >< cos(\Psi_n^A - \Psi_n^C) >}{< cos(\Psi_n^B - \Psi_n^C) >}} \qquad three\ subevent\ method \tag{4.14}$$

The use of either the two or three subevent method in this work has depended on the availability of detectors to measure the event plane. Further, because Cu+Au is an asymmetric system only the three subevent method is applicable for measuring individual resolution of SMD-South, SMD-North, BBC-South, and BBC-North. The two subevent method is used for measurement of the second and third order event planes by combining the BBC-South and BBC-North into one common event plane measurement with the second detector being the central arm (CNT) [45, 40].

Chapter 5

Systematic Uncertainties in the v_n Measurements

5.1 Systematic Uncertainty Due to Event Plane Determination

In measuring the event plane angle Ψ_1 (for use in measuring v_1) only the SMD-South is suitable. The BBC-South uses produced charged particles whose azimuthal direction is linked to charged hadrons detected in the central arms by way of momentum conservation. This leaves only two possible combinations of three detectors that involve the SMD-South detector. The SMD-North is inadequate because it is in the Cu going direction and for very central events the entire Cu nucleus collides essentially inside the Au nucleus cross section. For more peripheral events the SMD-North has significantly fewer neutrons, which yield lower resolution. Figure 5.1 shows the distribution of energy from hadronic interactions deposited in the North and South. Lastly the SMD-North has issues with hot channels that alone make it a poor candidate. Figure 5.2 shows the recentered and flattened reaction planes from both SMD-North and SMD-South. The irregular peaks in the North (left panel) show the result of hot channels and the waviness is the response of the Fourier flattening procedure's result when attempting to correct for a distribution with a knot in it.

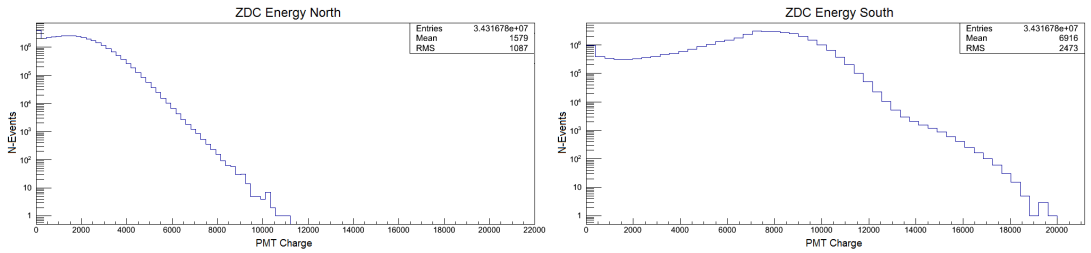

Figure 5.1: The ZDC North (left) measures significantly less energy from incident neutrons than the ZDC South (right). The North is the Cu-going direction and the South is Au-going. The event selection is minimum bias, and the number of events is plotted on the y-axis. The charges measured in all PMTs are added and plotted on the x-axis. The ZDC measurements featured here are for illustrative purposes as the ZDC is not used directly in event plane determination.

Only SMD-South is used for the event plane measurement, and SMD-North is used

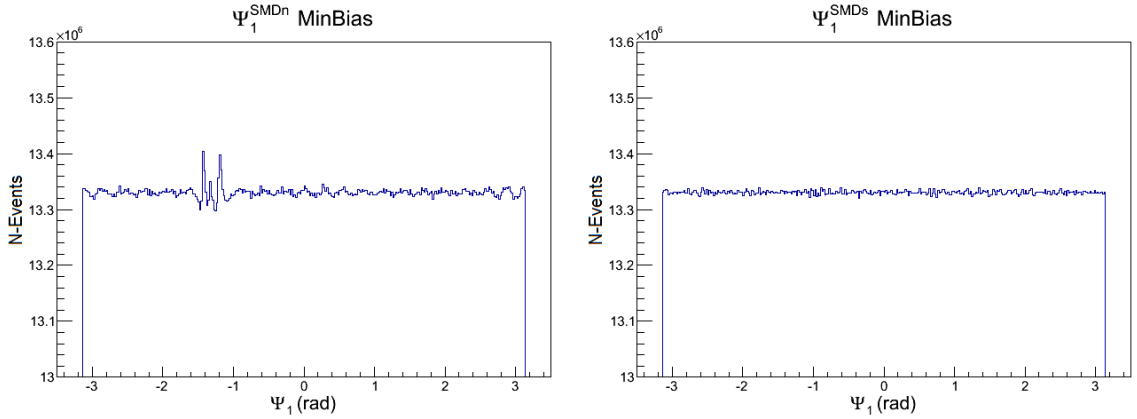

Figure 5.2: The left panel shows the recentered and flattened event plane distribution measured with the SMD-North which is the Cu going direction. The right panel is the corresponding distribution in SMD-South where Au spectator neutrons are incident. The irregular peaks in the North are due to hot channels.

for determining the event plane resolution in conjunction with the BBC-South. The difference found using SMD-North with BBC-North vs BBC-South to calculate the resolution (Eq. 4.14) is used to estimate the event-plane systematic uncertainty in the v_1 measurement. The leftmost panel of Figure 5.3 shows the alternate event-plane resolution results calculated separately in four centrality bins. This is found to be the largest source of systematic uncertainty in the v_1 measurements ranging from 20% for collisions in the 10-20% centrality bin and 12% in the 40-50% bin.

The systematic uncertainty associated with the use of the second and third order event planes in measuring v_2 and v_3 has involved more complicated steps than those used for v_1. The event plane is initially measured using a combination of BBC-North and BBC-South. The charged particles incident on the BBC-North are rotated 180° to coincide (approximately within the limits of measurement) with the angles of charges in the BBC-South, and the aggregate from both detectors is used. This combined BBC-North-South event plane measurement affords higher resolution than that from separate BBC-South (Fig. 5.3). The resolution of the combined BBC detector is found with the two subevent method (Eq. 4.13) with the additional use of the Central Arm event plane (CNT) . For this resolution, the particles used for evaluating the resolution are limited to only those with p_T between 0.2

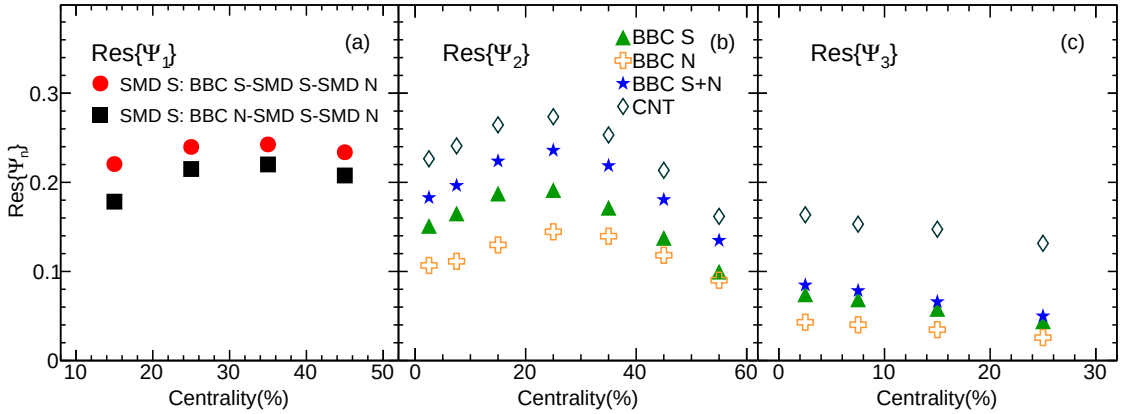

Figure 5.3: Panel (a) shows the event plane resolution as a function of centrality for the SMD-South detector used in the v_1 measurement. Panel (b) and (c) show the second and third order event plane resolution. The BBC event plane resolution is obtained from two sub-events and BBC-South, BBC-North, CNT from three sub-events as a function of centrality.

and 2.0 GeV/c in order to minimize the influence of jets. The resolution of BBC-North and BBC-South are measured individually using the three subevent method with the alternate BBC and CNT detectors, and then resulting v_2 and v_3 differences are respectively used as the systematic uncertainty for the combined BBC detector. The resulting uncertainty is found to be between 3% and 4% for v_2, and between 3% and 7% for v_3.

5.2 Systematic Uncertainties from Background Particles

The systematic uncertainty associated with the influence of background tracks on the measured v_n values is studied by varying track matching cuts (Sec. 4.3), which are used to reduce the background. For a preliminary test, the PC3 matching cut is removed and the resulting flow measurements found to be less than 50% of the original because of the increased influence of the background. To use the PC3 matching requirement to measure the systematic uncertainty associated with the background, the cut is varied between 2.0 and 2.5 σ and the difference in Fourier coefficients from measurements of anisotropic flow are again compared. A similar test is performed in which the PC3 matching cut is held at 2.0 σ and the EMCal cut is turned on or off. The resulting changes in v_n measurements are

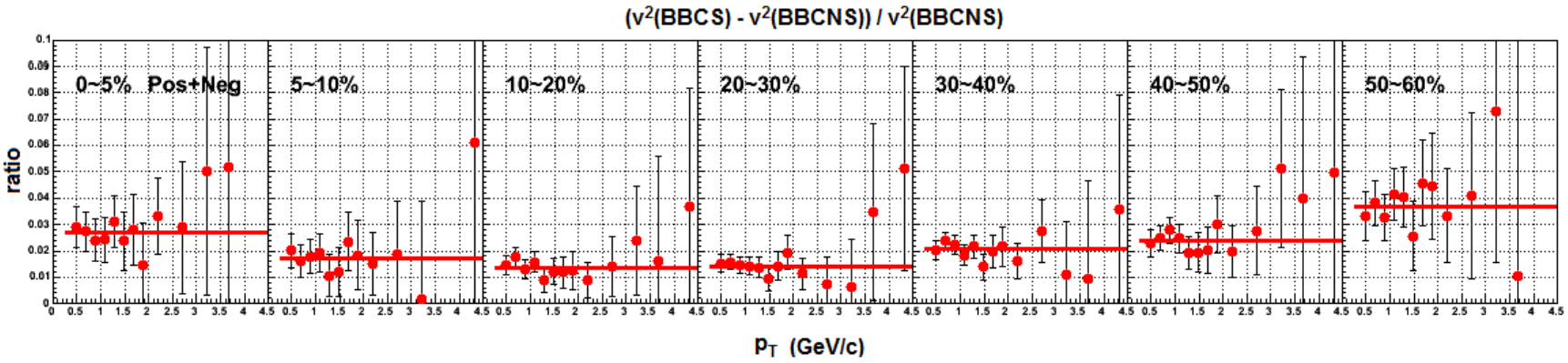

Figure 5.4: (Plot made by Hiroshi Nakagomi) Systematic uncertainty in the second harmonic event plane measurement is found through comparison of results obtained using different detector combinations. BBC-North and BBC-South are combined and compared to BBC-South.

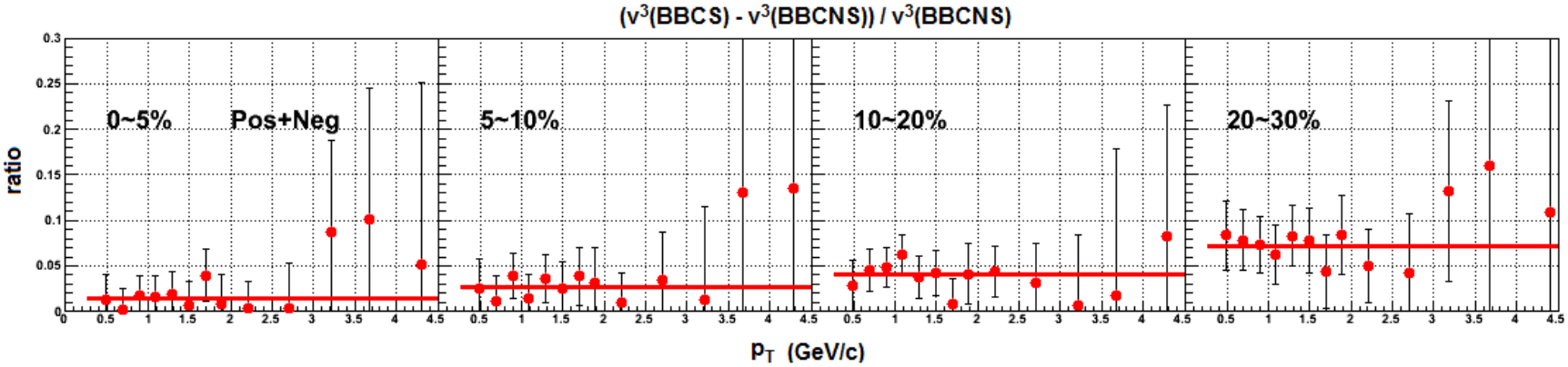

Figure 5.5: (Plot made by Hiroshi Nakagomi) Systematic uncertainty in the third harmonic event plane measurement is found through comparison of results obtained using different detector combinations. BBC-North and BBC-South are combined and compared to BBC-South.

shown in Figures 5.6, 5.7, 5.8. Both tests are found to yield differences on average of less than an absolute difference of 5×10^{-4} for v_1 and less than 2% for v_2 and v_3.

5.3 Systematic Uncertainties Due to Limited Detector Acceptance

A number of studies have been performed to examine the influence that detector acceptance may have on the anisotropic flow measurements. A toy model used to produce a flat reaction plane distribution together with an anisotropic track distribution mimicking measurements has been mated to the same analysis procedure used with real data. The simulation approximates the acceptance of the PHENIX central arm as well as individual subsystems to find out if the geometry is suitable to the type of flow measurements sought. With only statistical differences found between the generated distribution and those reproduced with full azimuthal acceptance, the PHENIX central arm acceptance, and the TOFW acceptance (Fig. 5.9), this test did not yield any results that negate the detector setup used.

An important distinction between the toy model and a full detector simulation (such as GEANT, GEometry ANd Tracking) is that detector inefficiencies are unaccounted for in the former. The reaction plane angle in each toy model event is exactly known and not subject to the recentering and flattening procedures used to correct detector biases.

Comparisons are made between anisotropic flow measurements using only East or West arms of PHENIX in order to account for acceptance effects. Sizeable uncertainties are found, especially for the first and third harmonic. For v_1 the uncertainty has little centrality dependence, unlike v_2 and v_3, which have moderate centrality dependence. At low p_T the measured flow coefficients are very close to zero and the relative uncertainty has little meaning, especially for the first harmonic. For v_1 the uncertainty associated with the acceptance is within $3times10^{-3}$ absolute value. An average of the uncertainty percentages are taken over the whole p_T range for v_2 and v_3 to summarize the size of this uncertainty (Table 5.1), and the uncertainties are found to be within 3% for v_2, and 10% for v_3. Quantitatively, the uncertainty is propagated for each p_T bin of each centrality.

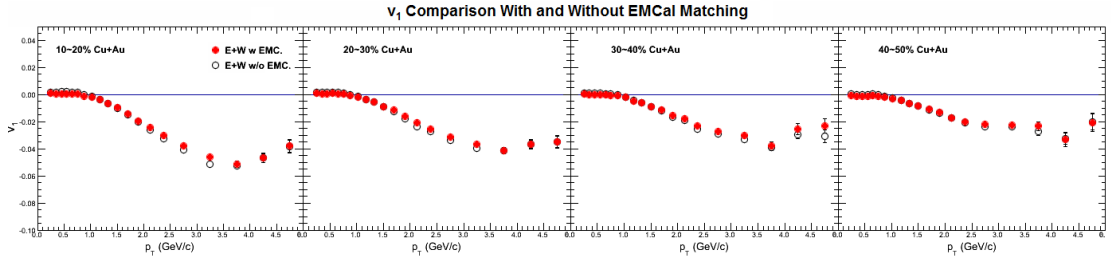

Figure 5.6: Comparisons are made of v_1 with and without EMCal matching track requirement to estimate the influence of background tracks.

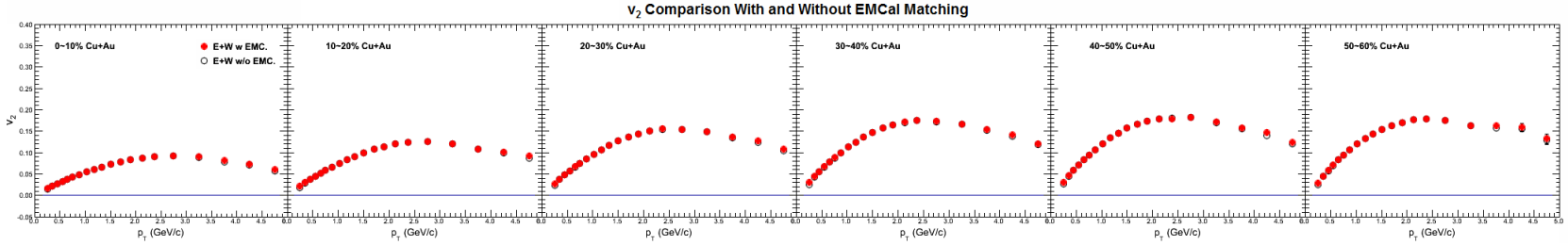

Figure 5.7: Comparisons are made of v_2 with and without EMCal matching track requirement to estimate the influence of background tracks.

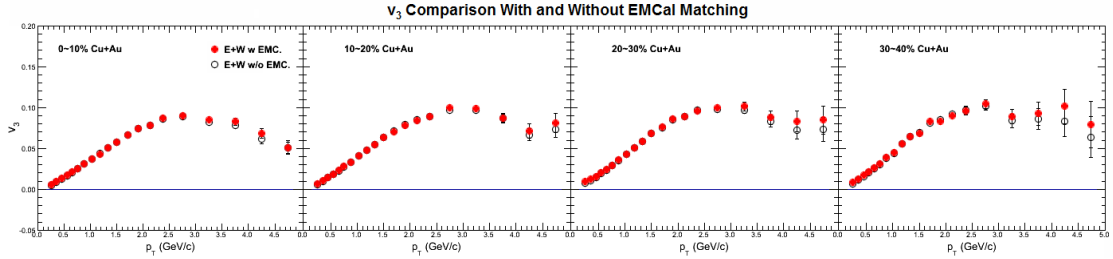

Figure 5.8: Comparisons are made of v_3 with and without EMCal matching track requirement to estimate the influence of background tracks.

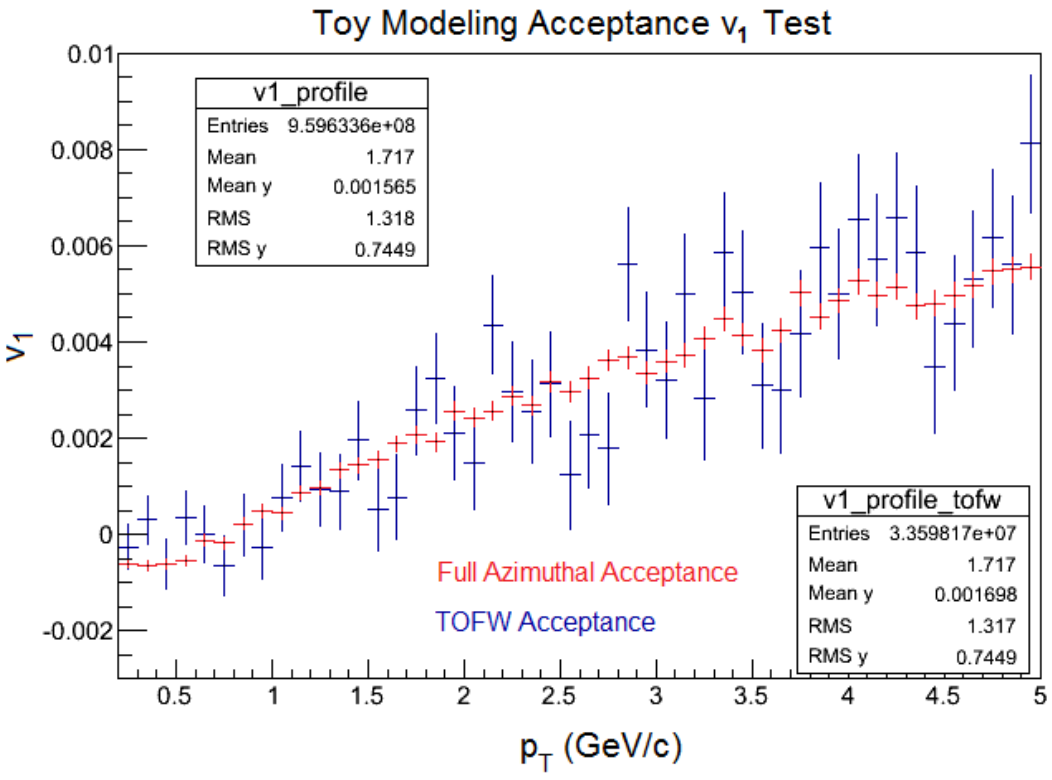

Figure 5.9: A toy model is used to test the viability of measuring anisotropic flow using limited azimuthal acceptance. In the plot above v_1 is measured using alternately the Time of Flight West detector acceptance (blue) and full azimuthal acceptance (red).

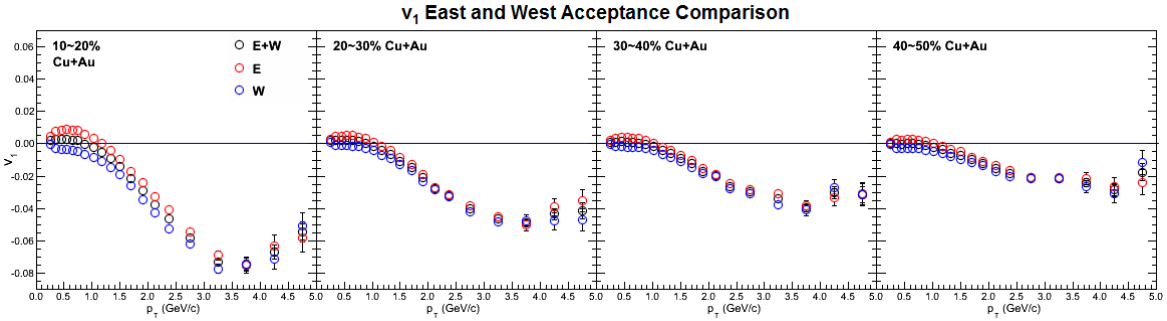

Figure 5.10: Measurements of v_1 are made separately for East (red), West (blue), and combined detectors (black). The difference between East and West results are taken as a systematic uncertainty.

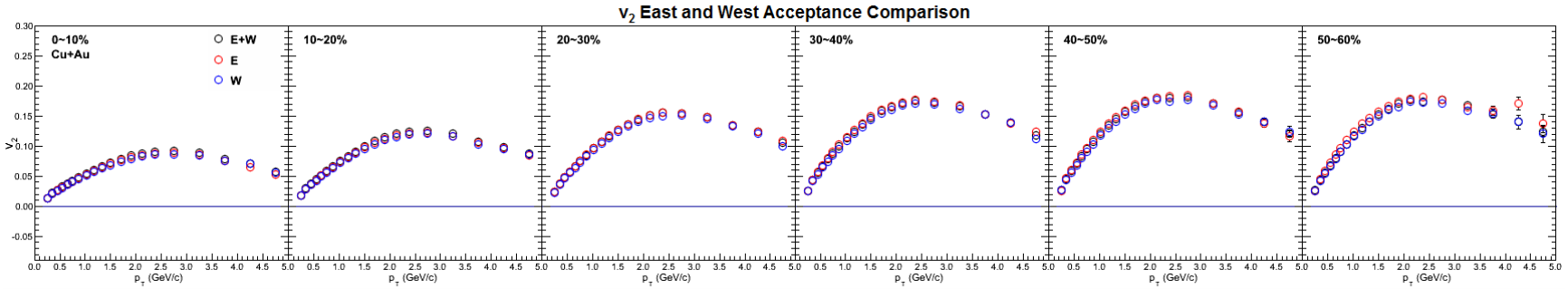

Figure 5.11: Measurements of v_2 are made separately for East (red), West (blue), and combined detectors (black). The difference between East and West results are taken as a systematic uncertainty.

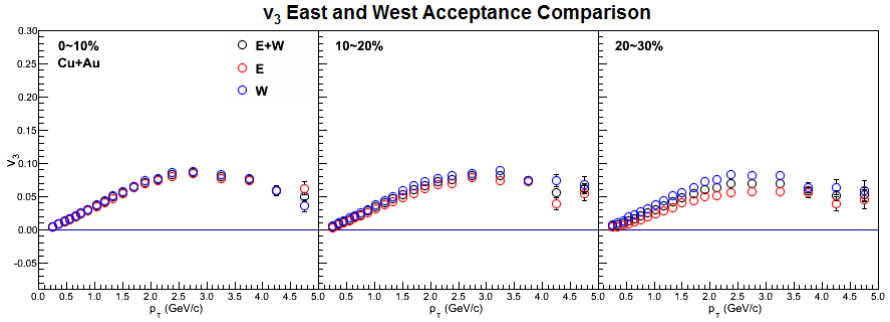

Figure 5.12: Measurements of v_3 are made separately for East (red), West (blue), and combined detectors (black). The difference between East and West results are taken as a systematic uncertainty.

5.4 Uncertainties Due to Particle Identification

Species purity is 95% as required by the two-standard-deviation cut and a two-standard-deviation veto below 2 GeV/c (Sec. 4.4.3). The systematic uncertainty due to the influence of species mixing is therefore maximally 5%. This estimate is significantly high because all of the measured species differ in their respective anisotropic flow coefficients by less than 50%. Below 2 GeV/c a common systematic uncertainty is therefore found to be 3%. Due to ambiguity in the fitting, a 5% systematic uncertainty is assigned to pions and protons for p_T greater than 2 GeV/c and is similarly 10% for kaons. In the case of v_1 the systematic uncertainty from particle identification is listed as absolute errors in order to be consistent with the presentation of other uncertainty factors in the directed flow measurement.

In order to be consistent with the presentation of other uncertainty contributions, the contribution from particle identification is listed as an absolute error for v_1 in the summary table (Sec. 5.5).

5.5 Summary of Systematic Uncertainties in the v_n Measurements

Table 5.1 shows different sources of systematic uncertainty for measurements of Fourier coefficients, featured in several figures in Sec. 6. All of the v_n measurements are plotted as a function of p_T, uncertainties can therefore be grouped according to the degree of correlated influence across the range of p_T. The three general types are:

- A uncorrelated uncertainties. Each data point will potentially shift independently.
- B some uncertainty correlation. Data points shift in the same direction in varying degrees.
- C uncertainties are correlated. Data points shift by a fixed increment.

Systematic uncertainties for v_1 measurements			
Uncertainty Sources	$10\% - 20\%$	$40\% - 50\%$	Type
Event plane	20%	12%	C
Background (absolute error)	5×10^{-4}	5×10^{-4}	A
Acceptance (absolute error)	3×10^{-3}	2×10^{-3}	C

Systematic uncertainties for v_2 measurements			
Uncertainty Sources	$0\% - 10\%$	$50\% - 60\%$	Type
Event plane	3%	4%	B
Background	2%	2%	A
Acceptance	2%	3%	C

Systematic uncertainties for v_3 measurements			
Uncertainty Sources	$0\% - 10\%$	$30\% - 40\%$	Type
Event plane	3%	7%	B
Background	2%	2%	A
Acceptance	8%	10%	C

Systematic uncertainties for particle identification in v_1 measurements			
species	$p_T \leq 2$GeV/c	$p_T \geq 2$GeV/c	Type
pion (absolute error)	1×10^{-3}	2×10^{-3}	A
kaon (absolute error)	1×10^{-3}	3×10^{-3}	A
proton (absolute error)	1×10^{-3}	3×10^{-3}	A

Systematic uncertainties for particle identification in v_2 and v_3 measurements			
species	$p_T \leq 2$GeV/c	$p_T \geq 2$GeV/c	Type
pion	3%	5%	A
kaon	3%	10%	A
proton	3%	5%	A

Table 5.1: Systematic uncertainties given in percent on the v_n measurements.

Chapter 6

Anisotropic Flow Results

6.1 Anisotropic Flow of Charged Hadrons

Measurements of the first, second, and third Fourier coefficients characterizing directed, elliptic, and triangular flow of the particles produced in heavy ion collisions are presented here. In each case, the absolute values of v_n increase as a function of p_T until between 2.5 to 3.0 GeV/c at which point they begin to decrease. This may reflect a change in particle production mechanisms, from recombination out of a thermal distribution of partons to a domain dominated by jet fragmentation.

6.1.1 Directed Flow

In an idealized system, the event planes measured using spectator neutrons will have opposite directions in the forward vs backward rapidities regions (Fig.4.27). In keeping with convention [46], the v_1 measurements that characterize directed flow are found with respect to the spectator nucleons in the projectile going direction. Further convention establishes the smaller nuclei species to be the projectile, and the larger nuclei to be the target. Because the target gold nuclei are used in this work to find the event plane (for reasons explained in Sec. 5.1), a sign-flip is introduced to restore consistency.

Figure 6.1 shows the first-order Fourier coefficient v_1 vs p_T for inclusive charged hadrons. Each sub-panel represents a 10% centrality interval beginning with more central on the left and increasingly peripheral toward the right. The most central interval is omitted because in these collisions the geometric anisotropies in the initial state are the smallest making the measurement systematics limited. In all centralities v_1 is negative for p_T above approximately 1 GeV/c. This signifies a greater abundance of particles moving away from the copper nucleus side of the azimuthal plane. The greater abundance of

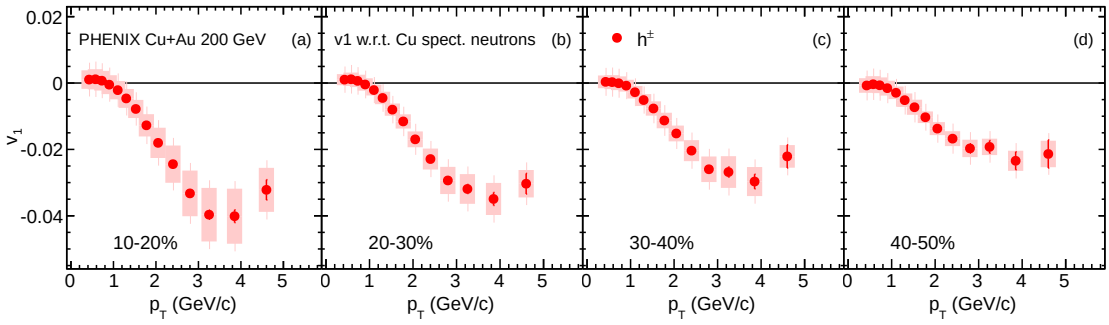

Figure 6.1: The Fourier coefficient v_1, which describes directed flow, is plotted as a function of p_T in four centrality intervals for inclusive charged hadrons measured at midrapidity in Cu+Au collisions at $\sqrt{s_{NN}}$ = 200 GeV. The left most panel is 10-20% centrality and to the right are increasingly more peripheral 10% intervals. The uncertainty bars show statistical uncertainties and the shaded boxes show systematic uncertainties.

low p_T particles would therefore be expected to offset this momentum imbalance with increased flow on the gold nucleus side. Results indicate this as seen by the positive v_1 below 1 GeV/c, however within the systematic uncertainty the low p_T result is also consistent with zero. Directed flow measurements in symmetric collision systems have similarly been observed to switch sides in the azimuthal plane at around 1 GeV/c, provided that forward and backward rapidity ranges are dealt with independently to prevent cancellation from the symmetry at midrapidity (an example is seen in Fig. 19 in the following reference) [13].

Two parameters commonly used [39, 47, 48, 49, 50] to examine the influence of collision geometry on particle production and flow are the number of participants (N_{part}) and the eccentricity (ε_n) defined in Equation 6.1 from reference [39]. The collision eccentricity is in some sense the degree of departure from a circular overlap region. For instance, ε_2 is the degree of ellipticity in the overlap region.

$$\varepsilon_n = \frac{\sqrt{\langle r^2 \cos(n\phi)\rangle^2 + \langle r^2 \sin(n\phi)\rangle^2}}{\langle r^2 \rangle} \tag{6.1}$$

To calculate N_{part} and ε_n a Glauber model Monte Carlo simulation with a Woods-Saxon

density distribution [51, 52, 53] is used that includes influences from nucleon fluctuations. Results for Au+Au, Cu+Cu, and Cu+Au at the same energy are shown in Table 6.1 at the end of this chapter. All N_{part} and ε_n values used herein were contributed by Dr. Jeffery Mitchell.

Unlike the measurements of elliptic and triangular flow coefficients (v_2 and v_3, shown in Fig. 6.4, and 6.7 respectively), the absolute value of v_1 in the intermediate and high p_T regions decreases starting from central to more peripheral collisions. This coincides with a smaller number of participants giving rise to diminished directed flow, while over the same course greater elliptic and triangular flow are measured for reasons discussed below.

Directed flow also differs from the second and third order harmonics in its variance with eccentricity. As the absolute value of v_1 decreases from central to peripheral, ε_1 increases. It is found empirically that v_1 varies approximately with $1/N_{part}^{2/3}$ as seen in Figure 6.2. No scaling relation with ε has been found. As this work constitutes the first measurement of directed flow from the PHENIX collaboration, there are no other available systems for direct comparison using this scaling.

The dissimilar relations of v_1 to N_{part} and ε_n may suggest the origin of directed flow at midrapidity is different from that of elliptic and triangular flow. In all centrality and p_T intervals the magnitude of v_1 is significantly smaller than that of v_2 and v_3 and the underlying cause of directed flow may have similarly small influence on the bulk system.

While no immediately obvious physical interpretation for the $1/N_{part}^{2/3}$ scaling factor presents itself, it may pertain generically to the transverse area of overlap between the two nuclei, if N_{part} is taken to be approximately representative of the initial volume of the system. This conjecture can only be weakly suggested here as the systematic uncertainties (Fig. 6.1) are of similar sizes to the variations in scaled v_1, and it is unclear whether the sources of systematic uncertainty would bias the measurements of central and peripheral centrality intervals identically.

The result of a second empirical attempt at scaling v_1 in different centrality intervals

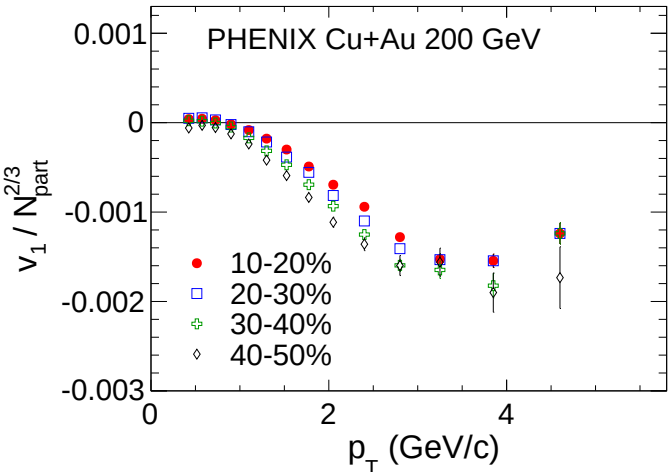

Figure 6.2: The Fourier coefficient v_1 is scaled with $1/N_{part}^{2/3}$ for four centrality intervals of Cu+Au collisions at $\sqrt{s_{NN}} = 200$ GeV. Numerical uncertainty is plotted with bars and systematic uncertainty is omitted. Approximate agreement is seen from low to high p_T.

using $1/\sqrt{N_{part}}$ is shown in Fig. 6.3.

6.1.2 Elliptic Flow

Measurements of the second harmonic coefficient v_2, which is representative of the elliptic flow in charged hadrons produced in Cu+Au collisions at $\sqrt{s_{NN}}$ = 200 GeV, are shown in Figure 6.4 as a function of p_T. Six centrality intervals are plotted in 10% increments beginning with the most central. Values of the second Fourier coefficient v_2 increase as collisions range from most central to mid-central around 30-40% and then either level off or slightly increase in 40-50% with the ambiguity arising from systematic uncertainty. Over the whole p_T range v_2 is consistently higher than v_1 and v_3 (Fig. 6.1, 6.7). Also in Figure 6.4 are v_2 values for the Cu+Cu and Au+Au systems at the same energy. The Cu+Au values (red) fall very consistently between that of the smaller Cu+Cu (green) and larger Au+Au (blue) values from [54].

With the exception of the first centrality interval, v_2 is ordered by system size. Comparing the three systems according to their respective centrality intervals is somewhat arbitrary in that the centrality event selection lacks a unifying physical observable to compare with.

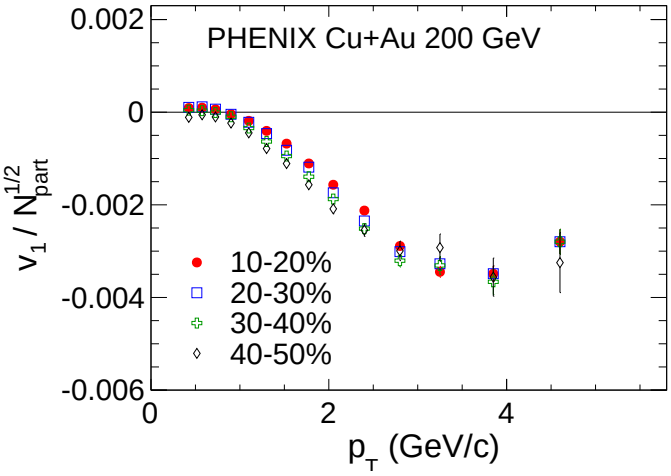

Figure 6.3: The Fourier coefficient v_1 is scaled with $1/N_{part}^{1/2}$ for four centrality intervals of Cu+Au collisions at $\sqrt{s_{NN}} = 200$ GeV. Numerical uncertainty is plotted with bars and systematic uncertainty is omitted. Approximate agreement is seen from low to high p_T.

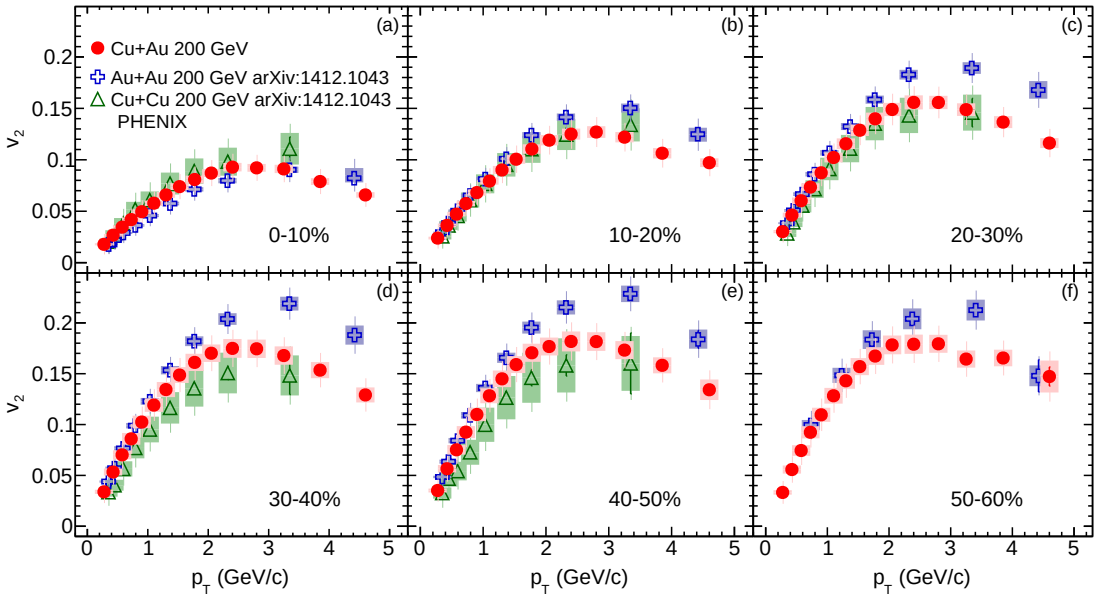

Figure 6.4: The second-order Fourier coefficients v_2 which is a measurement of elliptic flow, is plotted as a function of p_T. Cu+Cu data points [54] plotted in green, Cu+Au is in red, and Au+Au [54] is blue. Statistical uncertainty is plotted with bars and systematic uncertainty with shaded boxes. The top left panel shows the 0-10% centrality interval and subsequent panels show increasingly peripheral collisions in 10% intervals.

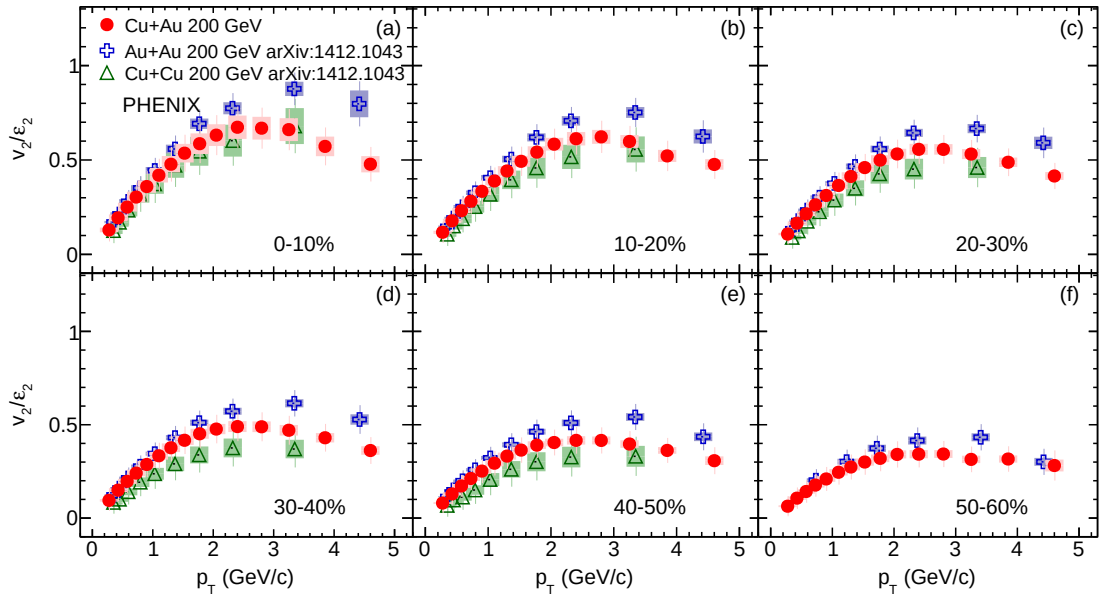

Figure 6.5: An identical presentation is used as in Figure 6.4 with the addition of scaling by ε_2. System sizes are consistently ordered for all centralities from smallest up to largest. The second-order harmonic scaled with eccentricity is seen to decrease from central to peripheral collisions. Eccentricity is calculated with Monte Carlo Glauber simulation.

In this scheme each species centrality is selected only in comparison to other collisions with the same species. Elliptic flow is understood to arise in large part from the influence of the collision geometry giving rise to a lenticular overlap region [47]. Scaling is introduced for v_2 of the three systems based on the elliptic eccentricity (ε_2) estimated from Glauber Monte Carlo simulations. The results are shown in Table 6.1 at the end of this chapter. For the second harmonic, the most central collisions have the lowest elliptic eccentricity and subsequently more peripheral collisions have correspondingly greater eccentricity. The results of v_2 scaled with ε_2 are shown in Figure 6.5.

With eccentricity scaling v_2 in Cu+Au remains consistently positioned between the smaller Cu+Cu system and larger Au+Au system. The species order is also flipped for the first centrality interval as seen in the top left panel of Figure 6.4 in relation to the unscaled resulted shown in Figure 6.5. Scaling with ε_2 has the additional effect of yielding coefficients that decrease in each centrality interval for all three systems as more peripheral

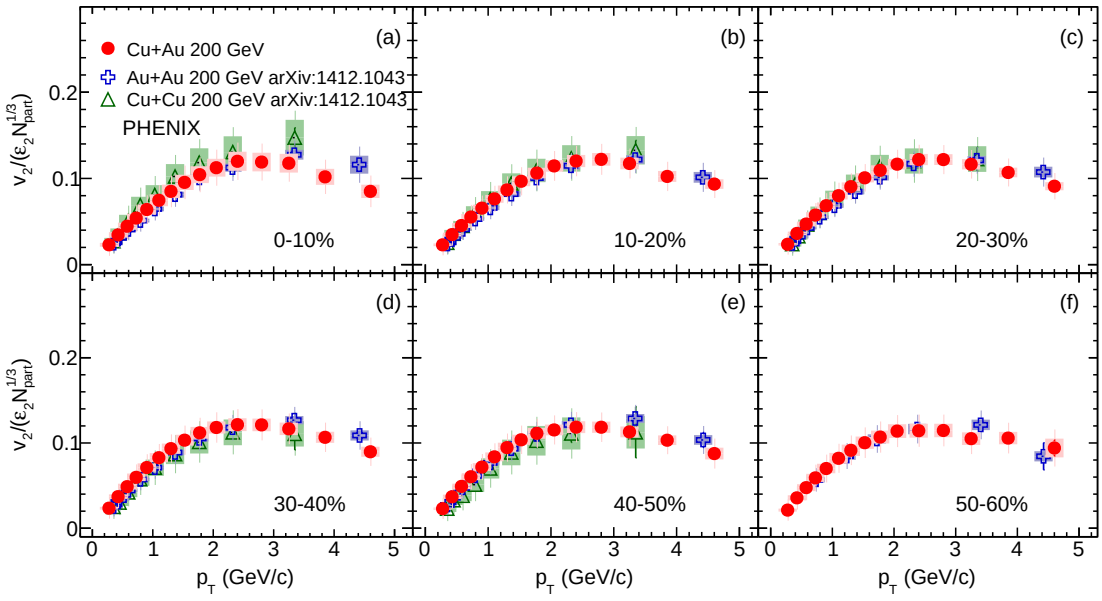

Figure 6.6: A presentation identical to Figures 6.4,6.5 is used. The second harmonic coefficient is scaled with eccentricity and N_{part}. Close agreement is seen for all three systems across a broad p_T range and in six centrality intervals.

collisions are selected.

This decrease in the eccentricity scaled second harmonic coefficients with centrality (Fig. 6.5) suggests elliptic flow is influenced substantially by the shape of the overlap region; however additional influence(s) are involved. A known scaling for Au+Au and Cu+Cu [39] is $1/(\varepsilon_n N_{part}^{1/3})$, in which $N_{part}^{1/3}$ is considered to be proportional to the 1-D length scale of the medium. Hanbury-Brown-Twiss measurements at RHIC have also demonstrated proportionality with $N_{part}^{1/3}$ [55]. The length of medium particles traverse will thereby influence the degree of collectivisation in flow.

6.1.3 Triangular Flow

The third order Fourier coefficient which is a measurement of triangular flow, is plotted in Figure 6.7 as a function of p_T for Cu+Au collisions at $\sqrt{s_{NN}}$ = 200 GeV. Three different centrality intervals are plotted beginning with 0-10% and concluding with 20-30%. Minimal v_3 increase is seen from most central to off-central collisions. This dependency

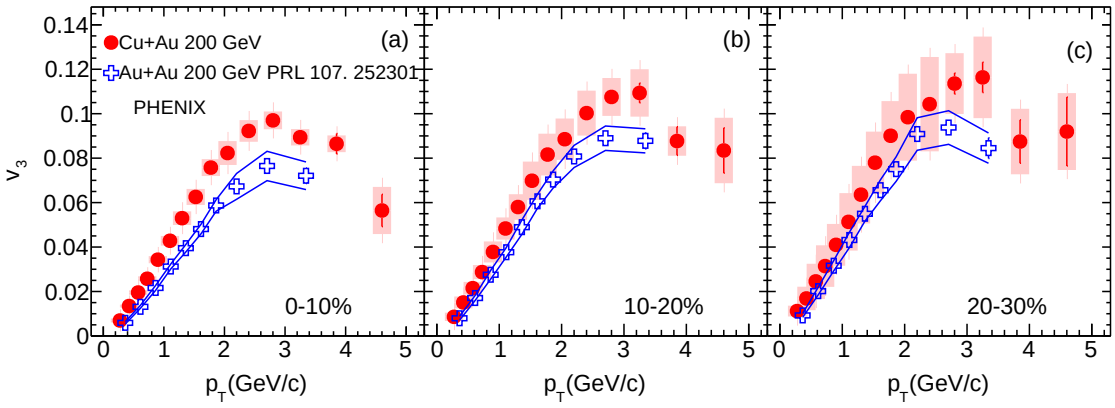

Figure 6.7: In each panel, the $v_3(p_T)$ coefficients are compared for the same centrality class, as marked in the figure. The symbols represent the measured $v_3(p_T)$ values, the uncertainty bars show the statistical uncertainties, and the shaded boxes indicate the systematic uncertainties for Cu+Au. The blue bounding lines show the systematic uncertainties for the Au+Au measurement. Cu+Au is represented with red data points and Au+Au with blue from [**?**].

is similar to that seen in measurements of triangular flow in Au+Au collisions at the same energy [56, 10, 57]. Within statistical uncertainty results are also consistent with no increase between centrality intervals. Also in Figure 6.7 are v_3 measurements of Au+Au at the same energy. For the three intervals available for comparison Cu+Au (red) is consistently greater in magnitude than Au+Au (blue). The third-order eccentricity ε_3 which is the degree to which participants are shaped in a trianglular arrangement, is consistently higher for Cu+Au than for Au+Au.

Table 6.1 at the end of this chapter shows ε_3 values for both systems. Eccentricity values are calculated from Equation 6.1 using Glauber Monte Carlo simulations that feature fluctuations. Preliminary (unpublished) comparisons have been made between simulations with and without fluctuations. Similar calculations that omit fluctuations show a resulting ε_3 comparatively minimal with only 5-10% of results that feature fluctuations. Consequently the triangular eccentricity may be largely the result of fluctuations even in the asymmetric Cu+Au system that has a degree of triangularity in the overlap region (illustrated in Fig. 6.8). The Cu+Au ε_3 values are between 25% and 50% greater than for Au+Au collisions. This can be interpreted as the fluctuations having greater influence in the smaller of

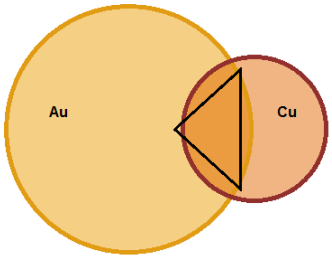

Figure 6.8: The overlap region of Cu+Au has inherent triangularity.

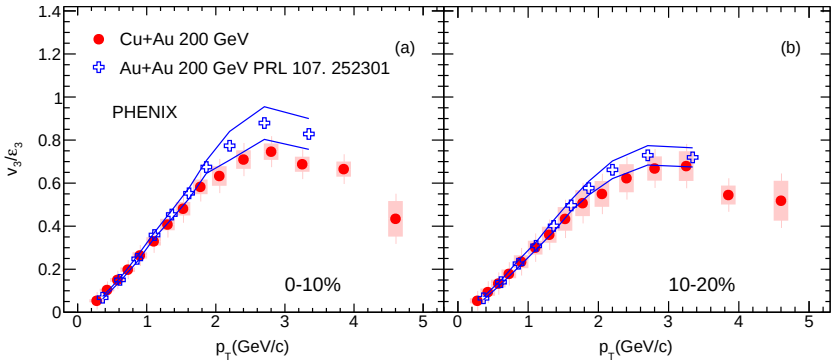

Figure 6.9: An identical presentation is used as in Figure 6.7 with the addition of scaling by ε_3. Very close agreement is seen for p_T below 2 GeV, above which Au+Au is either greater or consistent with Cu+Au within systematic uncertainties.

the two systems. By extension, Cu+Cu would then be expected to have an even larger ε_3 than Cu+Au; however there are no available ε_3 calculations for Cu+Cu from PHENIX.

The influence of eccentricity is investigated in Cu+Au collisions by scaling v_3 with ε_3 as is shown in Figure 6.9. The 20-30% centrality interval is omitted because the large systematic uncertainty of Cu+Au greatly obscures comparison. As was done in the analysis of v_2 (Sec. 6.1.2), scaling with ε_3 and $N_{part}^{1/3}$ is also shown in Figure 6.10. It is less clear in this case which of the two scalings best characterizes the measurement of triangular flow.

6.2 Anisotropic Flow of Identified Charged Hadrons

Figures 6.11, 6.12, and 6.13 show first, second, and third Fourier coefficients which are respectively measurements of directed, elliptic, and triangular flow of produced particles

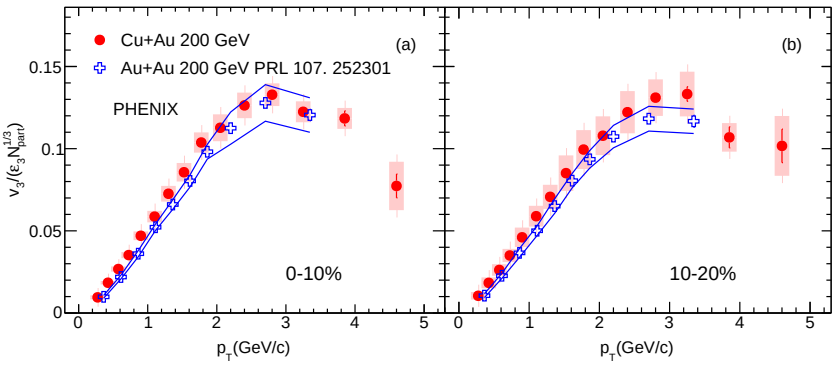

Figure 6.10: An identical presentation is used to Figure 6.7 with the addition of scaling by ε_3 and $N_{part}^{1/3}$. With this scaling Cu+Au and Au+Au v_3 are in agreement within systematic uncertainties across the whole p_T range.

from Cu+Au collisions at $\sqrt{s_{NN}}$ = 200 GeV. Statistical uncertainties are shown with bars and systematic uncertainties are shown with shaded boxes. The systematic uncertainties shown are only Type A (Sec. 5.5) as the correlated uncertainties are common to all three species. Each species is plotted with the positive and negative charges combined. Pions are plotted in red, kaons in blue, and protons (and anti-protons) in green. For v_1 and v_3 the centrality intervals are combined into a single 30% interval to reduce statistical uncertainty, with ranges 10-30% and 0-30% respectively. Centrality intervals are combined using a technique found in Reference [58].

The most central interval for v_1 is omitted because of the large systematic uncertainty. All three harmonics show mass ordering at intermediate p_T indicating more pronounced anisotropy for the lighter species. For v_1 systematic uncertainty prevents this conclusion from being definitive. All three species change directed flow direction from the copper side of the azimuth at low p_T, to the gold side at higher p_T. This crossing is also consistent with zero flow given the size of the systematic uncertainty. Mass ordering is a feature of hydrodynamic theory which points to a common velocity field. In the intermediate p_T region all three species show v_1 that is somewhat linear. Similarly to v_2 and v_3 the onset of this linear increase (negative for v_1) begins at higher p_T for larger masses. For p_T above 2

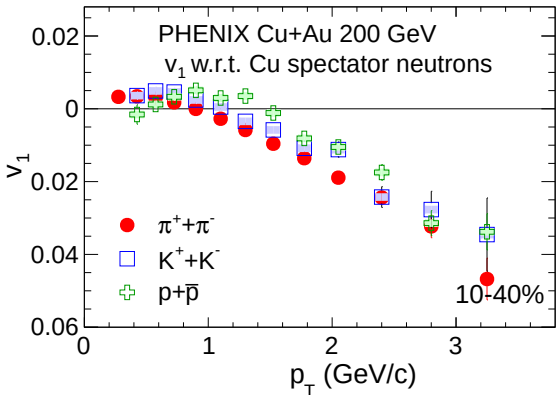

Figure 6.11: The first Fourier coefficient which is a measurement of directed flow is presented as a function of p_T in Cu+Au collisions at $\sqrt{s_{NN}} = 200$ GeV is shown for identified charge combined pions (red), kaons (blue), and protons (green). Collision centrality is merged for greater statistics into one interval of 10-40%. The most central collision interval is omitted because of high systematic uncertainty. Positive v_1 signifies flow in the copper side of the azimuthal plane. Statistical uncertainty is represented with bars and systematic uncertainty from particle identification is indicated with shaded boxes. The full systematic uncertainty is found in Table 5.1.

GeV/c the proton v_2 and v_3 departs from the ordering trend and are instead higher than that of pions and kaons.

The departure of proton v_2 and v_3 above pion and kaon is consistent with PID results from A+A [39, 56]. A consequence of the common velocity field predicted from hydrodynamics is that flow coefficients of the separated species differ when compared with respect to p_T. To account for this, p_T on the horizontal-axis is replaced with KE_T (Eqn. 6.2). Scaling related to species mass alone is inadequate, as demonstrated by measurements involving the ϕ meson, which has a mass similar to that of the proton although v_2 similar to π and K [59]. The number of valence quarks (n_q) per hadron is known to account for the differences in measurements of elliptic flow. Close agreement is seen for the second order coefficient when both the both v_2 on the vertical axis and KE_T on the horizontal axis are scaled with n_q. The influence of each of these steps is seen in Figure 6.14.

$$KE_T = m_T - m = \sqrt{p_T^2 + m^2} - m \tag{6.2}$$

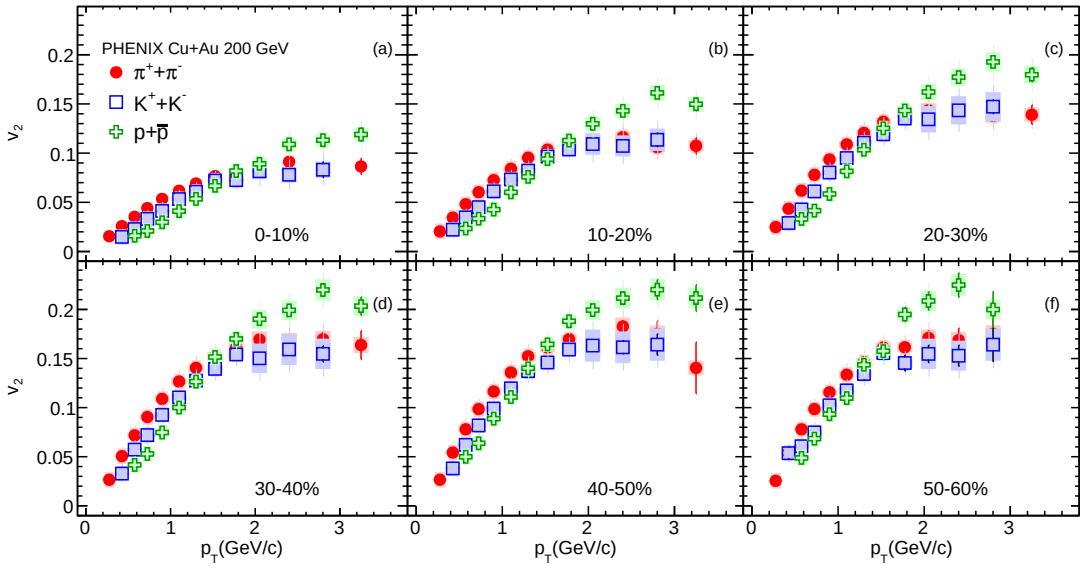

Figure 6.12: The second Fourier coefficient which is a measurement of elliptic flow is presented as a function of p_T in Cu+Au collisions at $\sqrt{s_{NN}}$ = 200 GeV is shown for identified charge combined pions (red), kaons (blue), and protons (green)). Six centrality classes are shown each having a 10% interval beginning with the most central 0-10% collisions in the upper left panel. Statistical uncertainty is represented with bars and systematic uncertainty from particle identification is indicated with shaded boxes. The full systematic uncertainty is found in Table 5.1.

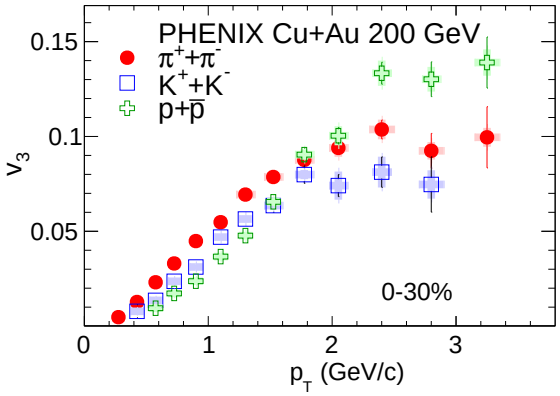

Figure 6.13: The third-order Fourier coefficient, which is a measurement of triangular flow is presented as a function of p_T in Cu+Au collisions at $\sqrt{s_{NN}}$ = 200 GeV is shown for identified charge combined pions (red), kaons (blue), and protons (green). Collision centrality is merged for greater statistics into one interval of 0-30%. More peripheral collision centralities are omitted because of systematic uncertainty. Statistical uncertainty is represented with bars and systematic uncertainty from particle identification is indicated with shaded boxes. The full systematic uncertainty is found in Table 5.1.

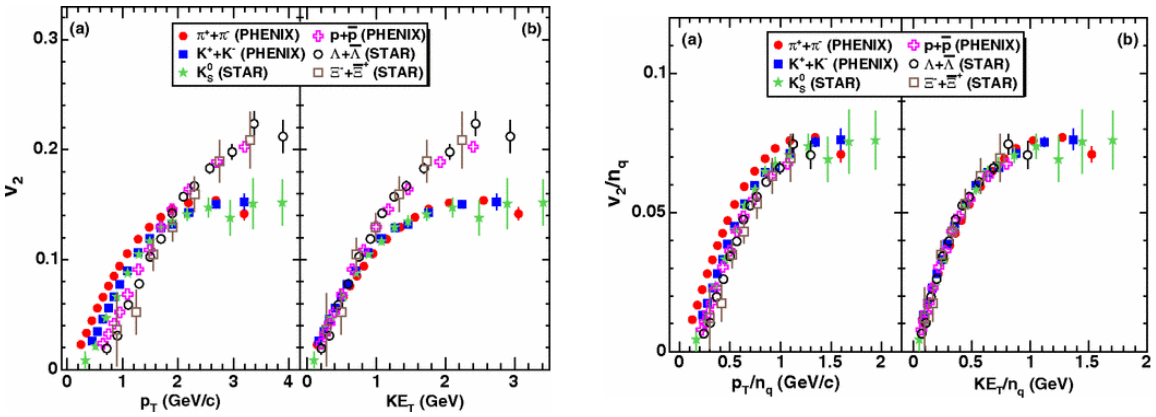

Figure 6.14: (Used with permission [54]) Measurements of the second Fourier coefficient for several hadron species produced in Au+Au collisions at $\sqrt{s_{\rm NN}} = 200$ GeV. Subpanels show steps implementing n_q scaling. The left most panel is unscaled $v_2(p_T)$, the middle left panel shows $v_2(KE_T)$, the middle right panel shows v_2 with both axis scaled by n_q, and the right most panel shows $v_2(KE_T$ with both axis scaled by n_q. For mesons n_q is 2, and for baryons 3.

Quark number scaling is explainable using models of coalescence/recombination from a phase-space densely populated with partons in thermal equilibrium progressing into a subsequent hadronization stage [60, 61, 62].

6.3 Comparisons with Theoretical Calculations

Heavy ion nuclear physics advances through measurements and comparisons with theoretical calculations. There are cases in which one principal fitting equation can be used analytically such as with *Blast Wave* modeling [63, 64, 65]. There are arguably more cases in which modeling will require intricate and extensive simulations, often Monte Carlo. The two types of comparisons with theory described in this section are the latter.

6.3.1 Hydrodynamics

Hydrodynamic modeling treats the state of matter (QGP) created in heavy ion collisions to be a nearly perfect fluid, describable with equations that stem from those in every academic text on thermal and statistical mechanics. The degree to which the QGP is describable as a perfect fluid is reflected by the very low viscosity over entropy (η/s), which

is a controllable parameter in hydrodynamics.

$$dE = TdS - PdV + \mu dN \tag{6.3}$$

Equation 6.3 is immediately recognizable as the first law of thermodynamics [66]. Following the derivation by Florkowski [67], if N is taken as baryon number then $dN = 0$. The remaining extensive variables E (energy), V (volume), S (entropy) are exchanged for ones that are intensive: ε (energy density) and s (entropy per baryon) using the relations in 6.4.

$$\varepsilon = \frac{E}{V}, \quad s = \frac{S}{N} \tag{6.4}$$

Additionally N is taken as the number of baryons n, yielding Equation 6.5.

$$d\varepsilon = \frac{\varepsilon + P}{n} + nTds \tag{6.5}$$

Next the entropy per baryon is considered to be a conserved quantity which yields adiabatic flow [67]. The resulting ideal hydrodynamic equation is commonly cited in the form of an energy-momentum tensor given in Eq. 6.6, where u^μ and u^ν are flow velocity vectors, and $g^{\mu\nu}$ is the metric tensor (alternate conventions are used for the sign of g^{00}). [68, 69, 70, 71, 67, 72, 73].

$$T^{\mu\nu} = (\varepsilon + P)u^\mu u^\nu - Pg^{\mu\nu} \qquad \partial_\mu T^{\mu\nu} = 0 \tag{6.6}$$

Event generators are used to simulate partonic distributions in varying degrees of ther-

mal equilibrium and with various energy density distributions. These are typically accompanied by assumptions of approximate cylindrical (in the case of 2D hydrodynamics) symmetry/boost-invariance. The remaining piece of theory necessary to guide a basic model of the medium's evolution is the equation of state, which relates pressure and energy density and can be obtained from lattice QCD computations. More sophisticated hydrodynamic models exist that are able to predict anisotropic flow measurements. In particular, calculations from the 3D+1 hydrodynamic model that includes the effects of viscosity in the medium are available for comparison to the v_1, v_2, and v_3 flow results described in previous sections of this chapter [69].

For v_1 only qualitative comparison is possible because of a different pseudorapidity range used in the hydrodynamic simulation. The crossover of the directed flow from the copper side of the azimuth for lower p_T particles to the gold side for higher p_T particles at around 1 GeV/c is consistent with predictions seen in Figure 6.15 [69]. Similar crossover is predicted by hydrodynamic theory in the case of symmetric systems [74] if independence in the forward and backward rapidities is considered in Section 6.1.1.

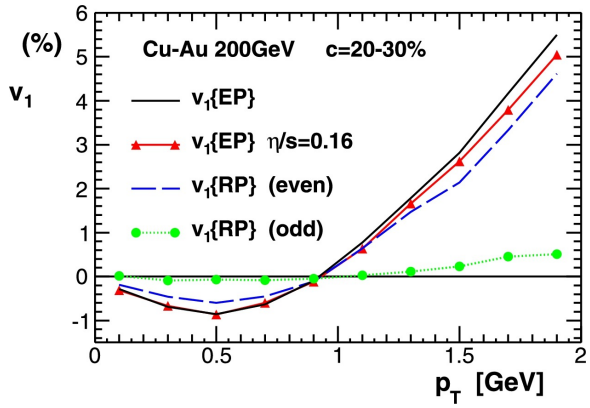

Figure 6.15: (Used with permission [75]) The first order coefficient v_1 which is a measurement of directed flow is plotted as a function of p_T. The results are with respect to the gold going spectators and are not sign-flipped like those in this work. With a different rapidity range covered these results are only qualitatively comparable. The black and red curves are otherwise the most directly comparable to the v_1 measurement in this work. The blue curve is a measurement designated *even* as it using both forward and backward spectator neutrons combined with even parity. The green curve is comparable to the blue except with *odd* parity. Below p_T of approximately 1 GeV/c the flow is on the copper size of the azimuth, and a crossover to the gold side is seen for high p_T to the gold side. This general behavior is consistent with measurements in this work.

Predictions for v_2 and v_3 for charged hadrons from the 3D+1 viscous hydrodynamic model are available for direct comparison with measurements. Figures 6.16 and 6.17 compare $v_2(p_T)$ and $v_3(p_T)$ respectively with calculations using η/s = 0.08 and 0.16. Comparisons are made for the most central 0-5% and also off central 20-30% intervals, in each case up to p_T of 2 GeV/c. For the most central interval the η/s = 0.08 matches more closely; however both values reproduce the data reasonably well.

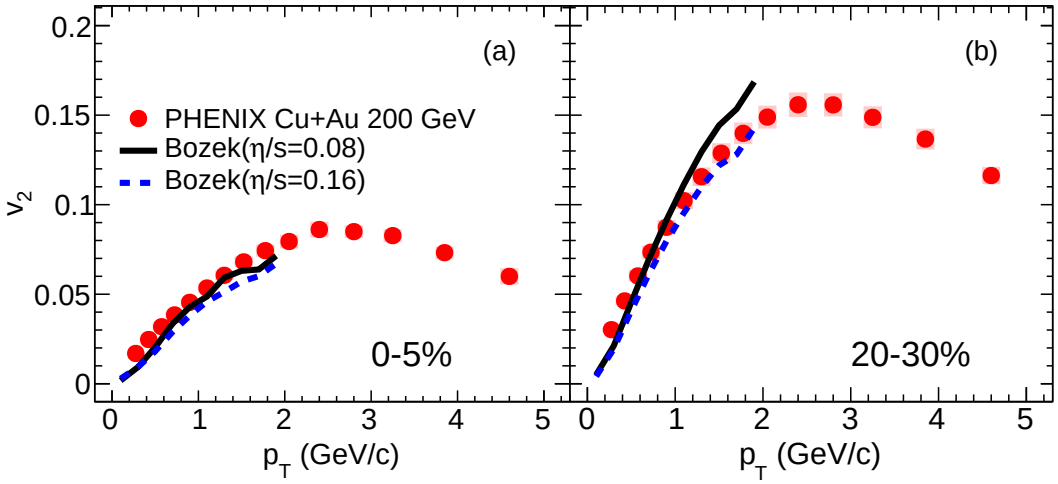

Figure 6.16: Calculations from 3D+1 viscous hydrodynamics are compared to measured values of the second Fourier coefficient $v_2(p_T)$ for unidentified charged hadrons at midrapidity in Cu+Au collisions at $\sqrt{s_{NN}}$ = 200 GeV. The left panel shows the most central 0-5% collision interval and the right shows 20-30%. Measurements from this work are plotted in red with bars representing statistical uncertainty and shaded boxes representing systematic uncertainty. Blue and black curves show the hydrodynamic calculations using η/s = 0.08 and 0.16 respectively.

6.3.2 A-Multiphase-Transport Model

Another tool for comparing experimental results with theory is the A-Multiphase-Transport-Model (AMPT) [76]. This model simulates heavy ion collisions from the early parton medium to hadron interactions before kinetic freeze-out. To do so a number, of other established models are combined including the HIJING [77, 78] (Heavy Ion Jet Interaction Generator) model of the initial conditions, the ZPC [79] (Zhang's parton cascade) model for partonic scattering using pQCD, the Lund string model for hadronization [76], and ART

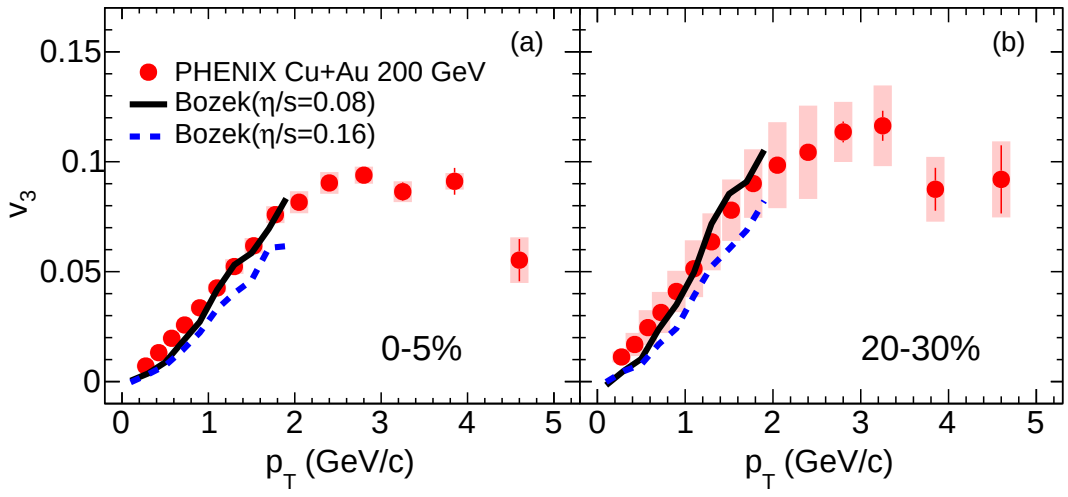

Figure 6.17: Calculations from 3D+1 viscous hydrodynamics are compared to measured values of the third Fourier coefficient $v_3(p_T)$ for unidentified charged hadrons at midrapidity in Cu+Au collisions at $\sqrt{s_{NN}}$ = 200 GeV. The left panel shows the most central 0-5% collision interval and the right shows 20-30%. Measurements from this work are plotted in red with bars representing statistical uncertainty and shaded boxes representing systematic uncertainty. Blue and black curves show the hydrodynamic calculations using η/s = 0.08 and 0.16 respectively.

[80] (A Relativistic Transport model) for hadron-hadron interactions.

A contributor to this work, and fellow member of the PHENIX Collaboration Javier Orjuela Koop has used AMPT v2.21 to simulate 2 million minimum bias Cu+Au events at $\sqrt{s_{NN}}$ = 200 GeV to calculate coefficients for comparison with measurements. Following the methods explained in Reference [81], calculations of $v_1(p_T)$ are made using alternatively fixed 42 mb nucleon cross sections referred to as *Black Disk* (BD) and *Grey Disk* (GD) that use varying cross sections. The first order Fourier coefficient is calculated with these alternate methods and shown in Figure 6.18.

As AMPT modeling does not include information on spectator neutrons following a collision, the event plane is used from the participants. The locations of participant nucleons are smeared with a Gaussian width of 0.4 fm. A second approach uses the impact parameter vector $\bar{b}$ as the event plane orientation. Results are necessarily only indirectly comparable to measurements using spectator neutrons for the event-plane determination. The top two panels in Figure 6.18 show the difference between the reaction plane from

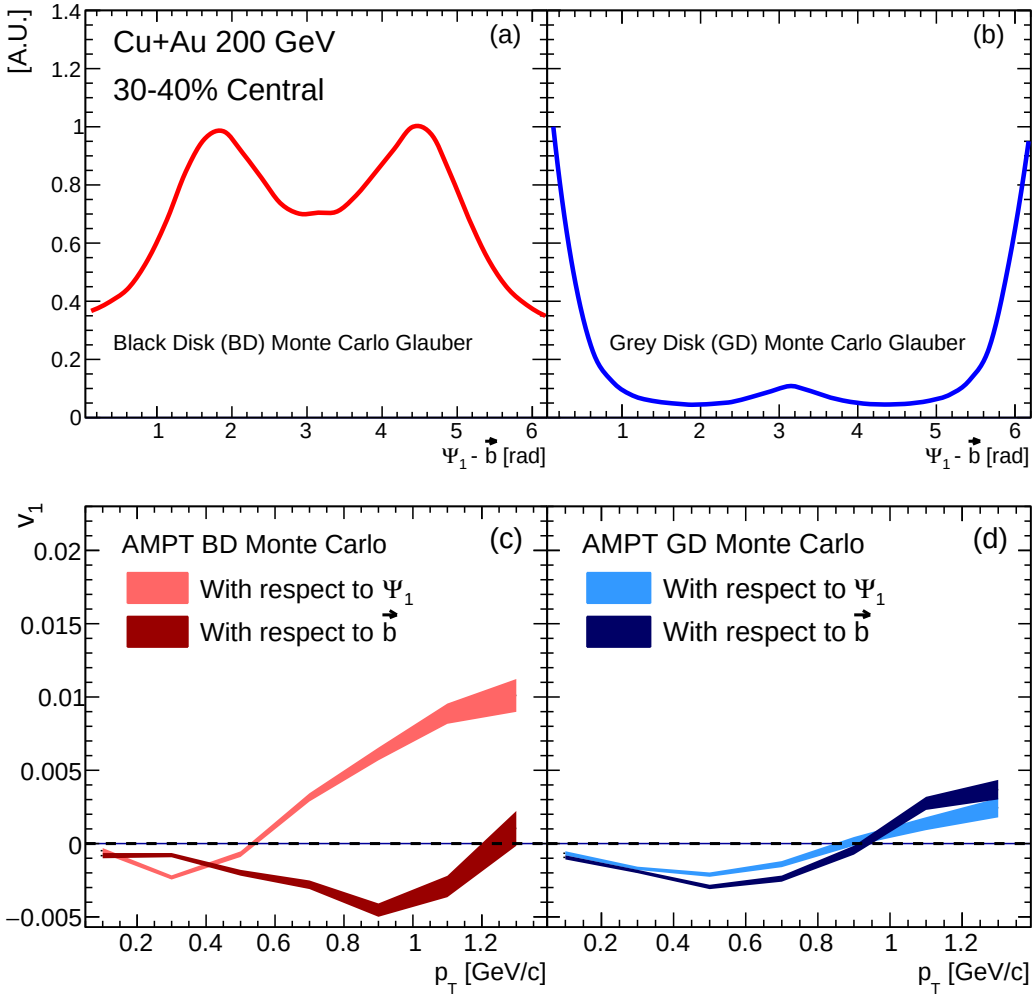

Figure 6.18: The bottom two panels show AMPT calculations for the first Fourier coefficient $v_1(p_T)$ which are indicative of directed flow for the 30-40% centrality interval. The top left panel shows the difference between an event plane found from participants and the impact parameter vector, when calculated using BD simulation. The corresponding top right panel shows the same with a GD simulation. The bottom left panel shows v_1 with respect to the participant plane (red) and the impact parameter vector (pink) both using BD. Likewise the bottom right panel shows the same with a GD simulation.

participants and the impact parameter vector angles. The left shows this difference for the BD method, and the right for the GD method. The bottom two panels show v_1 calculated with BD (left) and GD (right) for the 30-40% centrality interval. Each of the bottom panels show calculations using the reaction plane and additionally the impact parameter vector. Significant variation is seen between BD and GD and in both cases the results feature positive v_1 above 1 GeV/c. This corresponds to directed flow predicted on the copper side of the azimuthal plane, in contradiction to measurements (Fig. 6.1).

Calculations of $v_2(p_T)$ and $v_3(p_T)$ using AMPT are shown in Figures 6.19, and 6.20. Both figures show calculations using partonic cross sections of 1.5 mb and 3.0 mb and all are made with BD having 42 mb nucleon-nucleon cross section. The centrality intervals range from 0-10% to 50-60% for v_2 and 0-10% to 20-30% for v_3. Like with v_1, smearing is again used with width 0.4 fm. The results reproduce measurements out to approximately 1 GeV/c. The larger 3.0 mb partonic cross section is found to provide a closer match.

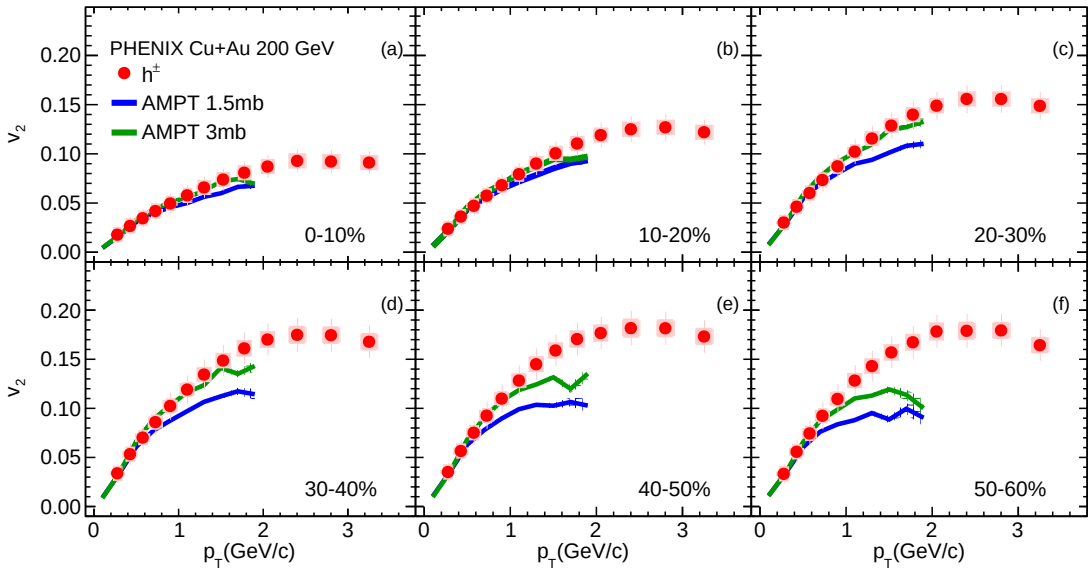

Figure 6.19: AMPT calculations of the second Fourier coefficient v_2 which are indicative of elliptic flow are shown with respect to p_T. Comparison is made to measured values (red) for six centrality intervals. The upper right panel shows 0-10% and subsequent panels are increasingly more peripheral in 10% increments. The blue curve shows model calculations using 1.5 mb partonic cross sections and the green shows 3 mb.

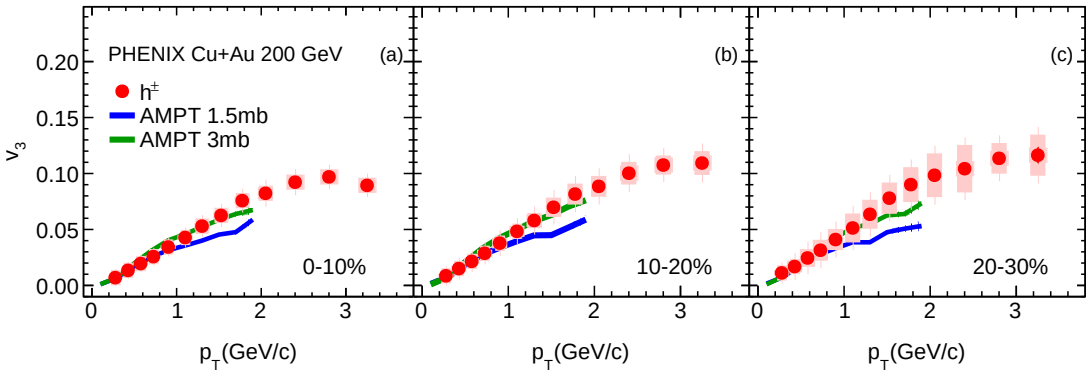

Figure 6.20: AMPT calculations of the third Fourier coefficient v_3 which are indicative of triangular flow are shown with respect to p_T. Comparison is made to measured values (red) for six centrality intervals. The upper right panel shows 0-10% and subsequent panels are increasingly more peripheral in 10% increments. The blue curve shows model calculations using 1.5 mb partonic cross sections and the green shows 3 mb.

centrality	Au+Au 200 GeV			Cu+Cu 200 GeV		Cu+Au 200 GeV			
bin	$N_{\rm part}$	ε_2	ε_3	$N_{\rm part}$	ε_2	$N_{\rm part}$	ε_1	ε_2	ε_3
0–10%	325.2	0.103	0.087	98.2	0.163	177.2	0.171	0.138	0.130
	±3.3	±0.003	± 0.0018	±2.4	±0.003	±5.2	±0.015	±0.011	±0.004
10–20%	234.6	0.200	0.122	73.6	0.241	132.4	0.283	0.204	0.161
	±4.7	±0.005	± 0.0035	±2.5	±0.007	±3.7	±0.023	±0.008	±0.005
20–30%	166.6	0.284	0.156	53.0	0.317	95.1	0.348	0.280	0.208
	±5.4	±0.006	± 0.0047	±1.9	±0.006	±3.2	±0.027	±0.008	±0.007
30–40%	114.2	0.356	0.198	37.3	0.401	65.7	0.400	0.357	0.266
	±4.4	±0.006	± 0.0083	±1.6	±0.008	±3.4	±0.027	±0.010	±0.010
40–50%	74.4	0.422	0.253	25.4	0.484	43.3	0.454	0.436	0.332
	±3.8	±0.006	± 0.0111	±1.3	±0.008	±3.0	±0.026	±0.013	±0.013
50–60%	45.5	0.491	0.325	16.7	0.579	26.8	0.520	0.523	0.412
	±3.3	±0.005	± 0.0179	±0.9	±0.008	±2.6	±0.024	±0.019	±0.019

Table 6.1: Number of participants (N_{part}) and the participant eccentricity (ε_1,ε_2, ε_3) from Glauber Monte Carlo simulations for Au+Au, Cu+Cu and Cu+Au collisions at 200 GeV.

Chapter 7

Summary

Measurements of the first three Fourier coefficients which characterize the first three moments of anisotropic flow were presented for Cu+Au collisions at $\sqrt{s_{NN}} = 200$ GeV. Measurements were made using the PHENIX detector at RHIC, and include both inclusive charged particles as well as identified $\pi^{\pm}$, $K^{\pm}$, p and $\bar{p}$ produced at midrapidity. The event plane method was used in each case which measures the azimuthal distribution of produced particles with respect to measurements of the collision azimuthal orientation.

Measurements of the first coefficient v_1 indicates directed flow. Unlike both v_2 and v_3 where the corresponding event plane angle measurements (Ψ_2 and Ψ_3) were made using participants, Ψ_1 is made with collision spectator neutrons. This alternate technique has the advantage of momentum independence between particles used in the event plane measurement and those in the azimuthal distribution, thus removing non-flow effects from momentum correlations.

The resulting v_1 values for inclusive charged hadrons measured as a function of p_T was found to increase in magnitude from low to medium p_T, peaking between 3 and 4 GeV/c consistently in four centrality intervals. The sign of v_1 at high p_T indicates an excess of particles produced on the gold spectator side of the collision. The size of the systematic uncertainty prevents strong conclusions as to a low p_T excess on the copper spectator side to balance the momentum distribution within the azimuthal plane. Beginning with the most central collision interval progressively to mid-central collisions, the magnitude of v_1 was found to decrease. A few empirical attempts have been made to employ scaling parameters that may point to the influence of the system size on directed flow.

Between 1 and 2 GeV/c, measurements of v_1 for identified hadrons were seen to have ordering according to their masses, which is consistent with hydrodynamic predictions of

a common velocity field. In all cases v_1 values were found to be significantly smaller than v_2 and v_3, reaching a maximum of around 4%. Direct comparisons to other systems was not possible as v_1 measurements have not been made.

The second coefficient v_2 measurement indicates elliptic flow, which is understood to originate in large part from a pressure gradient in the medium due to the geometry of the collision participant region. It is the largest in magnitude of the three harmonics for Cu+Au as with other systems and consistently increases with p_T up to its maximum between 2 and 3 V/c, and then decreases thereafter. Inclusive charged hadron v_2 was found to increase from the most central to mid-peripheral collision centrality interval. Comparisons were made to v_2 from Au+Au and Cu+Cu systems at the same energy and in every case values from Cu+Au were found to lie between the larger and smaller systems. When scaling by elliptic eccentricity was used on each of the three systems, v_2 was consistently ordered from smallest to largest system. Scaling by both elliptic eccentricity and $N_{part}^{1/3}$ aligned the three systems to one curve and additionally aligned all centrality intervals ($N_{part}^{1/3}$ is understood to corresponds to the length-scale of the medium).

Identified particle v_2 was seen to be ordered consistently according to mass and as anticipated from hydrodynamics. At p_T above 2 GeV the proton v_2 exceeds both pion and kaon v_2. This feature is understood to be the result of the parton recombination phase in the collision development.

Measurement of the third Fourier coefficient v_3 indicates triangular flow of produced particles. Little centrality dependence was found that is either consistent with a small increase from most central to less central, or within systematic uncertainties the results are also consistent with no centrality dependence. In each case v_3 increases from low to mid p_T and then decreases after approximately 3 GeV/c.

A similar approach to scaling was implemented as in the examination of v_2. Comparison were made of v_3 from Au+Au. Both triangular eccentricity and a combination of triangular eccentricity with $N_{part}^{1/3}$ were used with similar efficacy. Both scale the v_3 from

the two systems well at low p_T and largely within systematic uncertainty above 2 GeV/c.

Comparisons were made to theoretical predictions from both 3D+1 viscous hydrodynamics and AMPT. Calculations of v_1 for direct comparison from hydrodynamics were unavailable however qualitative comparison was possible and found to be agreement with measurements in this work. AMPT calculations of v_1 were found to be similar in magnitude and opposite in sign. Predictions from both 3D+1 viscous hydrodynamics and AMPT for v_2 and v_3 were found to be consistent with measurements below p_T of approximately 1 GeV/c.

The initial geometry with its event-by-event fluctuations and the system size which is related to N_{part} both play a role in the development of azimuthal anisotropy in the distribution of produced particles. The hydrodynamic description of heavy ion collisions with small η/s describes the data closely up to 2 GeV/c in transverse momentum, and microscopic transport calculations are able to describe the observed anisotropies up to 1 GeV/c.

BIBLIOGRAPHY

[1] J. Collins and M. Perry. Superdense matter: Neutrons or asymptotically free quarks? *Phys. Rev. Lett.*, 34:1353–1356, May 1975.

[2] E. Shuryak. Quantum chromodynamics and the theory of superdense matter. *Physics Reports*, 61(2):71–158, 1980.

[3] K. Adcox, S. Adler, et al. Formation of dense partonic matter in relativistic nucleusnucleus collisions at RHIC: Experimental evaluation by the PHENIX collaboration. *Nuclear Physics A*, 757(12):184 – 283, 2005. First Three Years of Operation of RHIC.

[4] Peter F. Kolb and Ulrich W. Heinz. Hydrodynamic description of ultrarelativistic heavy ion collisions. 2003.

[5] J. Adams, M. Aggarwal, et al. Experimental and theoretical challenges in the search for the quark gluon plasma: The STAR Collaboration's critical assessment of the evidence from RHIC collisions. *Nucl.Phys.*, A757:102–183, 2005.

[6] B. Back, M. Baker, et al. The PHOBOS perspective on discoveries at RHIC. *Nucl.Phys.*, A757:28–101, 2005.

[7] E. Shuryak. What RHIC experiments and theory tell us about properties of quark-gluon plasma? *Nucl.Phys.*, A750:64–83, 2005.

[8] M. Luzum and J. Ollitrault. Extracting the shear viscosity of the quark-gluon plasma from flow in ultra-central heavy-ion collisions. *Nuclear Physics A*, 904905:377c – 380c, 2013. The Quark Matter 2012 Proceedings of the XXIII International Conference on Ultrarelativistic Nucleus-Nucleus Collisions.

[9] P. Kovtun, D. Son, et al. Viscosity in strongly interacting quantum field theories from black hole physics. *Phys. Rev. Lett.*, 94:111601, Mar 2005.

[10] A. Adare, S. Afanasiev, et al. Measurements of higher-order flow harmonics in Au+Au collisions at $\sqrt{s_{NN}} = 200$ GeV. *Phys. Rev. Lett.*, 107:252301, 2011.

[11] L. Adamczyk, J. Adkins, et al. Third harmonic flow of charged particles in Au + Au collisions at $\sqrt{s_{NN}} = 200$ GeV. *Phys. Rev. C*, 88:014904, Jul 2013.

[12] K. Aamodt, B. Abelev, et al. Higher harmonic anisotropic flow measurements of charged particles in Pb-Pb collisions at $\sqrt{s_{NN}} = 2.76$ TeV. *Phys. Rev. Lett.*, 107:032301, Jul 2011.

[13] G. Aad, B. Abbott, et al. Measurement of the azimuthal anisotropy for charged particle production in $\sqrt{s_{NN}} = 2.76$ TeV lead-lead collisions with the ATLAS detector. *Phys. Rev. C*, 86:014907, Jul 2012.

[14] S. Chatrchyan, V. Khachatryan, et al. Measurement of higher-order harmonic azimuthal anisotropy in PbPb collisions at $\sqrt{s_{NN}}$ = 2.76 TeV. *Phys. Rev.*, C89(4):044906, 2014.

[15] B. Abelev, J. Adam, et al. Directed flow of charged particles at midrapidity relative to the spectator plane in Pb-Pb collisions at $\sqrt{s_{NN}}$=2.76 TeV. *Phys. Rev. Lett.*, 111:232302, Dec 2013.

[16] B. Alver and G. Roland. Collision geometry fluctuations and triangular flow in heavy-ion collisions. *Phys. Rev.*, C81:054905, 2010.

[17] K. Ikematsu, Y. Iwata, et al. A start-timing detector for the collider experiment PHENIX at RHIC-BNL. *Nuclear Instruments and Methods in Physics Research Section A: Accelerators, Spectrometers, Detectors and Associated Equipment*, 411(23):238 – 248, 1998.

[18] M. Chiu, A. Denisov, et al. Measurement of mutual Coulomb dissociation in $\sqrt{s_{\rm NN}} =$ 130GeV $Au+Au$ collisions. *Phys. Rev. Lett.*, 89:012302, Jun 2002.

[19] C. Adler, A. Denisov, et al. The RHIC zero degree calorimeters. *Nuclear Instruments and Methods in Physics Research Section A: Accelerators, Spectrometers, Detectors and Associated Equipment*, 470(3):488 – 499, 2001.

[20] H. Crawford, D. Keane, et al. Proposed addition of a shower max detector to the STAR zero degree calorimeters. *Star Technical Note*, page SN0448, Dec 2003.

[21] G. Charpak, R. Bouclier, et al. The use of multiwire proportional counters to select and localize charged particles. *Nuclear Instruments and Methods*, 62(3):262 – 268, 1968.

[22] G. Charpak, , and F. Sauli. High-resolution electronic particle detectors. *Annual Review of Nuclear and Particle Science*, 34(1):285–350, 1984.

[23] K. Adcox, N.N. Ajitanand, et al. {PHENIX} central arm tracking detectors. *Nuclear Instruments and Methods in Physics Research Section A: Accelerators, Spectrometers, Detectors and Associated Equipment*, 499(23):489 – 507, 2003. The Relativistic Heavy Ion Collider Project: {RHIC} and its Detectors.

[24] V. Riabov. Drift chambers for the PHENIX central tracking system. *Nuclear Instruments and Methods in Physics Research Section A: Accelerators, Spectrometers, Detectors and Associated Equipment*, 419(23):363 – 369, 1998.

[25] PHENIX Drift Chamber Operation Principles. *PHENIX Focus Seminar*, Jan 2004.

[26] K. Adcox, J. Ajitanand, et al. Construction and performance of the PHENIX pad chambers. *Nuclear Instruments and Methods in Physics Research Section A: Accelerators, Spectrometers, Detectors and Associated Equipment*, 497(23):263 – 293, 2003.

[27] P. Nilsson, J. Barrette, et al. The pixel readout system for the PHENIX pad chambers. *Nuclear Physics A*, 661(14):665 – 668, 1999.

[28] L. Aphecetche, T. Awes, et al. PHENIX calorimeter. *Nuclear Instruments and Methods in Physics Research Section A: Accelerators, Spectrometers, Detectors and Associated Equipment*, 499(23):521 – 536, 2003. The Relativistic Heavy Ion Collider Project: RHIC and its Detectors.

[29] M. Aizawa, Y. Akiba, et al. PHENIX central arm particle ID detectors. *Nuclear Instruments and Methods in Physics Research Section A: Accelerators, Spectrometers, Detectors and Associated Equipment*, 499(23):508 – 520, 2003. The Relativistic Heavy Ion Collider Project: RHIC and its Detectors.

[30] E. Zeballos, I. Crotty, et al. A new type of resistive plate chamber: The multigap RPC. *Nuclear Instruments and Methods in Physics Research Section A: Accelerators, Spectrometers, Detectors and Associated Equipment*, 374(1):132 – 135, 1996.

[31] J. Velkovska, T. Chujo, et al. Multi-gap resistive plate chambers: Time-of-flight system of the PHENIX high-p_T detector. *Conceptual Design Report*, 2005.

[32] Shengli Huang. The Time of Flight Detector Upgrade at PHENIX. *IEEE 2006 Nuclear Science Symposium*, Dec 2006.

[33] J. T. Mitchell et al. Event reconstruction in the PHENIX central arm spectrometers. *Nucl. Instrum. Meth.*, A482:491–512, 2002.

[34] M. Santos and F. Dupertuis. Mass distributions marginalized over per-event errors. *Nuclear Instruments and Methods in Physics Research Section A: Accelerators, Spectrometers, Detectors and Associated Equipment*, 764:150 – 155, 2014.

[35] A. Ohlson. Calculating jet v_n and the event plane in the presence of a jet. *Phys. Rev. C*, 87:034909, Mar 2013.

[36] S. Rajeev and J. Ollitrault. Eccentricity fluctuations and elliptic flow at RHIC. *Physics Letters B*, 641(34):260 – 264, 2006.

[37] S. Voloshin, A. Poskanzer, et al. Collective phenomena in non-central nuclear collisions. 2008.

[38] L. Adamczyk, G. Agakishiev, et al. Inclusive charged hadron elliptic flow in Au+Au collisions at $\sqrt{s_{NN}} = 7.7$-39 GeV. *Phys. Rev. C*, 86:054908, Nov 2012.

[39] A. Adare, S. Afanasiev, et al. Systematic study of azimuthal anisotropy in Cu+Cu and Au+Au collisions at $\sqrt{s_{NN}} = 62.4$ and 200 GeV. *Phys. Rev. C*, 92:034913, Sep 2015.

[40] S. Afanasiev, C. Aidala, et al. Systematic studies of elliptic flow measurements in $\mathrm{Au} + \mathrm{Au}$ collisions at $\sqrt{s_{NN}} = 200$ Ge. *Phys. Rev. C*, 80:024909, Aug 2009.

[41] L. Adamczyk, J. Adkins, et al. Elliptic flow of identified hadrons in Au+Au collisions at $\sqrt{s_{NN}} = 7.7$-62.4 GeV. *Phys. Rev. C*, 88:014902, Jul 2013.

[42] Performance of the ALICE experiment at the CERN LHC. *International Journal of Modern Physics A*, 29(24):1430044, 2014.

[43] I. Selyuzhenkov and S. Voloshin. Effects of nonuniform acceptance in anisotropic flow measurements. *Phys. Rev. C*, 77:034904, Mar 2008.

[44] J. Barrette, R. Bellwied, et al. Proton and pion production relative to the reaction plane in Au+Au collisions at 11*A* GeV/*c*. *Phys. Rev. C*, 56:3254–3264, Dec 1997.

[45] A. Poskanzer and S. Voloshin. Methods for analyzing anisotropic flow in relativistic nuclear collisions. *Phys. Rev. C*, 58:1671–1678, Sep 1998.

[46] J. Adams, M. Aggarwal, et al. Directed flow in Au+Au collisions at $\sqrt{s_{NN}} = 62.4$ GeV. *Phys. Rev. C*, 73:034903, Mar 2006.

[47] S. Adler, S. Afanasiev, et al. Saturation of azimuthal anisotropy in Au+Au collisions at $\sqrt{s_{NN}} = 62 - 200$ GeV. *Phys. Rev. Lett.*, 94:232302, Jun 2005.

[48] E. Avsar, C. Flensburg, et al. Eccentricity and elliptic flow in proton-proton collisions from parton evolution. *Physics Letters B*, 702(5):394 – 397, 2011.

[49] T. Hirano and Y. Nara. Eccentricity fluctuation effects on elliptic flow in relativistic heavy ion collisions. *Phys. Rev. C*, 79:064904, Jun 2009.

[50] J. Noronha-Hostler, L. Yan, et al. Linear and cubic response to the initial eccentricity in heavy-ion collisions. *Phys. Rev. C*, 93:014909, Jan 2016.

[51] M. Miller, K. Reygers, et al. Glauber modeling in high-energy nuclear collisions. *Annual Review of Nuclear and Particle Science*, 57(1):205–243, 2007.

[52] R. Glauber. Cross sections in deuterium at high energies. *Phys. Rev.*, 100:242–248, Oct 1955.

[53] R. Woods and D. Saxon. Diffuse surface optical model for nucleon-nuclei scattering. *Phys. Rev.*, 95:577–578, Jul 1954.

[54] A. Adare, S. Afanasiev, et al. Scaling properties of azimuthal anisotropy in Au+Au and Cu+Cu collisions at $\sqrt{s_{\mathrm{NN}}} = 200$ GeV. *Phys. Rev. Lett.*, 98:162301, Apr 2007.

[55] S. Afanasiev, C. Aidala, et al. Charged kaon interferometric probes of space-time evolution in Au+Au collisions at $\sqrt{s_{\mathrm{NN}}} = 200$ GeV. *Phys. Rev. Lett.*, 103:142301, Sep 2009.

[56] A. Adare, S. Afanasiev, et al. Measurement of the higher-order anisotropic flow coefficients for identified hadrons in Au+Au collisions at $\sqrt{s_{NN}}$ = 200 GeV. 2014.

[57] A. Adare, C. Aidala, et al. "Measurements of directed, elliptic, and triangular flow in Cu+Au collisions at $\sqrt{s_{NN}} = 200$ GeV". 2015.

[58] H. Masui and A. Schmah. Event plane resolution correction for azimuthal anisotropy in wide centrality bins.

[59] J. Chen, Y. Ma, et al. Elliptic flow of ϕ mesons and strange quark collectivity. *Phys. Rev. C*, 74:064902, Dec 2006.

[60] R. Fries, V. Greco, et al. Coalescence models for hadron formation from quark-gluon plasma. *Annual Review of Nuclear and Particle Science*, 58(1):177–205, 2008.

[61] M. He, R. Fries, et al. Scaling of elliptic flow, recombination, and sequential freeze-out of hadrons in heavy-ion collisions. *Phys. Rev. C*, 82:034907, Sep 2010.

[62] D. Molnár and S. Voloshin. Elliptic flow at large transverse momenta from quark coalescence. *Phys. Rev. Lett.*, 91:092301, Aug 2003.

[63] C. Adler, Z. Ahammed, et al. Identified particle elliptic flow in Au+Au collisions at $\sqrt{s_{\rm NN}} = 130$GeV. *Phys. Rev. Lett.*, 87:182301, Oct 2001.

[64] X. Sun, H. Masui, et al. Blast wave fits to elliptic flow data at $\sqrt{s_{\rm NN}} = 7.7 - 2760$ gev. *Phys. Rev. C*, 91:024903, Feb 2015.

[65] L. Adamczyk, J. Adkins, et al. Centrality dependence of identified particle elliptic flow in relativistic heavy ion collisions at $\sqrt{s_{NN}} = 7.7 - 62.4$ GeV. *Phys. Rev. C*, 93:014907, Jan 2016.

[66] R. Pathria. *Statistical Mechanics*. International series of monographs in natural philosophy. Elsevier Science & Technology Books, 1972.

[67] F. Wojciech. *Phenomenology of Ultra-relativistic Heavy-ion Collisions*. World Scientific.

[68] B. Schenke, S. Jeon, et al. Elliptic and triangular flow in event-by-event D $= 3 + 1$ viscous hydrodynamics. *Phys. Rev. Lett.*, 106:042301, Jan 2011.

[69] P. Bożek. Flow and interferometry in (3 + 1)-dimensional viscous hydrodynamics. *Phys. Rev. C*, 85:034901, Mar 2012.

[70] P. Huovinen and P. Ruuskanen. Hydrodynamic models for heavy ion collisions. *Annual Review of Nuclear and Particle Science*, 56(1):163–206, 2006.

[71] K. Dusling and D. Teaney. Simulating elliptic flow with viscous hydrodynamics. *Phys. Rev. C*, 77:034905, Mar 2008.

[72] B. Schenke, S. Jeon, et al. (3+1)D hydrodynamic simulation of relativistic heavy-ion collisions. *Phys. Rev. C*, 82:014903, Jul 2010.

[73] G. Baym, B. Friman, et al. Hydrodynamics of ultra-relativistic heavy ion collisions. *Nuclear Physics A*, 407(3):541 – 570, 1983.

[74] F. Gardim, F. Grassi, et al. Directed flow at midrapidity in event-by-event hydrodynamics. *Phys. Rev. C*, 83:064901, Jun 2011.

[75] Piotr Boek. Event-by-event viscous hydrodynamics for cuau collisions at. *Physics Letters B*, 717(13):287 – 290, 2012.

[76] Z. Lin, C. Ko, et al. Multiphase transport model for relativistic heavy ion collisions. *Phys. Rev. C*, 72:064901, Dec 2005.

[77] X. Wang and M. Gyulassy. HIJING: A Monte Carlo model for multiple jet production in pp, pA, and AA collisions. *Phys. Rev. D*, 44:3501–3516, Dec 1991.

[78] X. Wang and M. Gyulassy. Systematic study of particle production in $p+p(\overline{p})$ collisions via the HIJING model. *Phys. Rev. D*, 45:844–856, Feb 1992.

[79] B. Zhang, Z. Chen, et al. Experimental study of four-channel tunable optical add/drop multiplexer based on fiber bragg gratings, 1998.

[80] B. Li and C. Ko. Formation of superdense hadronic matter in high energy heavy-ion collisions. *Phys. Rev. C*, 52:2037–2063, Oct 1995.

[81] J. Orjuela Koop, A. Adare, et al. Azimuthal anisotropy relative to the participant plane from a multiphase transport model in central $p+\mathrm{Au}$, $d+\mathrm{Au}$, and $^3\mathrm{He}+\mathrm{Au}$ collisions at $\sqrt{s_{NN}} = 200$ GeV. *Phys. Rev. C*, 92:054903, Nov 2015.